University College London

PhD Thesis in Photonic Systems Development

The Timing Performance of Scintillator Detectors

Author:

Mark Stephen Brown

Supervisors:

Dr. Ioannis Papakonstantinou

&

Dr. Cyril Renaud

November 11, 2016

Abstract

The timing performance of the scintillator detector is of critical importance to positron emission tomography. An improvement in this quantity will lead to dramatically improved image quality giving better information to clinicians. With the recent large improvements in the performance of scintillator detectors, due to switches to new inorganic scintillator crystals such as LYSO and new photodetectors such as MPPCs, smaller effects are no longer negligible if we wish to continue to improve. In this PhD I present a Fisher Information based statistical model. This allows light-based contributions to the timing performance to be quantified. The model allows us to suggest areas of attack which could lead to further improvement in scintillator detector performance. To validate this model, experimental work has been carried out at UCL and CERN. This validation is split into radiation and optical measurements. I first present a new study into the effect of the interaction position within the scintillator crystal upon the timing performance. The radiation results demonstrate no relationship between the two effects. Secondly to explore this relationship further, I performed measurements looking at how the surface profile of the scintillator crystal alters light propagation through it. These measurements are performed using time correlated single photon counting and a reflection goniophotometer. The optical results demonstrate the surface can delay propagation of light through the scintillator crystal.

With the validated model, estimates of the Cramer Rao Lower Bound are made for various potential improvements such as preferred direction surface scattering and refractive index mismatch correction. I conclude with the presentation of one potential method; namely utilising metasurfaces upon the lateral faces of scintillator crystals to scatter light towards the photodetector.

Declaration

I, Mark Stephen Brown confirm that the work presented in this thesis is my own. Where information has been derived from other sources, I confirm that this has been indicated in the thesis.

PhD Candidate	Date

Acknowledgements

It is perhaps fair to say this thesis has taken me a while to write. In that time I have changed and grown as a person. As I write this, I'm drinking coffee pondering how I managed to get this far. The answer of course is with help. From my mum and from brothers. They have always supported me as best as she could. One of brothers gave me the laptop I'm writing this thesis upon! Without their support I would not have pushed on this far. From my school days there are two teachers who always believed in me. From them I have my desire to learn and my love of physics and computers. Next I would like to thank the photonics systems development CDT who offered me a place to study. I did not dream for a second they would accept me and the moment I was offered a place will remain with me as a constant reminder to not always assume the worst.

To the PhD itself! Clemens and Alaric were a source of stability and support throughout my studies at UCL.

Finally to my supervisor. Ioannis' enthusiasm and expertise combined with his friendship and unwavering support over the last four years has made this thesis possible. Without question, if I ever had a problem, he would available to help.

Thanks to Stefan, without whom this thesis would most certainly be a chapter shorter.

Finally to my friends, near and far. As we all are, we are shaped by the people who surround us. And I have been shaped to be a better person. The kindnesses offered are not and never will be forgotten.

Contents

List of Figures

List of Tables

Chapter 1

Introduction

1.1 Motivation

Advances in materials and technologies used in Positron Emission Tomography (PET) have lead to significant improvements in image quality [1]. PET scanners are comprised of many thousand scintillator detectors. Each scintillator detector is composed of a scintillator crystal — a material which emits light when ionising radiation strikes it and a photodetector — a device for conversion of light into an electrical signal. Both in recent times have been improved. In the case of the scintillator crystal, older materials such as BGO are being replaced by new heavy inorganic materials such as LYSO and BaFr. These newer materials have much higher light outputs and much lower decay times [2, 3]. For the photodetectors, older style photomultiplier tubes are being replaces with Silicon Photomultiplier (SiPM) or Multi-Pixel Photon Counter (MPPC). In addition to being faster, these detectors function within strong magnetic fields allowing potential multi-modal scanners such as PET-MRI [4].

In this work degradation effects upon the performance of modern scintillator detectors are investigated. This work looks at what would previously be considered negligible effects and endeavours to determine if the limits of scintillator detector performance can be pushed further. We are primarily interested in optical effects within the scintillator crystal and whether incorporation of 'photonics' can help improve the time resolution. Further improvements in the timing performance

of the scintillator detector will allow incorporation of Time of Flight (TOF) information into PET. This will not only reduce scan times, TOF information will allow significant improvements to the image quality [1, 5, 6]. Specifically, a reduction time resolution will lead to a higher signal to noise ratio. This will produce higher contrast images, thus giving clinicians more information about their patient [7].

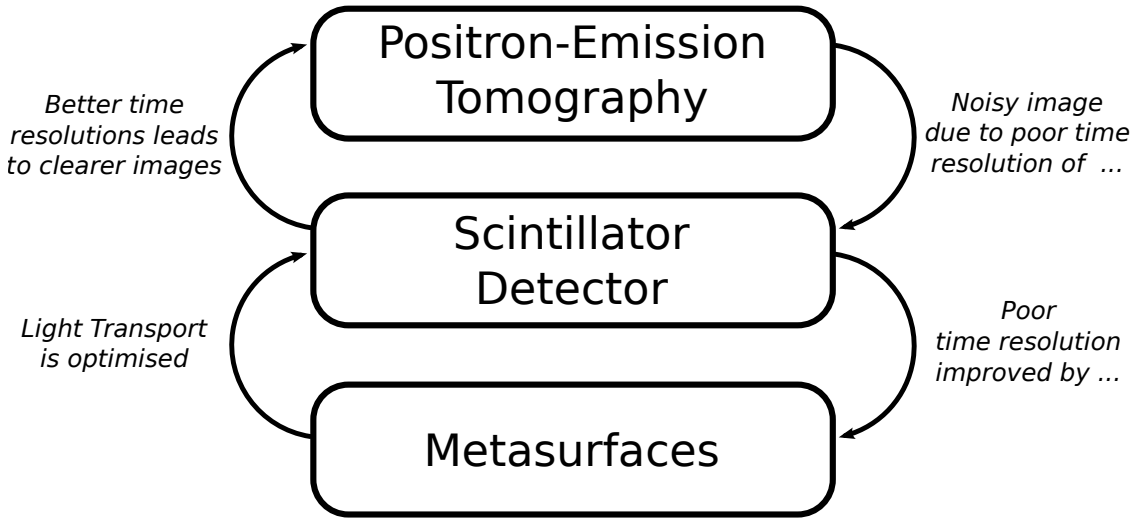

Figure 1.1: PET is a complex system whereby issues in one layer can significantly affect the performance in another. In PET, noisy images can be improved by improvement of the radiation detectors used. In this work it is proposed that alteration of the light transport via inclusion of a metasurface upon each scintillator detector will improve performance.

In figure 1.1 the synopsis of the content to be covered within this thesis is stated. The initial aim is to experimentally explore contributions to the performance of scintillator detectors using direct and indirect techniques. These results will be used to validate an experimental model. The model will be used to explore potential areas for improvement. Finally we will look at inclusion of a metasurface to alter light propagation through the scintillator crystal.

1.2 Outline of Thesis

To begin, experimental measurements to explore light propagation within the scintillator crystal are presented. In Chapter 3 radiation measurements exploring the effect of the interaction position upon the timing and energy performance of the scintillator detector are presented. These measure-

ments were published in PLOS ONE in 2014 [8]. Following this, optical measurements performed at UCL are presented in Chapter 4. Two experiments present new work looking at light interaction with the scintillator crystal. Performance changes are inferred from these measurements. The results collected from both experimental chapters are used in Chapter 5 to validate a new statistical model to predict the effect of light propagation through the scintillator crystal upon the timing performance of the scintillator detector. Both analytical and Monte-Carlo simulations of light propagation are presented and used. In Chapter 6 the statistical model is explored further to look at more complex surface and geometrical effects. The model is used to predict potential improvements due to alterations in scintillator crystal shape and incorporation of scattering structures at the lateral faces. Finally in Chapter 7 one method for designing such scattering structures is presented. To demonstrate this method of calculating the scattering differential cross section a polar angle confinement structure is designed.

In each chapter Python code has been used to analyse data, plot graphs, simulate light propagation, calculate timing performance and design scattering structures. Where appropriate the code for each has been placed online at `www.github.com/marksbrown`.

Chapter 2

Background

2.1 Positron-Emission Tomography

Overview of Technique

Positron-Emission Tomography, or PET, is a medical imaging technique. Images are formed by recovering a density map of positron-emitting, biologically-active radiotracer within the patient. This radiotracer will form a non-uniform distribution within the patient determined by the biological process it seeks to interact with. For instance FDG is a glucose analog commonly used in oncology for determining tumour spread within a patient. To determine the location of the radiotracer the result of radioactive decay within the patient must be detected. This is done by detection of the resulting products from positron-electron annihilation. A positron will annihilate close to its emission position [4] with an electron forming two 0.511MeV gamma ray photons. Due to momentum conservation, both gamma ray photons will travel in opposing directions. Detection of both gamma ray photons allows us to define a line, known as the Line of Response (LOR). Collections of such LORs allow variations in absorption of the radiotracer to be mapped and thus an image is generated.

In this section we will discuss each of these terms in greater detail.

2.1.1 Radiotracer

Reputedly the first usage of radioactive material for tracking was carried out by George de Hevesy in the early twentieth century. Using Lead-212 he was able to definitively prove his landlady's recycling of leftovers into meals later in the week! The most common radiotracer used in PET today is a glucose analogue known as Fludeoxyglucose (18-FDG). Different rates of glucose absorption in the body leads to a varying density of radiotracer throughout the body. Crucially 18-FDG is used in oncology due to tumours absorbing 10 times as much glucose as regular tissue [7].

In figure 2.1 the relationship between three key parameters in PET is shown.

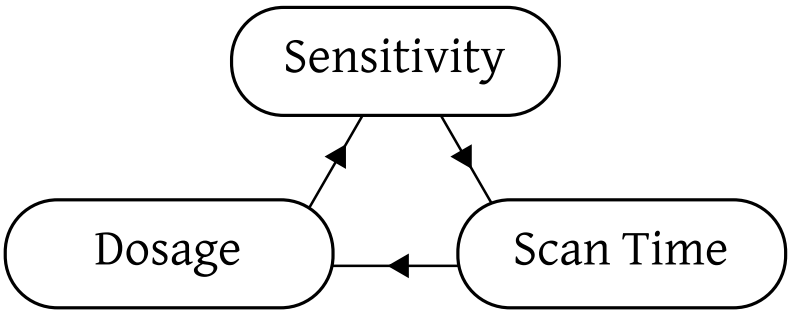

Figure 2.1: Three effects are linked in PET. These are dosage, sensitivity and scan time. An improvement in one, will allow a reduction in the other two.

The three parameters are dosage — the amount of radiotracer injected into a given patient, scan time — the duration of a given PET scan and sensitivity — the percentage of (true) gamma ray photon pairs detected. Simply put, an 'improvement' in any of these three, will lead to an improvement in the other two. For instance if it was possible to safely increase the radiation dosage to the patient, the scan time would be reduced and the sensitivity would not need to be as high to produce an image of the same quality. Maintaining two of the parameters and improving a third will improve PET image quality.

The injected dose, typically 400MBq or 8mSv for a whole body scan [9], must be kept as low as possible to prevent radiation poisoning to the patient. Furthermore fast-growing tissue experiences comparatively high damage due to radiation. Since these tissues also absorb more glucose than the body, this leads to a disproportionally higher radiation dose due to the targeted nature of the radiotracer. This high dosage currently prevents vulnerable groups such as children from using PET. Therefore a future aim should be to reduce this dosage.

PET scanners typically perform a low number of scans per day. This is due to the long scan time required to detect such the radiation dose used in PET. An increase in the number of scans per day would decrease the running cost per patient.

The fraction of positron emissions detected compared to those produced is known as the sensitivity. In PET this fraction is below 0.05% for a whole body image [7]. One of the aims towards the next generation of PET scanner is to improve this [7]. The two primary factors to the sensitivity are the solid angle coverage of scintillator detectors about the patient and the detection efficiency per scintillator detector. The former is generally limited due to the cost and additional complexity of more scintillator detectors. The latter will discussed in section 2.2.3 further.

2.1.2 Positron-Electron Annihilation

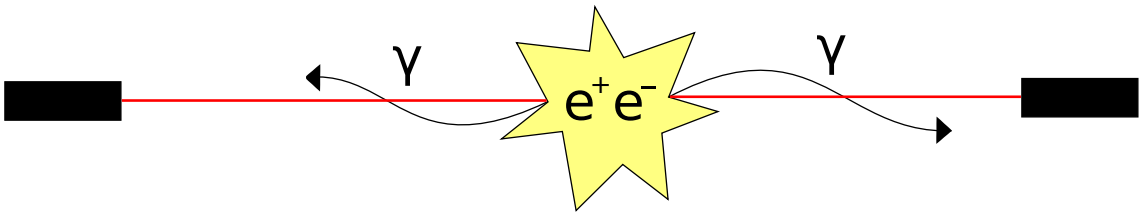

Figure 2.2: Back-to-back gamma ray photons detected in opposing scintillator detectors defining a line-of-response (LOR).

Two back-to-back gamma rays define a line of response (LOR). A non-zero net momentum of the electron-positron pair will result in acollinearity from 180° [10]. Positrons emitted from radiotracers will have an initial amount of kinetic energy. The probability of annihilation increases with decreasing net velocity of the electron-positron pair. Until annihilation, the positron loses energy via elastic scattering, typically travelling 0.1 mm for 18-FDG positrons in a water [11, Fig.7]. For no magnetic field, this distance is typically taken to be the intrinsic spatial resolution of the PET scanner [4]. The actual spatial resolution in practice is related to the shape of the scintillator crystal. This is discussed further in section 2.2.3.

2.1.3 PET Image Reconstruction

In figure 2.3 a simulation of the reconstruction process used in PET is shown.

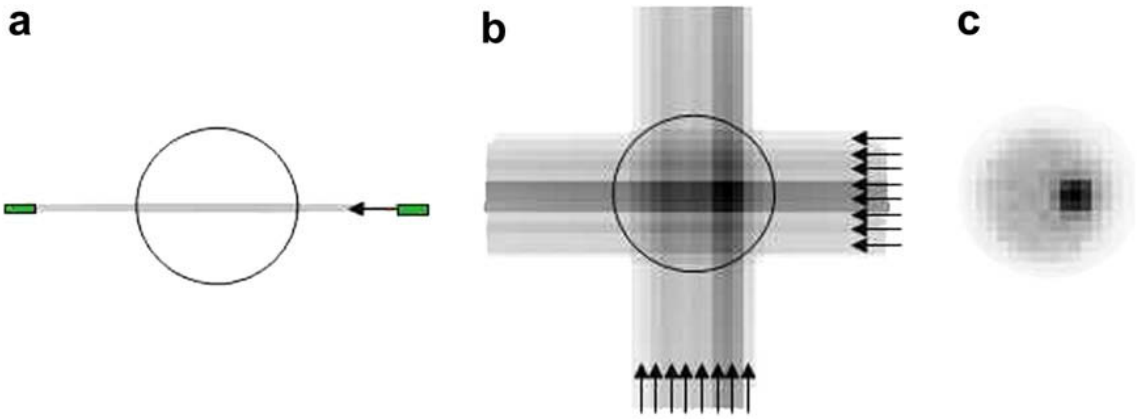

Figure 2.3: Simulation of the reconstruction process of an object used in PET. This image is taken from [12].

In this figure we can see three sub-figures; a, b, c. 'a' shows a single LOR between two scintillator detectors shown in green. 'b' in a linear summation of many LORs. In this image it is seen that a high density of intersections will indicate a high density of radiotracer. In 'c' the resulting PET image from the intersection data is shown. This is created without any TOF information.

In an actual image reconstruction, algorithms take into account a wide variety of factors to improve image quality. These include gamma-ray attenuation within the body, movement of the patient and relative scintillator detector positioning.

2.1.4 Image Quality Metrics

Image quality is typically characterised by the Noise-equivalent count rate (NECR), which is defined as

$$\text{NECR} = \frac{T^2}{T + S + 2R} \tag{2.1}$$

where T is the true coincidence event rate, S is the scattered event rate and R is the random event rate. T is the number of true $\gamma\gamma$ events detected via the photoelectric effect per unit time. S is similar but in this case one (or both) of the gamma ray photons interacts with the scintillator detector via Compton scattering. R is the rate due to completely uncorrelated random γ detections.

R can be simplified into

$$R = 2R_i^2 \Delta T \tag{2.2}$$

where R_i is the individual random count rate for a single scintillator detector and ΔT is the maximum time window between $\gamma\gamma$ pairs allowed. In the above we assume that the individual count rate is identical for all scintillator detectors within the PET scanner. It can be seen that can see that a reduction in ΔT will lead to an increase in the NECR. The width of the time window must be sufficiently large to account for the uncertainty in detection time, the time resolution, of each scintillator detector. If ΔT is too low, the true coincidence rate, T, will be artificially reduced by clipping. Therefore the time resolution must be improved to allow this reduction.

For sufficient improvement in the time resolution, the difference in flight time between the two gamma ray photons could be determined. This would allow us to assign probability to regions along the LOR of where the emission site originated. This is known as time-of-flight (or TOF) information. In figure 2.4 a simulation of the reconstruction process, with TOF information, is shown.

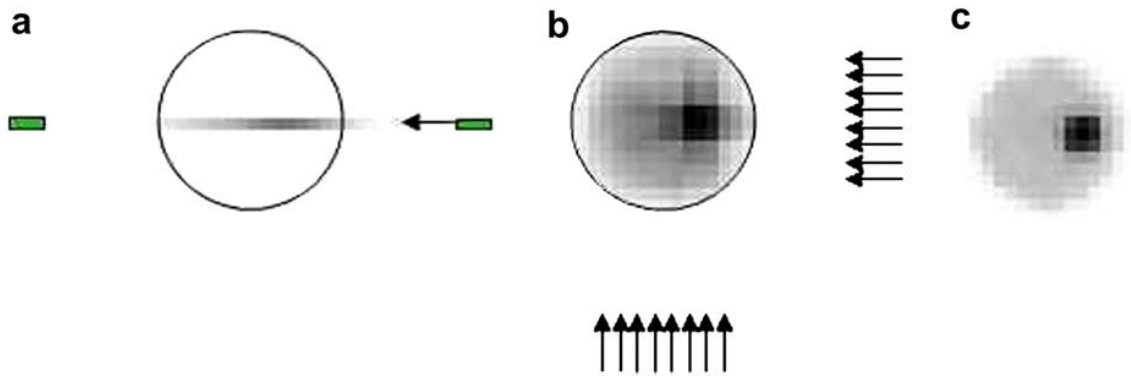

Figure 2.4: Simulation of the reconstruction process of an object used in PET using TOF information. Note the reduced noise about the object of interest. This image is taken from [12].

Compared to figure 2.3 the resulting reconstructed image shows less noise about the object of interest. Several studies [5, 6] have investigated the relationship between image quality and the time resolution. In [5, Table 4] predicted performance gains for inclusion of TOF information upon the NECR are shown. Additionally a lower number of counts would be required to produce an

image of the same quality without TOF information. Therefore it would be possible to accomplish quicker scan times [13].

2.2 The Scintillator Detector

Overview

In figure 2.5 a cross section of a scintillator detector is shown.

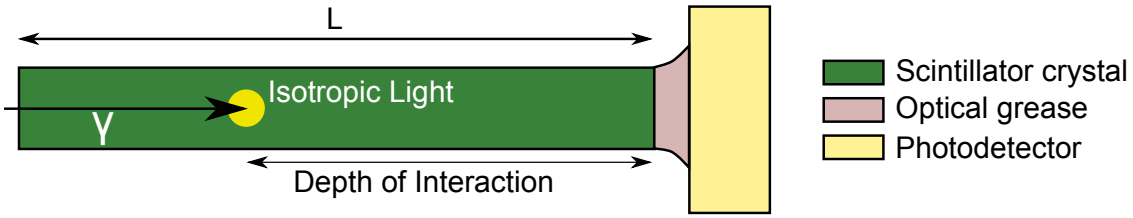

Figure 2.5: The scintillator detector is comprised of three main components. A scintillator crystal to convert incident radiation into an isotropic burst of optical photons. A photodetector to convert the generated optical light into an electrical signal. Optical grease to improve coupling between the scintillator crystal and the photodetector. The length of the scintillator crystal L and the depth of interaction (Depth of Interaction (DOI)) are shown.

Ionising radiation striking a scintillator crystal will produce a large number of low energy photons. These are predominantly in the optical regime and will therefore be referred to as optical photons[1]. The number of optical photons produced and energy of each will depend on the intrinsic material properties [2].

In this work we are interested in detection of 0.511 MeV gamma-ray photons. The process from γ interaction with the scintillator detector to successful detection can described as thus:

1. A single γ interacts with the scintillator crystal by the photoelectric effect and is totally absorbed producing a single high-energy electron-hole pair.

2. Passing through the scintillator crystal this high-energy electron thermally excites a large number of additional electron-hole pairs. In a modern scintillator material this is typically

[1]Many scintillating materials do in fact produce photons in the ultra-violet, however these are difficult (and expensive) to detect due to absorption by most forms of glass used in photodetectors

tens of thousands. This occurs within a micron-sized volume near to the γ interaction position.

3. Produced electron-hole pairs typically take tens of picoseconds to reach locations where recombinations can occur. These sites are known as luminescent centres.

4. At each luminescent centre recombination occurs, typically taking tens of nanoseconds, causing the emission of a optical photon.

5. Each optical photon will have a random direction and polarisation with respect to others.

6. Those optical photons which are not lost, will arrive at the photodetector and potentially be detected.

The important points of this process will now be discussed in further detail. First we must cover the names of specific components commonly used along with some nomenclature.

2.2.1 Properties of the Modern Scintillator Detector

Scintillator Crystals

In this PhD we use Lu_2SiO_5:Ce, commonly known as glslso or $Lu_{(2-x)}Y_xSiO_5$:Ce, known as Cerium doped Lutetium Yttrium Orthosilicate (LYSO:Ce). Whilst there are many other scintillator crystals available, L(Y)SO (LSO or LYSO) is set to be used in the 'next generation' of PET scanner due to its excellent performance compared to prior materials such as Bismuth Germanate (BGO). The difference between the two scintillator crystals is primarily one of crystal growth. LYSO has a much lower melting point [14] than LSO which makes it comparatively easier to fabricate. Also LYSO has a marginally lower density than LSO. LYSO is 7.1gcm^3 compared to the LSO value of 7.4gcm^3[2]. Unless otherwise stated the properties of LYSO and LSO are considered identical. Due to this LSO and LYSO are typically considered interchangeable terms.

Whilst Cerium doping is common, other dopants have been demonstrated. For instance Calcium doped LSO has been shown to have a lower decay rate [15]. More detailed information with respect to the material science of inorganic scintillator crystals can be found in [16]. Both LSO:Ce and LSO:CeCa are used in chapter 3.

[2]Internally measured at UCL using vernier callipers and a balance.

Photodetectors

Two photodetectors are considered in this PhD. A Photonis XP 2020 [17] photomultiplier tube (PMT) and a Hamamatsu S10931-050P [18] multi-pixel photon counter (MPPC). The former was selected due to its ubiquity and the latter as it is the current standard photodetector in operation with our colleagues at CERN. The hamamatsu handbook [19] covers a detailed introduction to photodetectors. An excellent review of the basics of scintillator detectors as a whole can be found in [20].

2.2.2 γ Interaction with the Scintillator Crystal

Sub-MeV ionising radiation will interact with the scintillator crystal via two mechanisms. These are via total absorption (the photoelectric effect) or inelastic (Compton) scattering. In both cases the number of electron-hole pairs generated is proportional to the energy deposited.

In figure 2.6 a luminescent centre of a scintillator crystal is shown.

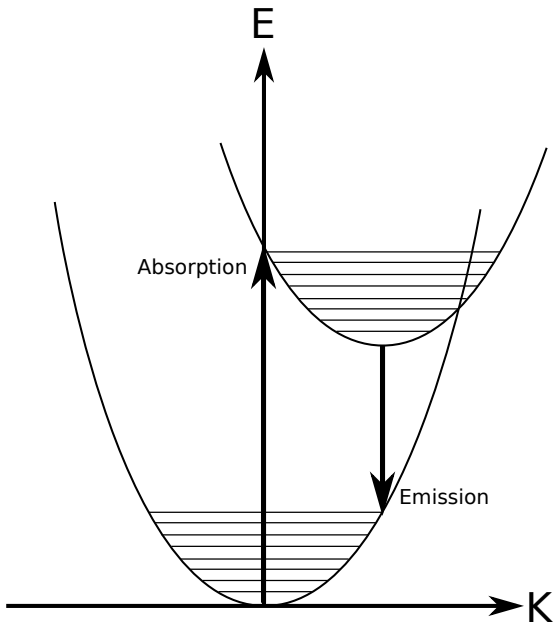

Figure 2.6: E-k diagram for a typical luminescence centre within a scintillator crystal. The relative offset of bands is responsible for differences in absorption and emission spectra.

Due to this E-K behaviour scintillator crystals are transparent to the radiation they produce by

electron-hole combination. For sufficiently high energy deposited by interaction with the scintillator crystal, the number of photons produced will be proportional to this. An example of the energy distribution seen for 662 keV gamma ray photons interacting with a scintillator crystal is shown below in figure A.5.

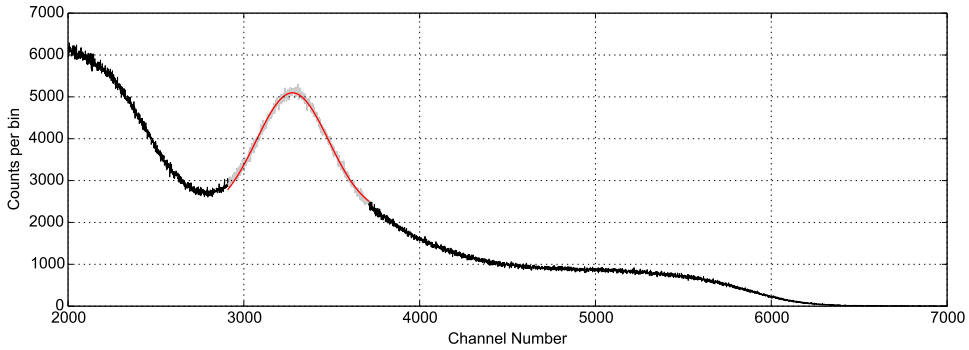

Figure 2.7: A typical energy spectrum for 662 keV gamma ray photons incident upon a scintillator crystal made of Cerium doped Lutetium Orthosilicate (LSO:Ce). The photopeak is fitted with a red line indicating a fitted Gaussian.

The apparatus and method to capture the above figure is shown in Appendix A.2. In the above figure we can see a Gaussian peak. This peak, which we will refer to as the photopeak, is the result of photoelectric interaction with the scintillator crystal. In this case the peak location corresponds to the energy deposited — 662 keV. The spread about this value is due to the finite energy resolution of the scintillator detector. The energy resolution is defined as $\frac{\Delta E}{E}$ where ΔE is the FWHM of the photopeak and E is the photopeak location. The energy resolution is discussed in the next chapter in greater detail in section 3.3.2.

In PET we are only interested in selecting events which interact by the photoelectric effect. Therefore we only consider events which have an energy close to the photopeak centroid. If this was not performed there would be an ambiguity in the time correlation between true events increasing noise in the final PET image.

2.2.3 Shape of the Scintillator Crystal

The shape of the scintillator crystal in PET is determined by three factors. These are tesellation, spatial resolution and sensitivity. These factors combine to ensure scintillator crystals are long,

thin cuboids. Due to the importance this will play later in the thesis we will discuss these three factors in greater detail.

Tessellation of Scintillator Crystals

Ideally there would be a one to one ratio of scintillator crystal to photodetector. However due to the high cost of photodetectors and complexity of circuitry required to connect thousands of scintillator detectors into a single system, this is not the case. Scintillator crystals are typically arranged in tesselated blocks connected to multiple photodetectors. Using Anger logic, relative light intensity between photodetectors, it is possible to determine which scintillator crystal an event occurred within. Therefore to maximise sensitivity and leave no gaps, scintillator crystals should be designed to tessellate.

Spatial Resolution of PET

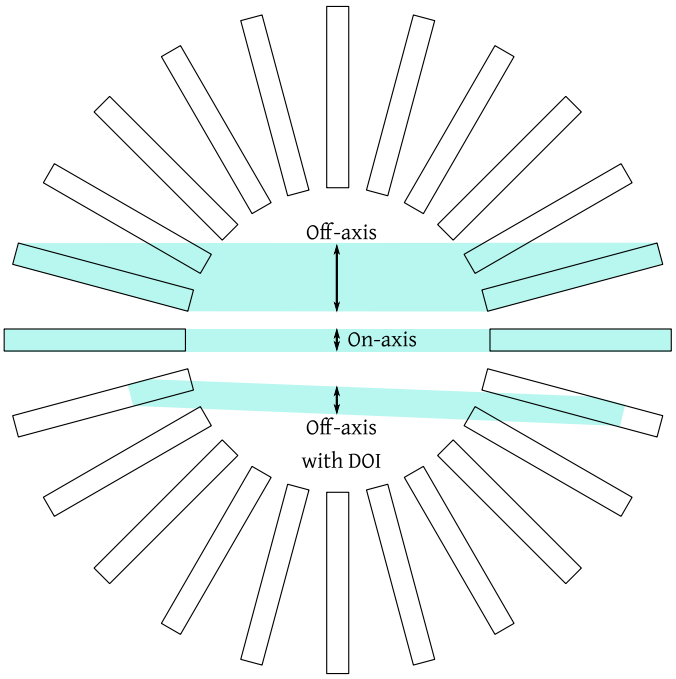

Figure 2.8: For a ring of scintillator detectors, three volumes due to lines of response are shown. These are the on-axis, off-axis and off-axis with depth of interaction (DOI) information.

The spatial resolution of images produced by PET will be limited by the 'width' of the scintillator crystal. Lines of response in fact define volumes of response. This is due to the finite size of the scintillator crystal as well as the ambiguity of gamma ray photon interaction position within the scintillator crystal. The effect can be seen in figure 2.8. Thinner scintillator crystals will therefore define thinner volumes. The scintillator crystals in this work are of the shape $2 \times 2 \times L$ mm^3. The 'pixel' size in this case is 2×2 mm^2.

Sensitivity of Scintillator Detectors

Longer scintillator crystals will interact with a greater proportion of gamma ray photons. The probability of a gamma ray photon interacting with the scintillator crystal follows an exponential decay of the form

$$F(z|E) = 1 - e^{-\sigma(E)\rho z} \tag{2.3}$$

where $F(z)$ is the probability of absorption after a distance z through a material with density ρ. σ is the (incident energy,E, dependent) total cross section of the material. LSO has a total cross section of 0.1173gcm^{-3} [21]. Combined with a density of 7.34gcm^{-3}, the attenuation length is calculated to be 12 mm at 0.511MeV. Using equation 2.3 a scintillator crystal of length 20 mm will interact with approximately 80% of incident gamma ray photons. The desire to capture as many gamma ray photons as possible is the primary reason to maintain long scintillator crystals in PET.

Ideally scintillator crystals would be sufficiently long to ensure all gamma ray photons are detected. However the overall performance of a PET scanner would be degraded if this was done. Firstly, longer scintillator crystals possess poorer timing performance than shorter [22]. This is due to increased variance in travel time from excitation position to the photodetector [23]. Experimental results in this area are presented in section 3.4. Secondly, in PET scintillator detectors are arranged in rings about the patient. In figure 2.8 lines of response will in fact define volumes of response. Compared to the on-axis case, the off-axis case has a higher volume. This is the parallax degradation to the spatial resolution. The parallax effect is compounded by longer scintillator crystals. To counter this knowledge of the DOI within a scintillator crystal would allow

a reduction in the spatial resolution.

2.2.4 Dual Decay Process

In the case of total absorption by the photoelectric effect, a gamma ray photon will generate N_0 electron-hole pairs[3] which is defined as

$$N_0 = E_\gamma \, \mathrm{LY} \tag{2.4}$$

where E_γ is the energy of the incoming gamma ray photon and LY is the scintillation yield. The subsequent recombination process in L(Y)SO is given by a chain of two decay processes; the relaxation of the electron-hole pairs into luminescent centres and their subsequent recombination causing the emission of a photon. These two processes can be modelled as a chain of two decays between levels 1, 2 and 3. This can be written as

$$\frac{dN_2}{dt} = -\frac{N_2}{\tau_2} + \frac{N_1}{\tau_1} \tag{2.5}$$

$$\frac{dN_2}{dt} = -\frac{N_2}{\tau_d} + \frac{N_0}{\tau_r} e^{-\frac{t}{\tau_r}} \tag{2.6}$$

where N is the number of scintillation photons produced at time t and τ_r, τ_d are the rise and decay constants respectively. For L(Y)SO these constants are 89 ± 13 ps and 43 ± 0.3 ns [24] respectively. It can be shown that equation 2.6 has the following solution [25]

$$N(t) = \frac{N_0}{\tau_d - \tau_r}(e^{-\frac{t}{\tau_d}} - e^{-\frac{t}{\tau_r}}) \tag{2.7}$$

2.2.5 Light Output at the Photodetector

The number of photons detected (N) by the photodetector, known as the light output, is related to the time resolution by a factor of $\frac{1}{\sqrt{N}}$ [16]. These are subsequently converted to photoelectrons and amplified. The resulting signal is analysed to give descriptive information about the incident particle. Namely the energy deposited and the time of incidence.

[3] Here we assume all electron-hole pairs recombine by radiative decay.

Algebraically we can express the number of photoelectrons generated, N, by

$$N = P_{DE} N_0 \tag{2.8}$$

$$N = L_{eff} E_\gamma \, \mathrm{LY} \tag{2.9}$$

where N_{ph} is the light output, P_{DE} is the photon detection efficiency and L_{eff} is the light extraction efficiency. The P_{DE} can be further split into

$$P_{DE} = \begin{cases} C_f P_{\mathrm{av}} F_f q_{eff} & \text{For SiPM} \\ C_f q_{eff} & \text{For PMT} \end{cases} \tag{2.10}$$

For the SiPM (Silicon Photomultiplier), C_f is the photodetector loss factor, P_{av} is the probability of causing an avalanche inside the photodiode, F_f is the fill factor, For the PMT (Photomultiplier Tube), C_f is the photodetector loss factor and q_{eff} is the quantum efficiency. The fill factor is due to the ratio of useful photosensitive area to the total area of the SiPM in contact with the scintillator crystal. Determining the size of each of these terms is difficult and beyond the scope of this work. We therefore assume the PMT used will have a P_{DE} of approximately 20% and a SiPM has one of approximately 10% This assumes a C_f of 1.

The maximum light output can be estimated by assuming all generated photons are collected — A L_{eff} of one. This corresponds to no bulk absorption, perfect reflectivity of all surfaces not in contact with the photodetector and no Fresnel losses from the coupling between scintillator crystal and photodetector. For a 0.511 MeV gamma ray photon incident upon LYSO the maximum light output is estimated to be 3800. This is due to a scintillation yield of 33,800 photons per MeV [26, LYSO] and an average quantum efficiency of 22% [27, Photonis XP2020 Q].

2.3 Summary

In this (brief) chapter we have covered the basics of scintillator detectors and their use in Positron-Emission Tomography. Additional background information will be given as chapters progress as the information is required.

Chapter 3

Direct Measurements

3.1 Introduction

3.1.1 Motivation

To begin we will explore the effect of γ interaction position upon the time and energy resolution of the scintillator detector. This is so we can better understand the contribution of optical light propagation through the scintillator crystal, light transport, upon the scintillator detector's performance. In this thesis we operate under the assumption that the contribution of the photodetector to the timing performance will continue to decrease over time. The variance of optical photon travel time, Δt, through a scintillator crystal of length L can be estimated to be

$$\Delta t = \frac{2nL}{c} \tag{3.1}$$

where n is the refractive index of the scintillator crystal and c is the speed of light. For a LYSO scintillator crystal with length 20 mm, this gives a variance of 240 ps. Equation 3.1 corresponds to an excitation at the photodetector end of the scintillator crystal. Half the light will travel through the scintillator crystal's length twice to again reach the photodetector (and detection). This effect is already larger than the photodetector contribution to the timing performance [28].

Prior work has looked into the light transport contribution upon the scintillator detector per-

formance [29–33]. In [34] the interaction position and its effect is explored for LSO and PMT combinations. This work shows timing performance degradation due to scintillator crystal length and surface finish. The degradation is attributed due to increased propagation delay due to dispersion at the lateral faces.

In this work we aim to see if the variation in the timing performance with interaction position for various scintillator crystal lengths. In this manner we wish to determine if the geometrical contribution is an averaging over multiple interactions, with regions of better performance, or if the geometrical contribution is independent of the interaction position.

3.1.2 Outline

As radiation sources and high quality photodetectors were required, both experiments were performed at CERN. Here expertise was provided by Dr. Stefan Gundacker and the PH-CMX group. The results from the DOI measurements were published in 2014 [8]. A description of the basic experimental procedure can be found in appendix A.1.

The depth of interaction (DOI), shown in figure 3.1, is the shortest distance to the photodetector from the Gamma ray photon (γ) interaction position. The DOI is a potential source of degradation to the timing and energy performance of the scintillator detector due to:

- Increased variance in the photon time-of-flight to the photodetector.
- Larger mean path length within the scintillator crystal to the photodetector could lead to increased surface light loss.

As discussed in the previous chapter, determination of the DOI is of importance for PET to negate or reduce the contribution of parallax error upon the spatial resolution [35,36]. If successful, longer scintillator crystals may be used leading to an improvement in the PET scanner's sensitivity and reduce overall scan times. Within monolithic scintillator detectors the same DOI information allows spatial confinement within the detector itself [37,38]. Thus potentially allowing more novel [39] [40] layouts and geometries.

In section 3.3 we begin by describing the standard and DOI coincidence apparatus. With this we describe the method utilised in both for analysing the raw data. In section 3.3.4, we use this method to characterise the $2\times2\times5$ mm^3 Agile Ca-co-doped LSO:Ce scintillator crystal used as the reference

scintillator detector. Once this is accomplished the CTR with L is explored with the standard coincidence apparatus using two identical $2 \times 2 \times L$ mm^3 Proteus LYSO:Ce scintillator crystals in section 3.4. Measurements conducted using the DOI coincidence apparatus are reported in section 3.5.2. In all measurements we explore the contribution of material, geometry and wrapping for polished scintillator crystals. PTFE (Teflon) tape is commonly used as the wrapping material for scintillator crystals due its high reflectivity, ease of application and importantly its diffusive properties. It should be noted however that PTFE is not used in commercial scintillator detectors due to the large number of layers required about each scintillator crystal. This would reduce the effective sensitivity. In these cases diffusive paint, such as Barium Sulphate ($BaSO_4$), would be utilised.

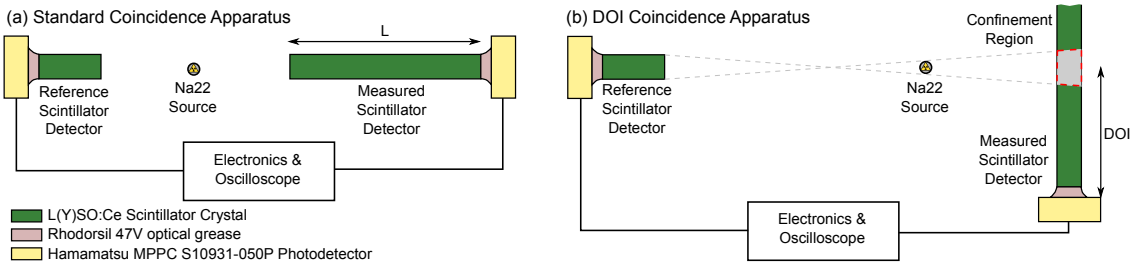

Figure 3.1: The two timing coincidence apparatuses. In (a) the standard coincidence apparatus, used in this chapter to measure the timing performance with the scintillator crystal length, L is shown. In (b) the depth of interaction (DOI) coincidence apparatus is seen. In this, the measured scintillator detector is rotated 90 degrees, with respect to the reference scintillator detector. In the standard coincidence apparatus the Na22 source is placed equidistant between the two scintillator detectors, whereas in the DOI coincidence apparatus the source is placed much closer to the measured scintillator detector. This leads to electronic collimation forming a confinement region within the measured scintillator detector. The confinement region is shown in grey surrounded by a red dashed line.

3.2 Scintillator Crystal Samples

Two scintillator crystal materials were used for measurements at CERN. The first is LYSO:Ce purchased from Proteus [41], which have been shown to be of excellent quality [22]. The second material used is Agile Ca co-doped LSO:Ce, known as LSO:CeCa. These have been shown to have a higher light output and faster decay time [42]. The light output being 22,000 MeV^{-1} for LSO:Ce compared to 25,000 MeV^{-1} for LSO:CeCa. As well as the decay time being 43 ns for LSO:Ce

compared to 31ns for LSO:CeCa [43]. The scintillator crystals used, and the names we will refer to them as, are given in table 3.1. All scintillator crystals were coupled to the photodetectors using the optical grease, Rhodorsil 47V [44] to improve light output.

Table 3.1: Scintillator crystals used in CERN experiments. L is the length of the scintillator crystal with values of 5, 10, 15, 20 and 30 mm. This gives a total of 10 LYSO:Ce scintillator crystals used.

Key	Material	X (mm)	Y (mm)	Z (mm)
LA	LYSO:Ce	2	2	$5 < L < 30$
LB	LYSO:Ce	2	2	$5 < L < 30$
ref5A	LSO:CeCa	2	2	5
ref5B	LSO:CeCa	2	2	5
Ca20	LSO:CeCa	2	2	20

3.3 Experimental Method

3.3.1 Description of Apparatus

The timing coincidence apparatus is comprised of two Hamamatsu MPPC S10931-050P SiPMs connected to CERN-developed NINO leading-edge discriminators via analogue amplifiers. The energy and timing information of individual pulses are collected using a LeCroy DDA 735Zi high-bandwidth oscilloscope. Our coincidence apparatus is held within a temperature-controlled chamber to maintain stability of photodetector performance. The first five minutes of each measurement are discarded due to any potential error introduced by temperature variation. This period was determined to be sufficient for the temperature in the chamber to stabilise.

Scintillator crystals are coupled to the SiPM photodetectors using Rhodorsil 47V optical grease to improve light output. The refractive indices of LYSO:Ce and the optical grease are approximately 1.8 [45] and 1.4 [44][1] respectively. Wrapped scintillator crystals are tightly bound in many layers of PTFE tape to ensure good coupling between the scintillator crystal and wrap and minimise transmission losses. Prior to wrapping and usage, all scintillator crystals are cleaned using isopropyl alcohol. Furthermore all scintillator crystals are handled with carbon-tipped tweezers. Both of the above are done as they can degrade the performance of the scintillator crystal.

The optimal threshold and bias values of the SiPMs were determined by parameter sweep and

[1] The difference between this and the glass or plastic window of the photodetector is typically considered negligible.

Table 3.2: Main SiPM parameters used for standard and DOI timing coincidence measurements.

	Bias (V)	Overvoltage (V)	Threshold (V)
Left Detector	72.6	2.2	1.64, 1.56
Right Detector	72.7	2.2	1.64, 1.56

are given in table 3.2. A thorough description of the experimental method can be found in [46].

3.3.2 Processing Data from Coincidence Apparatus

The positron emission from the Na22 source will generate two 0.511MeV gamma ray photons in opposition correlated in time. By selecting for events which interact solely by the photoelectric effect we ensure that the incident gamma ray photon has interacted with matter only once. Therefore if two gamma ray photons are detected in opposition within a small time window, it is highly likely they are from the same electron-positron annihilation. It is this 'electronic collimation' timing property which ensures we only record events from within the confinement region. These events are found by selecting the subset of interactions which fall within 2σ of the photopeak centroid of their respective energy spectra. This narrow range is chosen to drastically reduce the contribution of overlapping Compton interactions. When two gamma ray photons are detected within their respective photopeak energy ranges, as well as within a nanosecond of each other, the relative time delay between the two is recorded. For many such true events the relative difference in arrival time is histogrammed producing a Gaussian distribution known as the (relative) delay peak. The FWHM of any Gaussian is related to its standard deviation (σ) by

$$\text{FWHM} = 4\sqrt{\ln 2}\sigma \tag{3.2}$$

For two identical photodetectors the FWHM of the delay peak is defined as the coincidence time resolution (CTR) (see Appendix A.1.1 for more information), such that

$$\text{CTR} = 2\sqrt{2\ln 2}\sigma_{\text{measured}} \tag{3.3}$$

where σ_{measured} is the scale parameter measured from the delay peak and σ is the time resolution of the scintillator detector. This relationship holds because the delay peak is formed from the

convolution of two Gaussian distributions. Each distribution corresponds to the delay peak of each individual scintillator detector. In cases where we use a reference scintillator detector with a known time resolution, the CTR of an unknown scintillator detector is determined by subtraction in quadrature and a subsequent scaling such that

$$\sigma = \sqrt{\sigma_{\text{measured}} - \sigma_{\text{ref}}^2} \tag{3.4}$$

$$\text{CTR} = 4\sqrt{\ln 2}\sqrt{\sigma_{\text{measured}}^2 - \sigma_{\text{ref}}^2} \tag{3.5}$$

where σ_{ref} is the (known) reference time resolution. All CTR values in this chapter are given in picoseconds.

The energy resolution, σ_E, is defined as

$$\sigma_E = \frac{\Delta E}{E} \tag{3.6}$$

where ΔE is the FWHM of the photopeak with centroid E. The energy resolution is typically given as percentage. The two main contributions to the energy resolution are variance in the gain of the photodetector used and variance in the light output for a fixed energy input into the scintillator crystal.

3.3.3 Analysis of Data

The parameters describing the location and scale of the Gaussian distributions (the photopeaks and delay peak per measurement) were found by weighted least-squared fit. The error per bin was assumed Poissonian and taken as the square root of the number of measurements per bin. The standard error in the fit parameters were determined by the bootstrap method [47]. The full code used to perform the peak detection, peak fitting, parameter error determination and image & table generation can be found at https://github.com/marksbrown/ProcessingCTRData.

3.3.4 Reference Detector Measurements

Using two identical reference scintillator crystals (ref5A, ref5B) the CTR was determined using both the standard and DOI coincidence apparatuses. The key values from the measurements are

Table 3.3: Coincidence time resolution values for two identical polished $2 \times 2 \times 5$ mm^3 Ca-co-doped LSO:Ce wrapping in PTFE tape for standard and DOI measurements. χ_{Reduced} is the reduced chi-squared fit to the delay peak distribution.

Coincidence Apparatus	Left Energy Resolution (%)	Right Energy Resolution (%)	Detected true Events	Delay Peak Centroid (ps)	σ_{ref} (ps)	CTR (ps)
Standard	7.8±0.1	9.8±0.1	637±25	-77.5±2.3	39.3±1.2	131.0±4.0
DOI	10.5±0.1	12.7±0.1	1498±39	-14.0±1.5	39.6±0.9	132.0±2.9

shown in table 3.3 as time resolution and as CTR values. We note that the CTR from both measurements are in agreement. The CTR value from the standard coincidence measurement is in agreement with a prior measurement in [Table 2] [48] of 123±7 ps. For the remaining measurements the reference detector CTR is taken as 131 ± 4 ps unless otherwise stated.

3.4 Standard Coincidence Apparatus Results

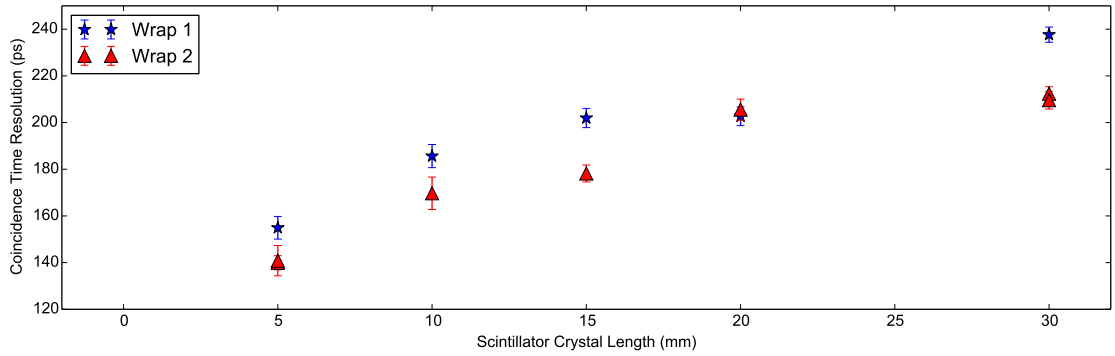

Figure 3.2: The CTR with scintillator crystal length is plotted for Proteus LYSO:Ce scintillator crystals of lengths 5, 10, 15, 20 and 30mm. All crystals possess a cross section of $2 \times 2 \times$ mm^2.

Standard coincidence measurements are made of the Proteus LYSO:Ce scintillator crystals listed in table 3.2. Two identical crystals, which are referred to as LA and LB, of each length are placed into opposing, identical, scintillator detectors. The CTR is then determined as the FWHM of the delay peak directly. In figure 3.2 we see the expected degradation of the CTR with increasing crystal length [22, 49–51] [52]. The full set of results are given in table 3.4. In these measurements the wrapping was reapplied by a second individual and the measurement retaken. These are referred

Table 3.4: Standard coincidence apparatus measurements for two identical polished Proteus LYSO:Ce scintillator crystals wrapped in PTFE tape. All crystals have a cross section of 2×2 mm^2. χ^2_{Reduced} is the reduced chi-squared fit to the delay peak.

Wrapped By	length (mm)	Left Energy Resolution (%)	Right Energy Resolution (%)	Detected true Events	Delay Peak Centroid (ps)	CTR (ps)
Wrap 1	5	7.05±0.07	9.44±0.09	856±29	-68.8±2.4	154.9±4.9
Wrap 2	5	6.33±0.08	7.36±0.09	361±19	-68.8±3.4	140.8±6.5
Wrap 2	5	6.89±0.05	7.29±0.05	1526±39	-64.8±1.6	139.9±3.0
Wrap 1	10	8.24±0.06	9.63±0.07	1032±32	-124.4±2.6	185.6±5.0
Wrap 2	10	6.66±0.05	7.59±0.05	515±23	-168.4±3.6	169.7±7.0
Wrap 1	15	9.05±0.05	9.07±0.05	1875±43	-176.0±2.1	201.9±4.1
Wrap 2	15	6.82±0.04	7.67±0.04	1569±40	-108.8±2.0	178.2±3.6
Wrap 1	20	10.97±0.05	9.85±0.05	1731±42	-85.2±2.2	202.7±4.0
Wrap 2	20	6.99±0.03	9.27±0.04	2003±45	-131.1±2.1	205.5±4.5
Wrap 1	30	10.94±0.04	13.07±0.06	3382±58	-58.6±1.8	237.7±3.3
Wrap 2	30	9.73±0.04	10.79±0.05	3502±59	-70.6±1.6	212.4±3.0
Wrap 2	30	9.52±0.05	10.72±0.06	2369±49	-67.9±1.9	209.6±3.8

to as 'wrap 1' and 'wrap 2'. Finally for the 5 mm and 30 mm the measurement is repeated by the same person. These steps were performed to determine the size of the contribution to the CTR introduced by the individual involved. We see that the 'quality' of the wrapping leads to a large systematic variation that must be carefully taken into account for measurements to be validly compared between scintillator crystals. One potential explanation of this result is presented in Section 6.2. Given that we also see a shift in the delay peak centroid between these measurements, we would conclude correct alignment upon the SiPM is also vital.

Also in table 3.4 we see that the energy resolution (%), for both left and right scintillator detectors, is poorer at higher L. This is due to increased variance in the total energy recorded. The light output per detected γ is reduced with L; likely due to increased path length of photons through the scintillator crystal. Also note that each measurement was conducted for 15 minutes each. Finally notice that the number of true events detected increases with L for the same time period (15 minutes) per measurement. This is due to the increasing volume of scintillator crystal within the confinement region defined by electric collimation. This leads to an increased sensitivity as expected.

3.5 Depth Of Interaction Coincidence Apparatus Results

3.5.1 Overview

The standard coincidence apparatus, as shown in figure 3.1 on page 33, is altered in two key respects. Firstly the right photodetector is placed within a 3D-printed clamp. This is designed to hold the scintillator crystal vertically with respect to the reference detector. Secondly the Na22 source is placed much closer to the vertically aligned scintillator detector than the reference. As in the standard apparatus both scintillator crystals are coupled to their respective photodetectors, Hamamatsu MPPC S10931-050P SiPMs, using Rhodorsil 47V optical grease.

The size of the confinement region is primarily determined by the separation distances between scintillator detectors and the Na22 source. The Na22 source is placed 5 mm from the scintillator crystal under investigation. The reference scintillator detector is a further 40 mm on the opposite side from the source, unless otherwise stated. As the Na22 source has a finite size of 1 mm^3, this defines the minimum size of the confinement region. For a source much closer to the scintillator detector under interest than to the reference detector, the confinement region will tend to the diameter of the source.

To determine the size of the confinement region experimentally we can exploit the relationship between the confinement region and volume of scintillator crystal discussed in section 3.4. Namely that there will be a fixed number of events per unit time if the volume of scintillator crystal does not change. For the same measurement and same confinement region we can assume a uniform number of events, regardless of DOI. Theremore if the confinement region passes outside the scintillator crystal, the number of true events recorded will drop until electronic collimation prevents any true events from being detected. In this we assume good alignment of the scintillator crystal with respect to the central axis of the DOI coincidence apparatus. We represent this described behaviour as a convolution between a uniform distribution and a Gaussian distribution. The uniform distribution is chosen as we do not expect the rate of interaction to change with DOI since the volume of scintillator crystal exposed via electronic collimation does not change. The Gaussian distribution is an estimate of the cross section of the electronic collimation expected. The uniform distribution has a width corresponding to the scintillator crystal length and an amplitude corresponding to the mean number of detected true events. The FWHM of the normal distribution corresponds to the

confinement region; In this case taken as 1 mm. As shown in figures 3.3 and 3.8 as a black-dotted line this is a valid assumption for our apparatus.

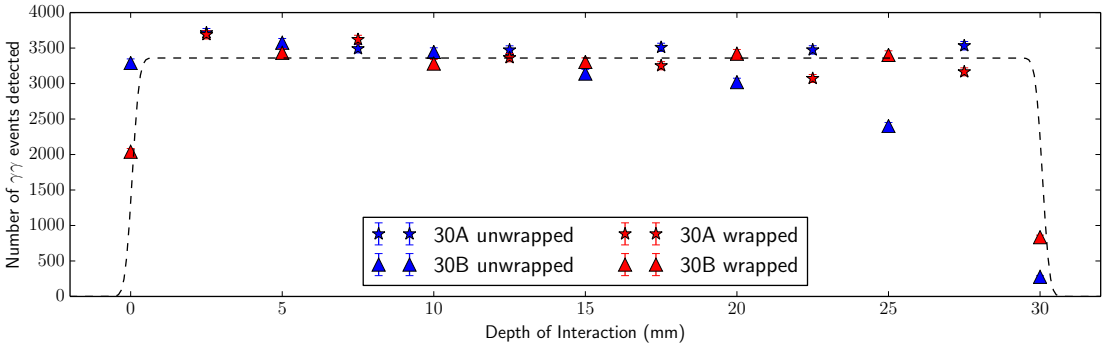

Figure 3.3: The number of true events recorded with DOI for two Proteus $2\times2\times30$ mm^3 LYSO:Ce scintillator crystals. A uniform distribution convolved with a Gaussian distribution with FWHM of 1 mm is plotted as a dashed black line.

3.5.2 30 mm DOI Results

CTR Results

CTR measurements are performed twice using two identical polished Proteus LYSO:Ce $2 \times 2 \times 30$ mm^3 scintillator crystals. These scintillator crystals, the 30A and 30B, are measured at DOI values between 0 and 30 mm in 2.5 mm increments alternating between the two scintillator crystals. By using two scintillator crystals in this fashion we are attempting to determine any systematic contribution due to differences in coupling, alignment and surface finish. To determine the contribution of wrapping material, each measurement is repeated with and without PTFE (Teflon) tape. Measurements with complete wrapping will referred to as the wrapped configuration. Likewise no wrapping is referred to as the unwrapped configuration. Each 30 mm measurement was taken for 54 minutes each. As in the standard coincidence measurements, the first 5 minutes prior to data collection are ignored to ensure temperature stability within the sealed apparatus box.

Table 3.5: Mean values for energy and timing performance of 30 mm DOI measurements. Results are grouped by sample and configuration. χ^2_{nofit} refers to the reduced chi-squared of fitting the weighted mean to the data.

SampleB configuration	Right Energy Resolution (%)	Detected true Events	Delay Peak Centroid (ps)	CTR (ps)	χ^2_{nofit}
30A unwrapped	15.76±0.02	3532±24	316.9±0.7	260.7±2.2	3.4
wrapped	13.84±0.02	3360±24	321.4±0.6	246.0±2.3	3.6
30B unwrapped	17.17±0.03	2735±20	306.0±1.3	256.9±5.3	0.6
wrapped	13.98±0.02	2816±20	293.6±0.8	231.7±2.9	1.7

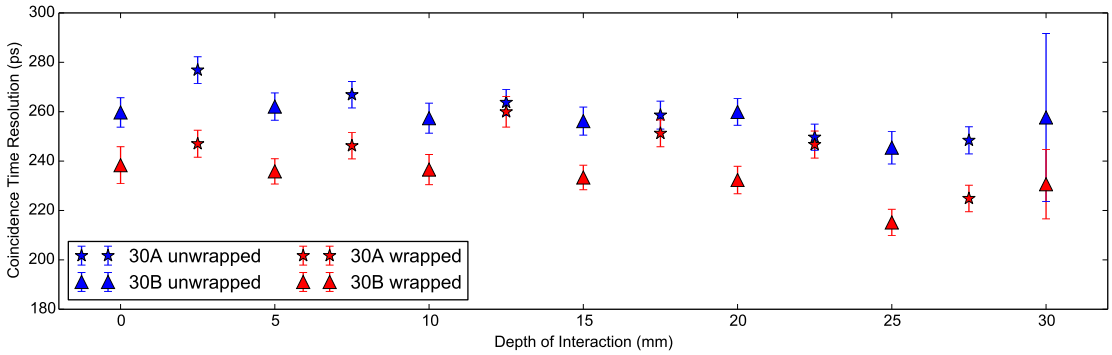

Figure 3.4: Coincidence time resolution (CTR in ps) versus the depth of interaction (DOI in mm) for for two Proteus $2 \times 2 \times 30$ mm^3 LYSO:Ce scintillator crystals in the wrapped and unwrapped configurations. Measurements are alternated with increasing DOI to check for any systematic error introduced by individual scintillator crystals.

In figure 3.4 the CTR (in ps) against DOI (in mm) per sample and configuration is given. In table 3.5 the values given for the timing and energy performance are averaged across the DOI. Firstly we note that no clear relationship between CTR and DOI is visible. The reduced chi-squared fit shows values close to unity for fitting to the weighted mean, indicating no relationship between CTR and DOI in both crystals and configurations. Secondly the CTR measurements from the wrapped configuration are consistently better than those from the unwrapped. The differences between the configurations being 8±5 ps and 18±6 ps for 30A and 30B respectively. The magnitude of this difference is much smaller than that which we would expect in the standard CTR measurement. For instance it is seen in [Table IV] [22] that the difference in the CTR between wrapped and unwrapped configurations is approximately 33%. The only difference between the standard and DOI coincidence apparatus is the size of the confinement region. Our measurements

therefore imply that knowledge of the excitation position within the standard coincidence apparatus for an unwrapped scintillator crystal would reduce the measured CTR by at least 25%. We would predict this behaviour is due to a reduction in the variance of the photon travel time to the photodetector across multiple events.

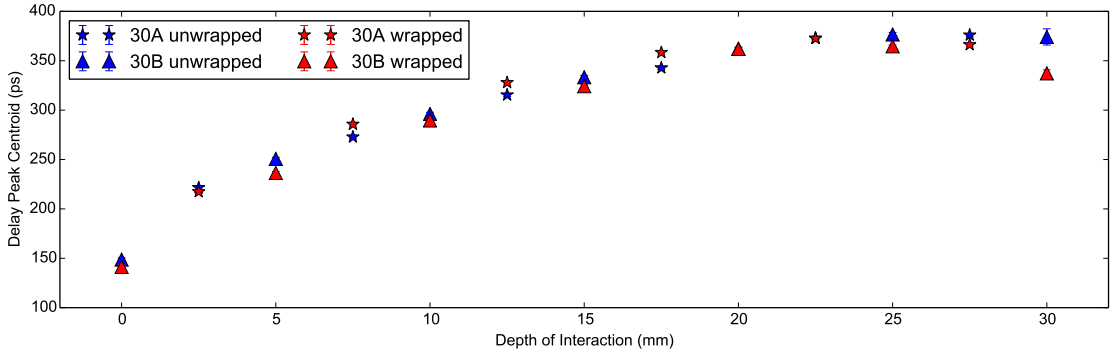

Figure 3.5: The delay peak centroid versus the DOI plotted for for two Proteus $2 \times 2 \times 30$ mm^3 LYSO:Ce scintillator crystals in the unwrapped and wrapped configurations. The plataeu is seen in all measurements at approximately 20 mm.

Additional timing and energy results for 30 mm

In the coincidence apparatus measurements additional properties are recorded; namely the delay peak centroid, the light output and the energy resolution. In figure 3.5 the shift in the delay peak position with increasing DOI is plotted. It can be seen that a plateau is reached for both configurations at 20 mm. In [53] this plateau is attributed to the travel time between photons travelling 'towards' and 'away' from the photodetector approaching equality. As the electronic trigger from the discriminator is tuned as close to the beginning of the signal as possible this cannot come before generated light has physically travelled from it's emission position to the photodetector. This idea is supported by the total shift seen of 150ps to 370ps corresponding to an approximate physical distance of 30 mm.

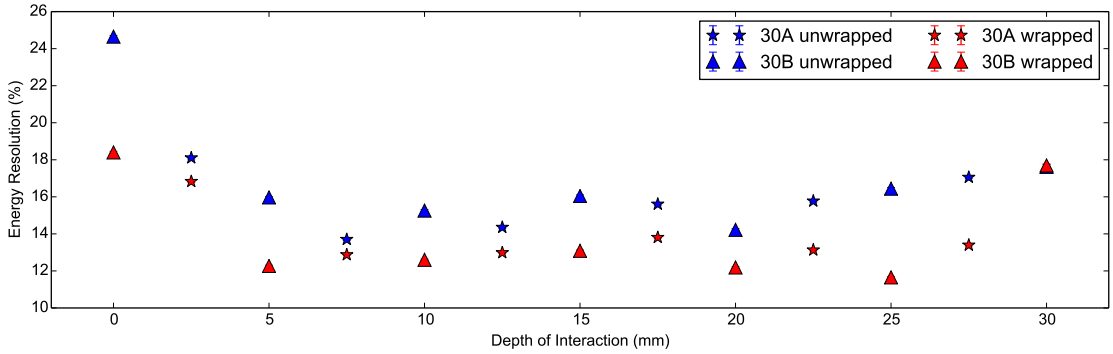

Figure 3.6: The energy resolution (%) versus the DOI plotted for two Proteus $2 \times 2 \times 30$ mm^3 LYSO:Ce scintillator crystals in the unwrapped and wrapped configurations. For a DOI greater than 5 mm, the mean energy resolutions are 16.52±0.02 % and 13.92±0.01 % for the unwrapped and wrapped configurations respectively.

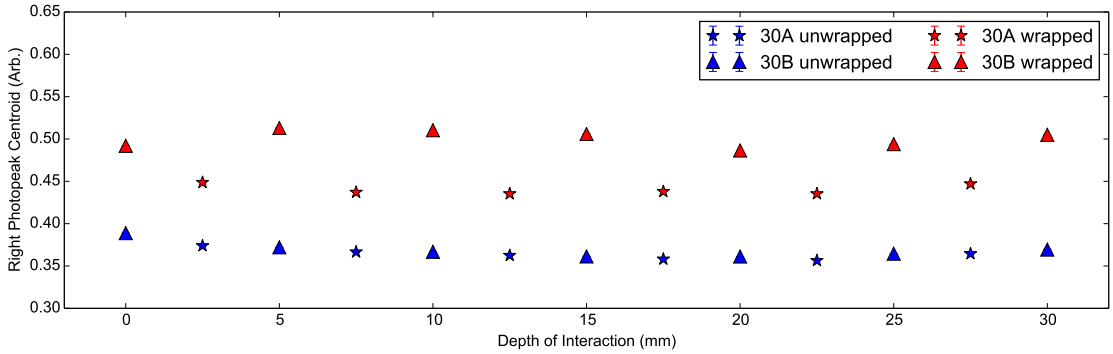

Figure 3.7: The right photopeak centroid versus the DOI for two identical scintillator crystals of shape $2 \times 2 \times 30$ mm^3 in the wrapped and unwrapped configurations. The right photopeak centroid corresponds to the absolute light output of the scintillator detector under investigation.

In figures 3.6 and 3.7 we can see the energy resolution and right photopeak centroid of the scintillator detector with DOI. The photopeak centroid corresponds to the absolute light output arriving at the photodetector. Firstly we see the light output and energy resolution are better in the wrapped configuration compared to the unwrapped for both scintillator crystals as expected. For a DOI greater than 5 mm, the mean energy resolutions are 16.52±0.02 % and 13.92±0.01 % for the unwrapped and wrapped configurations respectively. Secondly we notice that the wrapped measurements show a systematic variation in the photopeak centroid, most likely due to differences

in wrapping or coupling. Interestingly this pattern is also observed in figure 3.4 showing a poorer CTR for the '30B Wrapped' compared to the '30A Wrapped'. Thirdly we notice that the light output is approximately 20 % higher in the wrapped configuration with a minor drop off in both configurations for increasing DOI. We attribute this to longer path lengths through the scintillator crystal at higher DOI and therefore a greater chance of escape via Lobe reflection [54] or losses via absorption. In all measurements the energy resolution is seen to be at its poorest for low DOI values, despite a weak variation seen in the light output. This indicates a broadening of the photopeak at low DOI values as no large change in the absolute light output is observed. Given that this broadening occurs only at low DOI this implies the cause is due to the geometry of the scintillator crystal. Essentially, at low DOI the solid angle of γ-generated light reaching the photodetector without interacting with the side faces is high.

3.5.3 20 mm LSO:CeCa Measurements

To determine to what degree the material and scintillator crystal length contributes to the timing and energy performance we repeat the 30 mm measurements with a $2 \times 2 \times 20\text{mm}^3$ Agile Ca-co-doped LSO:Ce scintillator crystal. Additionally we consider a third 'partially wrapped' configuration; namely that we wrap the side faces but leave the face opposing the photodetector unwrapped. In doing so we expect to significantly reduce the contribution to the light output from the backwards reflecting mode. Aside from reducing the total light output, we wish to determine if the backwards reflecting mode has an effect upon the scintillator detector performance. For the 20 mm measurements, each measurement is collected for 90 minutes — An increase over the 30 mm measurements. This is done to counter the reduced sensitivity for shorter crystals and reduce the error in the delay peak fitting.

CTR Results

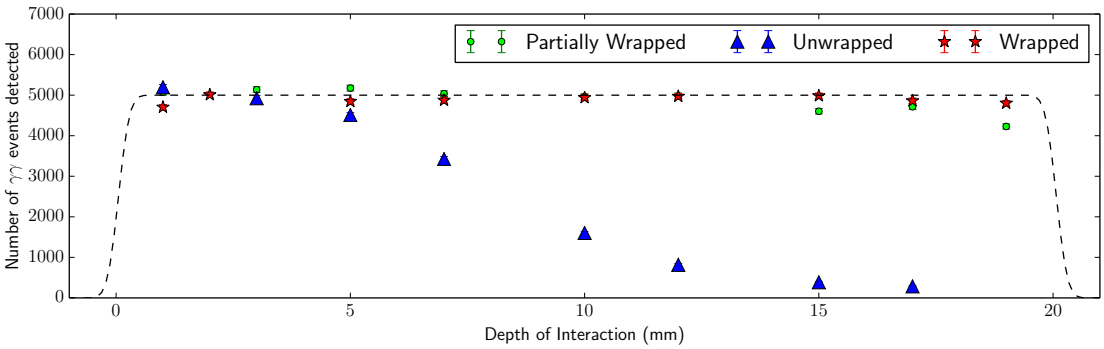

Figure 3.8: Three configurations shown for a $2 \times 2 \times 20$ mm^3 LSO:CeCa scintillator crystal. In this we see that the partially wrapped and wrapped configurations shown good alignment, whereas the unwrapped shows poor. This will result in fewer events being collected and thus a larger error in higher DOI measurements.

In figure 3.8 the number of detected true events is constant with DOI except for the unwrapped configuration. In this case we see a gradual drop off in the number of true events recorded with increasing DOI. This is due to poor vertical alignment of the scintillator crystal leading to the confinement region drifting outside the scintillator crystal. In figure 3.9 we see that this results in an increasingly larger error in the CTR until not enough events are collected to accurately determine the value at all. Even so, we find that poor alignment whilst degrading the error in the measurement, does not introduce a systematic shift into the CTR. Thus as long as the number of true events collected is sufficiently high then poor alignment will not affect the CTR recorded.

Table 3.6: Mean values for energy and timing performance of 20 mm DOI measurements. Results are grouped by sample and configuration. χ^2_{nofit} refers to fitting the weighted mean to the data.

Configuration	Right Energy Resolution (%)	Detected True Events	Delay Peak Centroid (ps)	CTR (ps)	χ^2_{nofit}
unwrapped	19.99±0.03	3412±24	148.9±0.9	240.0±3.5	1.1
partialwrap	17.27±0.02	4879±23	162.9±0.4	222.1±1.5	2.0
wrapped	14.20±0.01	4887±23	128.7±0.4	198.3±1.5	1.5

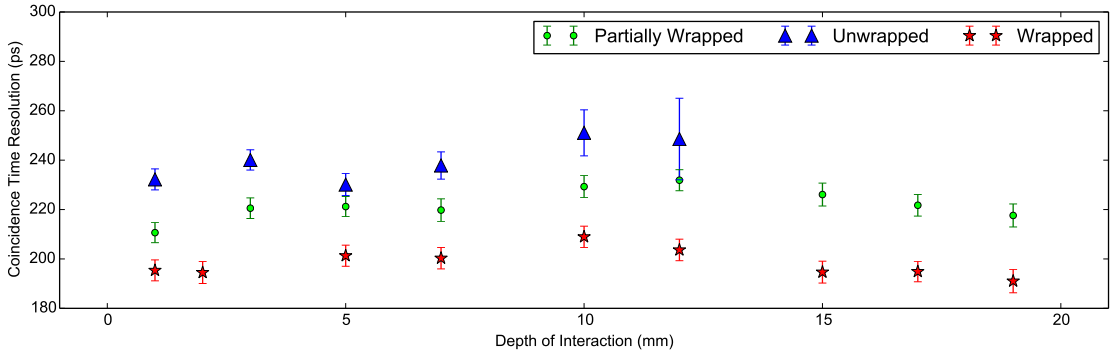

Figure 3.9: The CTR is plotted versus the DOI for three configurations of a $2 \times 2 \times 20$ mm^3 LSO:CeCa scintillator crystal.

In figure 3.9 we see the CTR improves with increasing amounts of wrapping by 20 ps; from unwrapped, to partially wrapped and finally to wrapped.

This is predominantly due to increased light output. These measurements have lower individual CTR errors than the previous 30 mm measurements, likely due to a greater number of true events recorded. These being approximately 5000 for LSO:CeCa compared to 3400 for LYSO:Ce; where these numbers are taken from figures 3.8 and 3.3 respectively. As the volume of the confinement region within the scintillator crystal is the same in both measurements this difference is primarily due to the difference in measurement time. The wrapped CTR is 198 ± 2 ps compared to 176±7 ps for the standard coincidence measurement given in [Table 2] [48]. For an equivalent $2 \times 2 \times 20$ mm^3 Proteus LYSO:Ce scintillator crystal a CTR of 202.7±4.0 ps in standard coincidence is observed. As expected, we see that LSO:CeCa timing performance is superior to that of LYSO:Ce.

In both the 20 mm and the 30 mm measurements we see that the CTR is worse in the DOI timing coincidence apparatus than in the standard. For the 30 mm measurements the CTR is

209.6±3.8 ps for the standard coincidence. In the DOI coincidence apparatus the mean CTR is 231.7±2.9 ps. These are the two closest values from their respective experiments, indicating a minimum non-negligible degradation of 10±2%. As the components and SiPM parameters, given in table 3.2, are the same in both the standard and DOI coincidence apparatus, we would conclude this difference is due to the confinement region.

Additional timing and energy results for 20 mm

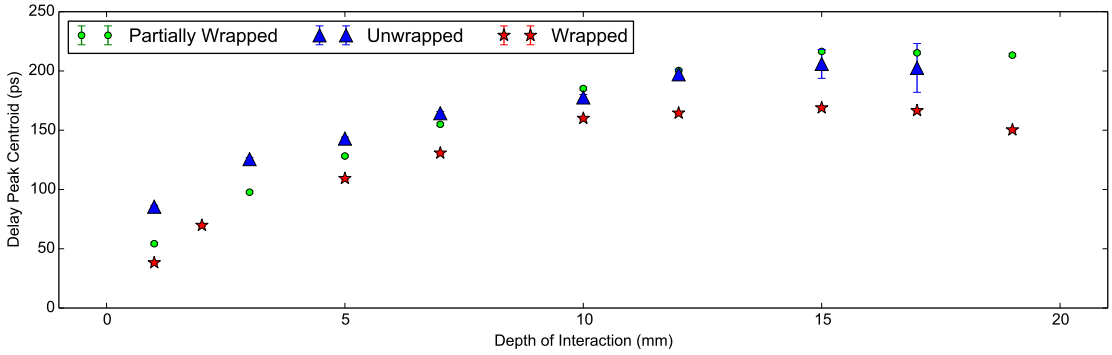

Figure 3.10: The delay peak position with DOI is plotted for a LSO:CeCa scintillator crystal of shape $2 \times 2 \times 20\text{mm}^3$ for the unwrapped, partially wrapped and wrapped configurations.

In this section we look at the energy performance of the 20 mm scintillator crystals under the three configurations described in the previous section. In figure 3.10 the delay peak position with DOI is seen to possess the same plateau as observed in the 30 mm measurements. In this case the plateau is reached close to 10 mm for the wrapped measurements. As in the 30 mm measurements, the peak to peak range in the delay peak centroid is comparable to the scintillator crystal length. We can conclude therefore that the shift is predominantly dependent upon the length of the scintillator crystal.

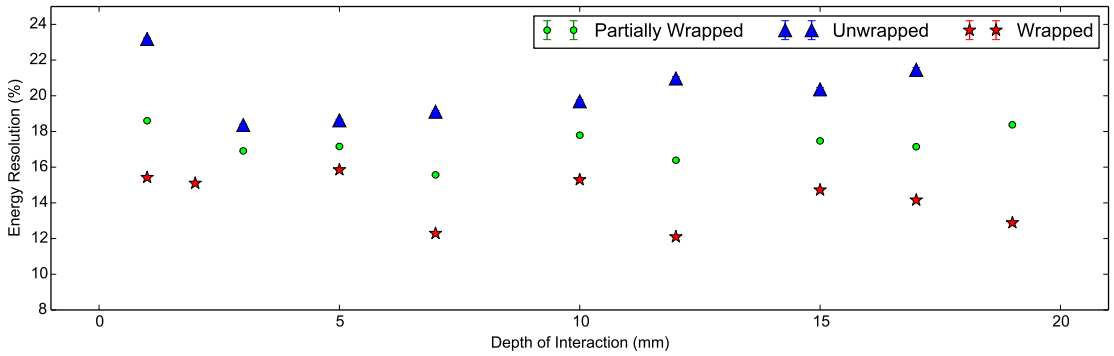

Figure 3.11: The energy resolution (%) for a LSO:CeCa scintillator crystal of shape $2 \times 2 \times 20\text{mm}^3$ for the unwrapped, partially wrapped and wrapped configurations.

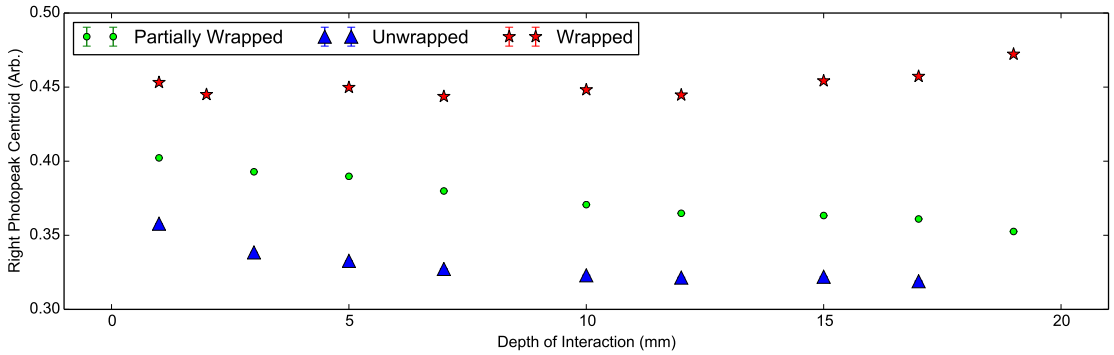

Figure 3.12: The right photopeak centroid plotted against the depth of interaction for a LSO:CeCa scintillator crystal of shape $2 \times 2 \times 20\text{mm}^3$ for the unwrapped, partially wrapped and wrapped configurations. The photopeak centroid corresponds to the light output of the scintillator detector.

In figures 3.11 and 3.12 we see the energy resolution and light output of the 20 mm measurements with DOI. As expected the wrapped measurements demonstrate the lowest energy resolution and the highest light output. At low DOI the energy resolution is at its poorest and the light output is at its highest regardless of configuration. This implies light transport through the scintillator crystal leads to surface losses. As the unwrapped configuration shows the largest drop in light output with DOI, this indicates the predominant loss is through the side faces.

3.6 Discussion

3.6.1 Analysis of results

The evidence presented this chapter lends itself to the conclusion that no relationship, within experimental error, was found between the CTRand DOI. This result is in agreement with reference [55] for polished scintillator crystals. The mean CTR recorded from the DOI coincidence apparatus was consistently poorer than equivalent measurements performed using the standard coincidence apparatus. This was despite the same equipment being employed in both experiments. In additional measurements, given with the full data to found in supplementary material of the research paper [8], we conclude this is not due to the threshold or bias values selected. Futhermore no difference between the standard and DOI measurements was seen in the reference scintillator detector CTR values, given on page 36. We therefore conclude the confinement region for long wrapped scintillator crystals has a negative effect upon the CTR. As the main physical change between the standard and DOI measurements is the variance in light transport within the scintillator crystals, it is logical to conclude this is the property responsible.

The results presented in [Figure 8] [53] show the delay peak centroid with DOI shifting in the same manner as presented in figures 3.5 and 3.10. In reference [53] the gradient of the delay peak centroid with DOI is presented as an effective refractive index. This effective refractive index (n) is defined as $n = mc$ where m is the gradient of the fitted line (in SI units) and c is the speed of light. For the 30 mm DOI measurements, where we fit to a subset of the delay peak centroid data with DOI below 20 mm, we find 3.6±1.5 and 3.4±1.2 for the unwrapped and wrapped configurations respectively. For the 20 mm measurements, where we fit to a subset of the delay peak centroid data with DOI below 10 mm, we find 3.9±1.0, 5.0±0.6 and 4.4±1.1 for the unwrapped, partially wrapped and wrapped configurations respectively. In reference [53] a value of 3.9 is presented for polished LSO:Ce scintillator crystals. This is in good agreement with our calculated values. Of particular note is the higher values of n for the partially and fully wrapped configurations in comparision to the unwrapped. Physically we are seeing that with the presence of wrapping the mean propagation time for photons through the scintillator crystal has increased. The curve shape itself is predominantly attributed to finite propagation time of information through the scintillator crystal. Given that the plateau occurs at high DOI we would conclude that the variation in the

time between the forward and backward modes[2] becomes negligible and as such no longer moves the delay peak.

The light output and energy resolution are seen in both the 20 mm and 30 mm measurements to degrade weakly with increasing DOI. This behaviour is attributed to losses from a higher path length through the scintillator crystal. The severe penalty in the energy resolution at very low DOI we attribute to the large potential variation in energy confinement across the photodetector. At higher DOI the light reaching the photodetector is more even across the photodetector face and thus more consistently detected.

It can also be seen that the mean energy resolution in the DOI measurements (beyond low DOI gives a mean of 14%) is higher than the comparable measurement for the standard apparatus (an average of approximately 12%) for identical scintillator crystals. This discrepency of 3% is harder to explain. Minor changes to the calibration of the photodetectors could explain this change however further study will be required to determine if this is so.

3.6.2 Implication of Results

There are four key results we can conclude from the measurements presented in this chapter

1. There is no relationship between the interaction position within the scintillator crystal and the timing performance.
2. The time resolution is poorer in longer scintillator crystals.
3. Usage of diffusive wrapping increases the measured light output from a scintillator detector.
4. The quality of wrapping will lead to significant variation in the recorded CTR.

[2]See section 5.6 for a description of modes in scintillator crystals

Chapter 4

Indirect Measurements

4.1 Introduction

Outline

In the previous chapter it was seen that geometry and surface effects are capable of degrading the timing performance of scintillator detectors. Specifically it was shown that, within experimental error, there was no relationship between the interaction position within the scintillator crystal and the timing performance. However we did find that the timing performance does degrade with quality of wrapping and in longer scintillator crystals. Clearly there is some effect at play affecting the performance which is related to the light transport. The measurements performed in this chapter look at effects which alter light propagation through the scintillator crystal — indirect determination of factors affecting the timing performance.

In this chapter we explore these effects in greater detail via optical measurements performed at UCL. This is done with the aim to determine if there is any variation with interaction position. Our ultimate aim is to place further constraints on the effects observed in the previous chapter on the timing performance of scintillator detectors. It is hoped that such measurements will allow key limitations underpinning the scintillator detector performance to be exposed and hopefully identify target areas for improvement.

Measurements performed in this chapter fall into two groups — Timing and scattering. In Sec-

tion 4.2 Time Correlated Single Photon Counting (TCSPC) measurements are performed. This is with the aim to directly observe the changes in the photoluminescent lifetime data due to excitation position and surface finish. Following this in Section 4.3 using a reflection goniophotometer the transmission and reflection scattering profiles of LYSO and PTFE are observed. This is done to observe deviations, if any, from the idealised specular or Lambertian behaviour assumed for materials used in scintillator detectors.

4.1.1 TCSPC Outline

In this chapter we present three sets of TCSPC results. These will focus on different optical phenomena with an aim to understand light propagation within the scintillator crystal more thoroughly. These three experiments are

1. Time Resolved Emission Spectrum (TRES) — The lifetime data of a $2 \times 2 \times 30$ mm^3 LYSO scintillator crystal is measured at discrete wavelengths. This is done to determine if there is any change in the lifetime data with wavelength. Any such variation would introduce an additional complexity to be accounted for. Despite minimal variation in the refractive index with wavelength for LYSO [45], it is possible there could be a change in the rise or decay components with wavelength.

2. Polished and unpolished comparison — The lifetime data of two $2 \times 2 \times 20$ mm^3 LYSO scintillator crystals are measured. Both crystals are identical bar one lateral face. One of the scintillator crystal has a polished lateral face, the other a roughened (or depolished). Depolishing a side face is a common technique to increase light output [16]. This is done to improve the timing and energy performance. In this measurement we are interested to observe this effect directly as well any change to the light distribution. In Section 4.3.2 the reflection from the lateral face is observed.

3. Near and far excitation comparison — A larger LYSO crystal, $10 \times 10 \times 2$ mm^3 is excited at two different locations and the lifetime data measured. This measurement allows the additional optical transit through the scintillator crystal to be observed. The change in the light output, along with any change in the light distribution, should be visible. This measurement is analogous to a near zero and a maximum DOI measurement.

In Section 4.2 the general method will be outlined along with any considerations relevant to the three experiments described above. After this each of the experiments will be described in further detail and their results presented. The discussion of these results will be left until Section 4.4.1 at the end of the chapter after the reflection goniophotometer results are presented.

4.1.2 Reflection Goniophotometer Outline

In this chapter we will look at the reflection profiles of two materials — LYSO and PTFE. These two experiments are

1. Comparison of polished and roughened (depolished) LYSO lateral faces. In this measurement we will measure the reflection profile from two identical LSO scintillator crystals with one difference — the lateral face. The aim is to observe the deviation for purely specular behaviour in the depolished case. Furthermore we wish to see how close to idealised specular, or indeed Lobe reflection, the 'polished' case is. This is a similar measurement to that presented in [54] for reflection profiles of BGO. In that a polished surface was seen to have a spread of 1.3°.

2. Off-axis measurements of Teflon tape (PTFE). In this measurement we will measure the reflection profile of PTFE with various polar angles of incident white light. We wish to determine if PTFE can be approximated as an idealised Lambertian emitter. If not, the size of the deviation will give some indication of the material's behaviour. In later chapters, this result may prove useful in determining deviations between predicted and experimental results.

In Section 4.3 a description of how the reflection goniophotometer operates will be presented. Following this, the two experiments described above will presented. The discussion of these results will be left until Section 4.4.2.

4.2 Time Correlated Single Photon Counting Measurements

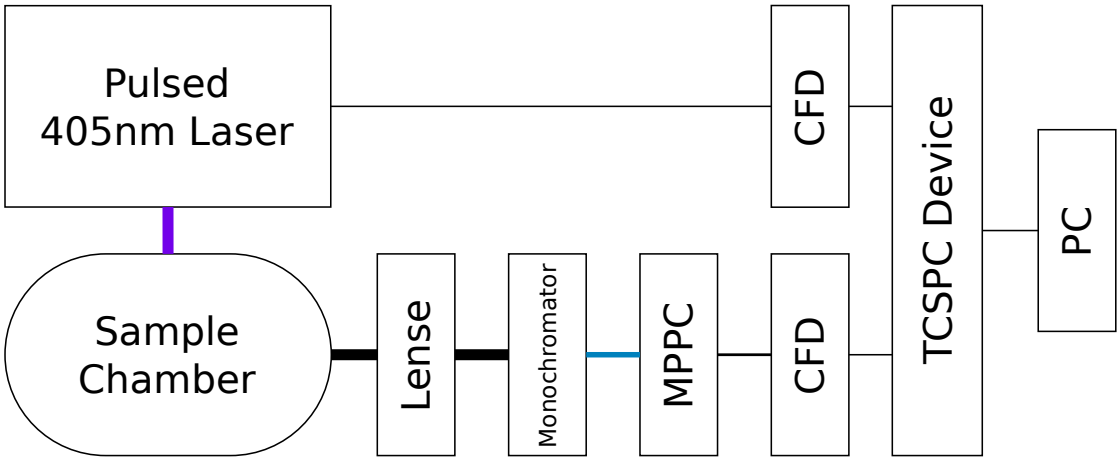

Figure 4.1: A schematic of the time-correlated single photon counting (TCSPC) apparatus with key components labelled is shown. Essentially the relative delays between laser pulses and the resulting interactions in the sample chamber are histogrammed.

TCSPC, can be used to record fast optical phenomena such as photoluminescence [56]. In a process similar to the delayed coincidence method [57], the time delay between a regular first signal and a weaker second is used to build up a histogram of relative arrival times. In figure 4.1 a schematic of the TCSPC apparatus is outlined. The first signal in this work is from an ultra-short pulsed laser with a wavelength of 405 nm produces pulses with a typical width of 60 ps and a period of 50 ns [58]. The laser in this case triggers the first discriminator electronically saving the need for additional optics and photodetector. The second signal is formed by detection of individual photons produced by the laser pulse interaction within the sample chamber. The second detector, an MPPC, is shielded by a monochromator to allow selection of specific interactions of interest to be studied. In this work photoluminescence is studied by choosing a wavelength sufficiently longer than the incident of 405 nm. The limit in the precision of time measurements in TCSPC is not constrained by the time resolution of 'start detector' and therefore is significantly lower [59]. In [59] a thorough description of TCSPC and the method used can be found.

4.2.1 Instrument Response Function

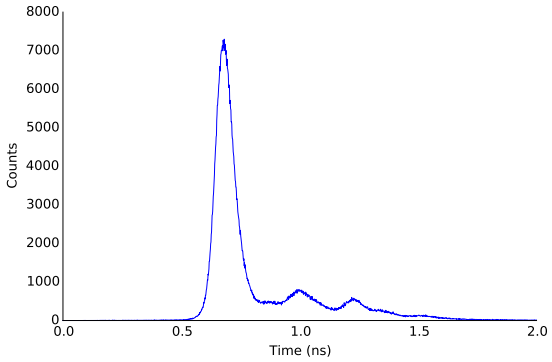

Figure 4.2: A typical instrument response function (IRF) from the TCSPC apparatus.

In figure 4.2 the lifetime data measured for the TCSPC with no sample present within the chamber is shown. This is known as the Instrument Response Function (IRF). The Full Width Half Maximum (FWHM) of the first peak in this figure is approximately 100 ps. This encompasses the time spread due to the finite width of the laser pulse, variance in travel time through the sample chamber and transit time spread (or equivalent) in the photodetector. Once normalised, the IRF can be considered a probability distribution of the arrival time of a random laser photon. Therefore once a sample is placed within the chamber, the resulting lifetime data measured will be a convolution of its own photoluminescence and the IRF. For a known IRF the photoluminescent distribution can be recovered using reconvolution analysis [56, 59, 60]. we use the proprietary tool known as FAST [61] where appropriate to accomplish this.

It should be noted that the TCSPC used is highly sensitive to reflecting surfaces within the sample chamber. In figure 4.2 secondary, smaller, peaks due to these reflections can been seen. Due to the convolution mentioned above, these multiple peaks lead to distortions in the lifetime data measured. This can make it difficult to isolate smaller components of the lifetime data reliably. In all the following measurements these secondary peaks have been verified as minimal by ensuring careful placement of holders, samples and filters within the chamber. In the following section measures to ensure this are discussed.

4.2.2 Sample Absorption Length Considerations

As discussed in Section 2.2, LYSO is mostly transparent to optical photons (which it can generate by radioluminescence). LYSO does begin to absorb light in the UV significantly, however at 405 nm the absorptivity is still low. Combined with the multiple reflections within the chamber and the beam spread of the laser, it becomes difficult to isolate phenomena other than the weak photoluminescence.

We endeavour to counter this issue effect in three ways. Namely:

1. Measurements are made through large thicknesses of LYSO. At least 10 mm of material must be present.

2. Samples within the chamber are aligned with the incoming light source to prevent short path returns. This increases the time delay of individual photons to returning to the sample as well as spreading the intensity of the secondary peaks out over time.

3. The focal point of the collecting lens is set to maximise the light collection from the primary excitation position. In combination with the placement of the sample we can maximise the useful signal when we intentionally move the sample.

Once these initial steps are completed, we compare the IRF to that with the sample in place. If the amplitude of secondary peaks (due to reflection) are low, the measurements can proceed.

Prior to all measurements the scintillator crystals are cleaned using isopropyl alcohol. No wrapping materials are used in these TCSPC measurements due to no effective manner of excitation through the material for the orientations explored in this chapter.

4.2.3 Time Resolved Emission Spectrum Measurement

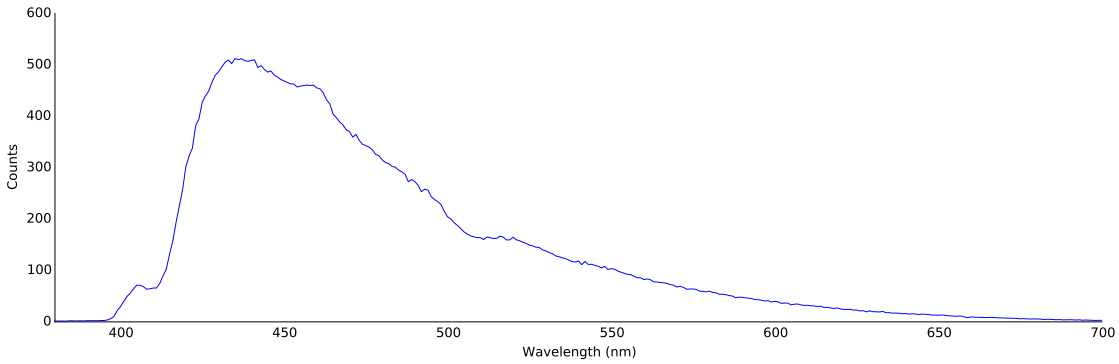

Figure 4.3: The LYSO photoluminescent emission spectrum for 405 nm laser excitation. The distribution has been corrected for the photodetector sensitivity.

In figure 4.3 the emission spectrum for a LYSO $2 \times 2 \times 30\text{mm}^3$ scintillator crystal is shown. This distribution matches that found for x-ray spectra [62, Fig 3.] for LSO. The peak of the distribution is at 435 nm, and despite the presence of a filter a secondary peak due to the laser is visible at 405 nm. Fitting a Gaussian to the peak of the distribution we find a location and scale parameter of 465.6 ± 1.0 nm and 28.4 ± 0.4 nm respectively. Whilst the distribution is clearly not Gaussian, a Gaussian does cover the bulk of the radiation emitted by LYSO. To determine the effect, if any, of the emission wavelength on the lifetime data, the following is performed. In figure 4.4 the TRES for LYSO is plotted from 410 nm to 600 nm for 10 nm increments.

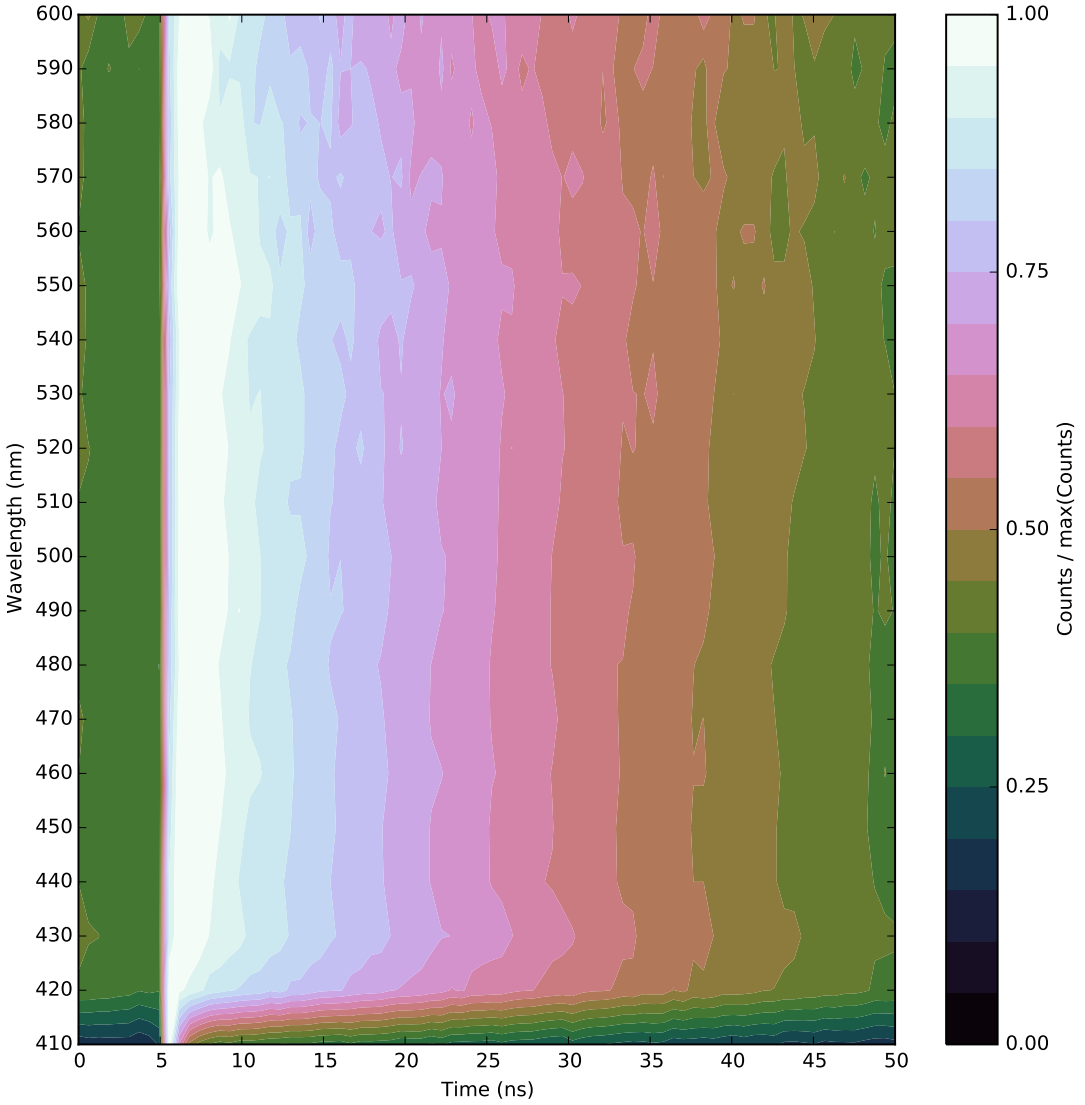

Figure 4.4: The photoluminescent lifetime data of LYSO with wavelength (TRES) for an excitation wavelength of 405 nm. Intensity is normalised to each wavelength's peak value to allow comparison of decay visually.

The lower limit was chosen to overlap with the laser to observe its effect upon the measurement. The upper limit was the highest wavelength a reasonable response could be gained from the scintillator crystal in reasonable time. Outside of the region affected by the laser, there is no discernible change of the lifetime data shape with wavelength. Combined with the size of the

scintillator crystals and the wavelength dependence of the refractive index [45] this result was not unexpected. The predominant decay component beyond 430 nm fell, within error, within the 43 ns [63] found via radiation measurements [63]. Due to this, in the remainder of the thesis we will not consider wavelength-dependent behaviour within simulations of the scintillator crystal.

4.2.4 Polished vs. Depolished Measurement

In our second measurement we compare two LYSO scintillator crystals of identical size but different surface finish. For one of the $2\times2\times10$ mm^3 crystals, one of the 2×10 mm^2 faces has been roughened. This is typically done to maximise the light output as it has been shown to not affect the time resolution subsequently measured [64]. We wish to determine if any difference in the resulting TCSPC lifetime data can be observed.

The method to accomplish this is similar to the previous section. In this, the scintillator crystals are laid flat on a black metallic surface with the lateral face of interest facing up. The scintillator crystals are oriented in line with the incident laser light. No wrapping is used, therefore light can escape from the total volume of the scintillator crystal. In this, and the next measurement, the lifetime data is recorded at 460 nm for 30 minutes per measurement, unless otherwise stated. In figure 4.5 the lifetime data of the two scintillator crystals are shown.

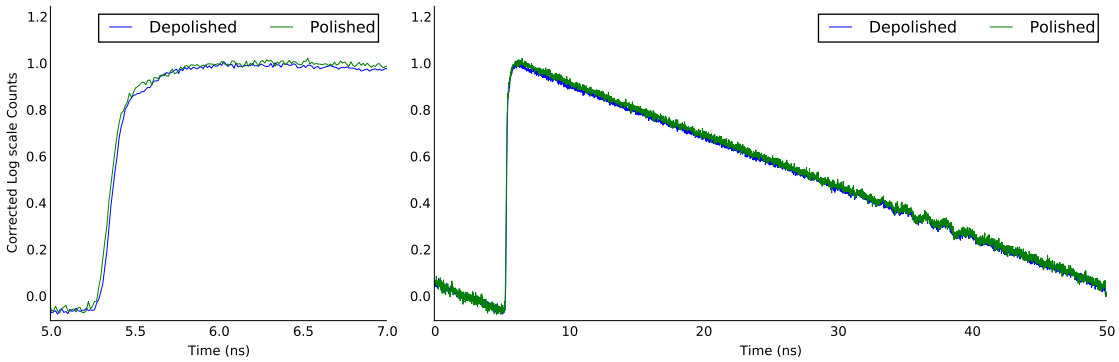

Figure 4.5: Comparison of LYSO decay spectrum with different surface finishes. These are identical LSO scintillator crystals with a single lateral face different. One has a depolished (roughened) lateral face, the other remains polished. No difference in lifetime data is visible.

In the above figure no discernible difference between the two decay spectra is visible. The

depolished scintillator crystal has a decay component of 49.0 ± 1.1 ns. The polished scintillator crystal has a decay component of 47.0 ± 3.6 ns. These agree well within experimental error. Given that light is able to escape through the whole scintillator crystal almost immediately, no difference between the two cases is expected. Ideally a measurement would look at excitation in a specific volume of the scintillator crystal and extract photons from another. This would be a fairer comparison with the radiation measurements performed in the previous chapter. However this would require that secondary peaks, as discussed in Section 4.2.2, be reduced. Furthermore this measurement does not account for any coupling effects between PTFE and the surface. However this measurement does give one interesting result. In figure 4.6 the counts per minute is shown.

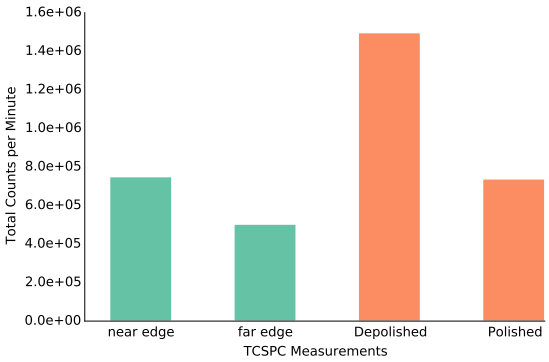

Figure 4.6: The total counts recorded for the polished/depolished and the near/far edge measurements are presented. Note that the counts per minute can be only be fairly compared in each experiment, not to one another.

In this we can clearly see that the depolished case receives double the counts per minute of the polished case. Due to the whole scintillator crystal being excited without wrapping, this is likely due to the increased light coupling out of the depolished face.

4.2.5 Near Edge versus Far Edge Measurement

Next we wish to observe a clear change in the lifetime data. If light transport does alter the lifetime data produced then alteration of the excitation position within the scintillator crystal should accomplish a visible change. Toward this end we excite a larger LSO scintillator crystal, $10 \times 10 \times 2$ mm^3 at two positions shown below in figure 4.7.

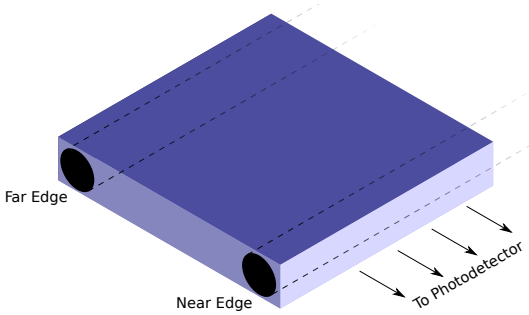

Figure 4.7: A $10 \times 10 \times 2$ mm^3 LYSO scintillator crystal is laid flat and excited at two different positions. These are labelled as near and far with respect to the photodetector.

In the above figure it seen that the larger scintillator crystal is laid flat and excited at two positions which we will refer to as near and far. This is due to their relative distance to the photodetector. In the far position, any photons generated by interaction with the incident light must travel through the scintillator crystal to reach the photodetector. This is opposed to the near case, where half of the generated photons may escape immediately. Despite the difference in geometry, to ensure a good sized absorption region, this measurement can be considered analogous to the DOI measurements in the previous chapter.

In figure 4.1 an adjustable lens is shown connected to the sample chamber. In this measurement the lens is focussed on the near end of the scintillator crystal for both measurements. This ensures that light is collected predominantly from this position — thus ensuring in the far edge case the majority of light collected must travel through the scintillator crystal. As in the previous measurement, the monochromator is set to 460 nm and each measurement is taken for 30 minutes. In figure 4.8 the lifetime data of the two excitation positions are shown.

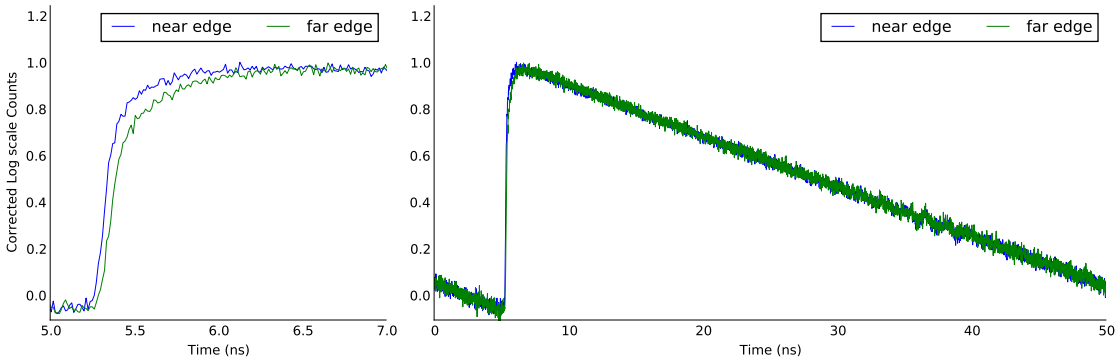

Figure 4.8: Comparison of LYSO decay spectrum with different excitation position. In this case a single unwrapped LSO scintillator crystal is excited at two different positions.

In the above figure it can be seen that the decay component is the same in both decays however there is a clear difference in the rising edge. This alteration is attributed to the increased travel time through the scintillator crystal. The slope of the rising edge is seen to be approximately the same. This would indicate there is limited increase variance introduced by light transport in the unwrapped case shown. In figure 4.6 it can be seen that there is a drop of a third in count rate between the near and far edge cases. This would attributed to light escaping through the scintillator crystal lateral faces and not reaching the photodetector.

4.3 Reflection Goniophotometer Measurements

A goniophotometer[1] is a device for exploring the transmission and reflection profile of a material's surface [65]. In [66] a similar device was used to measure the reflection properties of a common previous generated scintillator crystal, Bismuth Germanate (BGO). These results were then used in [54] to simulate custom reflection surfaces in a Monte-Carlo simulation (GEANT4 [67]) directly. In this work we utilise a more advanced goniophotometer to explore the properties of LYSO. In doing so we wish to determine deviations, if any, from the simplified reflection behaviours typically assumed in Monte-Carlo simulations. This will give us more information to determine the effect reflections at the faces of the scintillator crystal and the diffusive wrapping have upon the performance of the scintillator detector.

[1] Gonio from the Greek 'gōnia', means angle and photometer is a device for measuring intensity of light.

A typical goniophotometer is comprised of a light source and detector; Both parts on stages capable of moving about the sample. To record a Bi-directional reflectance distribution function (BRDF), for a given incident direction, many measurements are required uniformly on a unit hemisphere about the sample. A high resolution BRDF will require hundreds, if not thousands, of individual measurements. Due to this, a study into how incident wavelength or direction affects a BRDF can be extremely time consuming. In this work we utilise a reflection goniophotometer, which we will refer to as an imaging sphere.

4.3.1 The Imaging Sphere

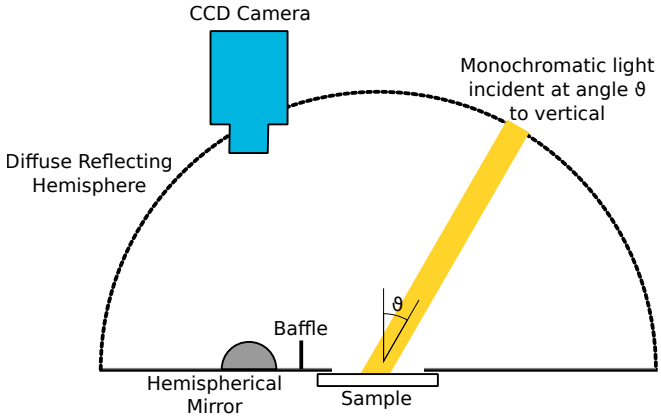

Figure 4.9: An idealised schematic showing the key components of the reflection goniophotometer.

In figure 4.9 a schematic of the imaging sphere is shown. Collimated light is shone onto the sample at an angle with respect to the surface. This light source can be chosen to be monochromatic or a white light source. In both cases, the source in this work is incoherent. Incident light scatters off the sample onto the weakly reflecting diffusive hemisphere. The hemisphere is diffusive to ensure scattered light from the hemisphere does not produce strong secondary specular reflections. Furthermore the hemisphere's surface is weakly reflecting to ensure secondary reflections die away quickly[2]. A high resolution (1024×1024 pixels) CCD images a hemispherical mirror places directly below the CCD. The mirror is designed to observe the see the entirety of the hemisphere — Thus

[2]The proportion of light from a secondary reflection reaching the CCD can be given by R^2. Therefore the lower the value of the reflectance R, the lowest the portion from secondary reflections.

allowing the CCD to image the light reflected from the sample. After post-processing to correct for aberrations and differences in light intensity due to the geometry of the imaging sphere, an image of the light intensity per solid angle is created. The calibrated version of this image is referred to as the BRDF. The sum of the BRDF will result in the reflectance of the sample. A much more detailed description of the instrument can be found in [68]. A full description of the methodology used with the imaging sphere is given in Appendix B.1.

As mentioned earlier in this chapter, we will look at the reflection profile of two materials — LYSO and PTFE.

4.3.2 A comparison of rough and polished LYSO surface profiles

We will compare the reflectance of the roughened surface to the polished one for chosen ranges of incident wavelength and incident angle. The aim is to observe the deviation from ideal specular in the polished case and the deviation from the polished case for the depolished case. In figure 4.3 it is seen that the bulk of optical photons produced by LYSO are within the range of 400 nm to 600 nm. As the refractive index of LYSO is 1.8 [45], the critical angle with air is approximately 34°. Therefore the range of interest for our measurements is defined by these wavelengths and the range between 0 and this critical angle.

To begin we use a selection of these ranges to look at the difference in reflectance between the polished and depolished cases. In figure 4.10 a bar chart of these results is shown.

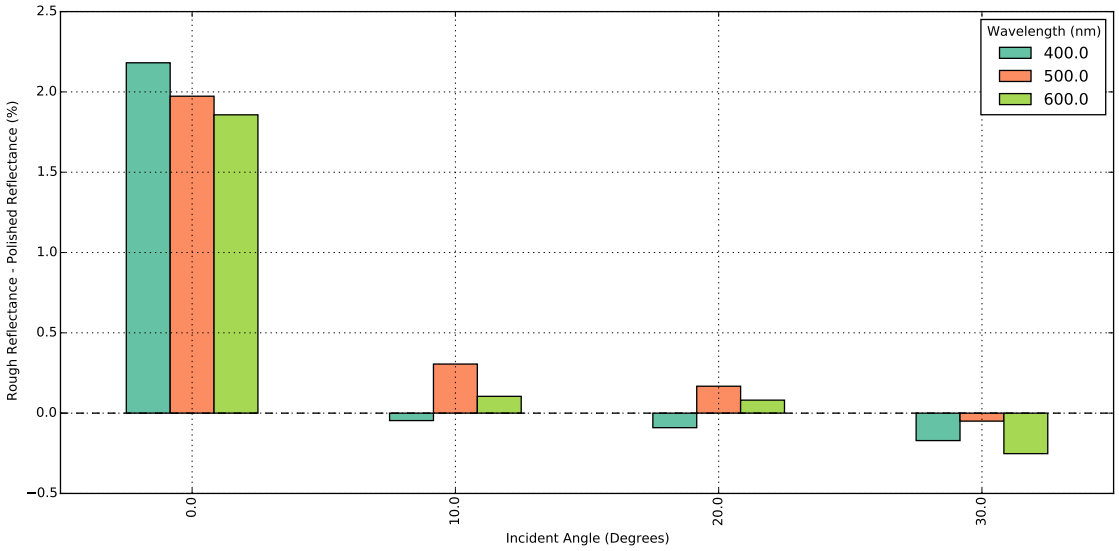

Figure 4.10: Difference in reflectance measurements from the Imaging sphere between polished and roughened surfaces of LYSO.

Intriguingly the roughened surface shows a higher reflectance, but only for normal incidence. One potential reason for this difference can be seen by looking at two BRDFs of normal incidence. The polished and depolished BRDFs are shown in in figures 4.11 and 4.12 respectively.

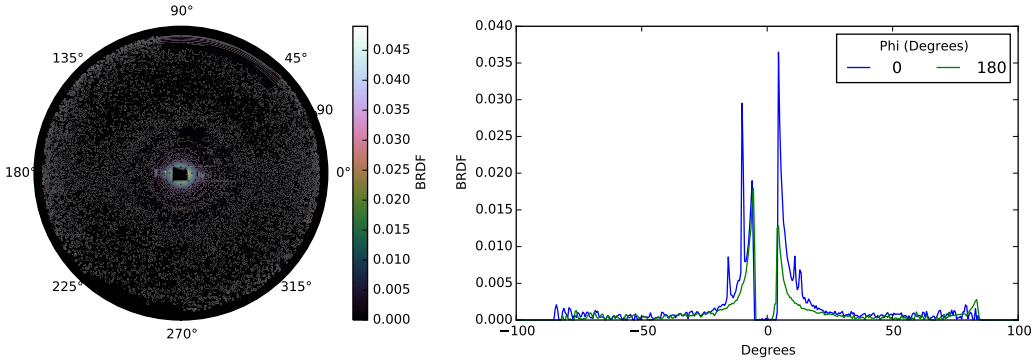

Figure 4.11: A polar plot along with horizontal and vertical slices of the BRDF of a polished LYSO 10×2 mm^2 face.

In these figures the spread about the (missing) specular peak can be seen. The specular peak is occluded due to a series of small square apertures are present along the hemisphere's surface.

One (or more) apertures can be opened to allow light to be shone onto the sample from within the Imaging sphere. Any light reflected onto an opened aperture will clipped from the resulting BRDF. This is advantage as the dynamic range of the CCD can be assigned to the edge. This allows us to explore the non-specular portion of the reflected light much more effectively. Critically the non-normal measurements do not exclude the specular peak. Therefore the (lack of) difference between polished and depolished reflectances could be attributed to the apparatus.

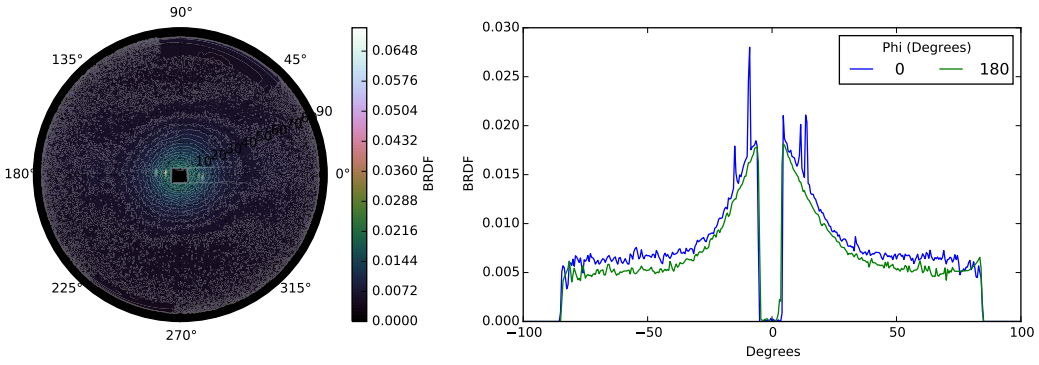

Figure 4.12: A polar plot along with horizontal and vertical slices of the BRDF of a roughened LYSO 10×2 mm^2 face.

There are two differences visible between the polished and roughened surfaces. Firstly in the roughened surface, about 1% of light is scattered uniformly into random directions. Secondly the width of the specular peak can be seen to be wider in the roughened case than the polished case. Both effects contribute 2% more reflected light in the depolished case than the polished case. To quantify these effects more clearly we fit Gaussian distributions to the peaks visible in the non-normal cases. In table 4.1 the results of these with wavelength and incident angle, along with their reflectance can be seen for both samples.

Table 4.1: Reflectance values for varying incident wavelength and incident angle for polished and roughened LYSO surfaces.

Wavelength (nm)	Angle (Degrees)	Rough (%)	Polish (%)	Rough Std (Degrees)	Polish Std (Degrees)	Rough Amplitude	Polish Amplitude
400	0	2.6	0.4	/	/	/	/
400	10	3.2	3.2	0.83	0.67	0.02	0.25
400	20	4.4	4.5	0.75	0.68	0.08	0.22
400	30	5.9	6.1	0.81	0.75	0.17	0.22
500	0	2.2	0.2	/	/	/	/
500	10	2.9	2.6	0.77	0.59	0.02	0.25
500	20	4.4	4.2	0.74	0.67	0.10	0.22
500	30	5.9	5.9	0.86	0.78	0.20	0.24
600	0	2.1	0.2	/	/	/	/
600	10	2.6	2.5	0.78	0.58	0.03	0.25
600	20	4.2	4.1	0.69	0.62	0.11	0.23
600	30	5.6	5.8	0.79	0.70	0.20	0.24

In the table it can be seen that the standard deviation of the Gaussian fits of the roughened surfaces are consistently higher than those for the polished cases. Values determined for normal incidence using a profilometer are given in [54, Figure 5]. These give values for a specular peak standard deviation of 0.31° for a polished surface, a value of 4.76° for an etched surface and 2.03° for a ground surface. By comparison we would see that the polished values are in good agreement.

In the same table we can see the amplitude of the specular reflection peaks. It can be seen that the amplitude of the roughened surface increases at higher angle. By comparison the amplitude of the specular peak for the polished case is essentially constant. Given that both roughened and polished show increasing reflectance with incident angle, as we would expect due to Fresnel reflection, this effect is most likely due to a greater proportion of light in the roughened cases reflecting specularly rather than diffusively. This would indicate that the effect of the roughened surface is most pronounced at low incident angles. Given the large difference in reflectance seen between the two cases at normal incidence, this conclusion would be in agreement.

4.3.3 Measurements of PTFE

In the previous chapter the 'wrapped' configuration used Teflon tape (PTFE) to wrap the scintillator crystals to improve light output at the photodetector. The reflection profile of PTFE is generally taken as a Lambertian reflector with an imperfect reflectance and no incident angle de-

pendency [66]. In this section we look at the reflection and transmission properties of PTFE to determine the size, if any, of deviation from this behaviour.

As we are primarily interested in the angular behaviour with PTFE we will use a white light source. This will produce clearer images and allow quicker scan times. For comparative purposes the reflection and transmission profiles for PTFE at normal incidence and at 20 degrees to the normal are measured. The results for these measurements are given in figures 4.13 and 4.14. The cross sections have been normalised to their maximum amplitude to allow easy comparison of the reflection and transmission.

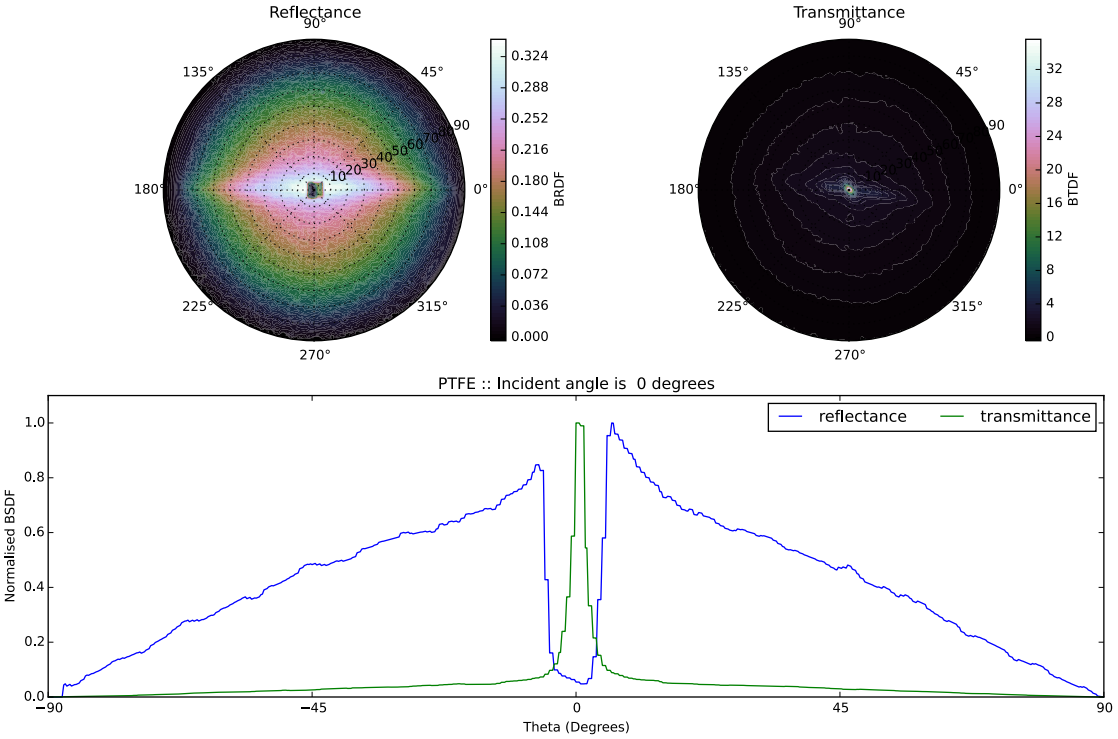

Figure 4.13: Reflectance and Transmittance plots of PTFE at normal incidence. Normalised (vertical) cross section of both reflectance and transmittance shown below for comparison.

In the above figure, the expected cosine behaviour of a Lambertian reflector is seen. Above the normal (Theta close to zero) the square aperture open for the incident source is visible in the reflected case. About this, a specular reflection is visible in the reflection image. Below in figure 4.14 a smaller, specular peak is visible. This would indicate that specular reflection from

PTFE does occur, but it is a much smaller effect than the Lambertian. For the transmittance plots, the specular peak is much more pronounced. This implies a large portion of the incident light is transmitted through the PTFE. The PTFE measurements presented in this section look at a single layer of PTFE. In reality, scintillator crystals are bound with many layers to produce a high reflectivity [69]. Also in this transmitted case, some diffusive behaviour does occur. This would indicate a small portion of light is scattered into high polar angles with respect to the surface. At the next PTFE layer it is unknown whether light would be specularly reflected, essentially trapped in the PTFE layers, or scattered back into the scintillator crystal. A future measurement should look at such high incident angles to determine this effect more fully. In figure 4.14 the reflectance and transmittance for white light incident at 20° to the surface normal is shown.

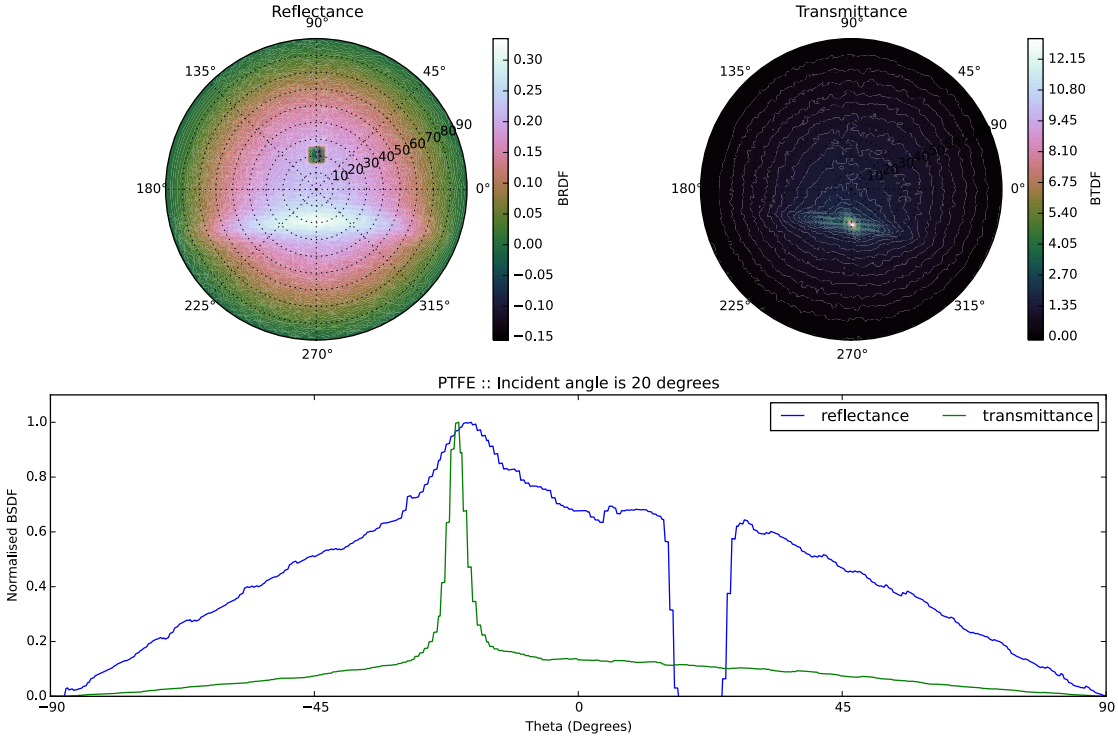

Figure 4.14: Reflectance and Transmittance plots of PTFE at 20° to normal incidence. Normalised (vertical) cross section of both reflectance and transmittance shown below for comparison.

In the above figure several interesting things are to be noted. Firstly a specular lobe, is as expected visible at 20°. In the reflectance cross section it can be seen however most light is

scattered as a Lambertian emitter. In the transmittance cross section the specular peak is lower, wider and again in the expected position. In this case a greater proportion of light is scattered diffusively compared to the normal incidence case. This implies a greater portion of the incident light is interacting with the PTFE before being emitted diffusively.

In both the normal and 20° incidence a bar is visible in both transmittance and reflectance values. This bar is not an artefact of the light source, implying the material itself is causing this behaviour. As the PTFE is stretched across the aperture this could be so. A future measurement should look at replicating this result and rotating the sample to arbitrary angles to determine if this is the case. We would conclude that PTFE can be approximated as a Lambertian reflector with the provision that Fresnel reflection is taken into account.

4.4 Discussion

4.4.1 Implications of TCSPC Results

In these measurements the lifetime data of optical excitation of LSO were presented. Three experiments were performed. In the first, TRES measurements on LYSO show no discernible change in the lifetime data with wavelength within experimental error. From this result it is concluded that any variation with wavelength is negligible in this work. In the next measurement we looked at the effect of polished and unpolished scintillator crystals. In these, a single lateral face was altered. The rate of light escaping was seen to double in these measurements when a single lateral face is depolished. This is consistent with [16]. No change in the lifetime data was visible. This could be due to the whole scintillator crystal being excited. In an actual γ interaction a single source of photons would be generated which would travel through the scintillator crystal. In this case, any photoluminescent light can escape quickly. A future measurement should look at a larger scintillator crystal. This would overcome the limit imposed by TCSPC due to secondary reflections to determine if this is the case. The third measurement looks at the introduced effect due to different excitations positions within the scintillator crystal upon the lifetime data. In this a minor alteration to the rising edge of the data was seen. Furthermore a drop of a third in the light output between the near and far edges was seen. A future measurement should look at including PTFE

wrapping around the bulk of the scintillator crystal. It would be interesting to see if the wrapping introduces an additional change to the rising edge. In this case we would predict a shallower rising edge and a smaller difference in the light output between the near and far cases.

As a whole the TCSPC measurements have shown light transport in the unwrapped cases is a small effect upon the decay spectrum seen. Further measurements would be needed to determine if the difference in light output between the near/far and polished/depolished cases carried over when wrapping is used.

4.4.2 Implications of Imaging Sphere Results

Measurements of the reflectance properties of two materials have been shown in this chapter. It was seen that the depolishing of a lateral face of LYSO leads to scattering into high polar angles. This results in increased reflectance compared to the polished case. Gaussian fits to the specular lobes for varying wavelength and incident direction show several things. Firstly that the depolished cases consistently show wider specular peaks. Secondly there is no shape variation with wavelength however there is a shift in the total reflectance. Given the minor variation with wavelength in the reflectance we would conclude the shape and reflectance are not significantly affected by it. Thirdly our results indicate that with increasing incident angle the proportion of light scattering specularly is seen to increase compared to the diffusive component. Given the usage of surface roughening to increase light output in scintillator detectors, this result would imply the increase is due to light trapping at these lateral faces.

The PTFE results show the predominantly Lambertian behaviour expected for both normal and non-normal incidence. However there is a visible bar which we attribute to the material. To confirm this, further measurements should be performed.

4.4.3 Implications of Experimental Results on Scintillator Detector Performance

Results presented in the previous chapter demonstrate several behaviours a theoretical description must be able to account for. Firstly there is no relationship, within experimental error, between the interaction position within the scintillator crystal and the timing performance. Any model of the

time resolution must show none or limited variation with depth of interaction. Secondly the time resolution has been shown to degrade with increasing scintillator crystal length. Furthermore the potential model must explain by poor quality wrapping is seen to degrade the timing performance. Finally, as shown in Appendix A.2, the light output must be seen to increase by a factor of at least two when wrapping is used.

The optical results presented in this chapter add additional constraints. Firstly the lifetime data from the scintillator crystal should show no dependence, within experimental error, upon the wavelength of the photon generated. Secondly roughening a single (lateral) face of a scintillator crystal should increase, ideally double, the light output observed compared to a purely specular case. Thirdly the interaction position within the scintillator crystal should alter the lifetime data and produce a small drop in the light output when travelling through a large bulk of scintillator crystal. Finally a depolished scintillator crystal should increase the number of photons scattered into random directions. This effect should be most pronounced near normal incidence.

In the next chapter these conditions will be used to validate a maximum likelihood based model of the timing performance of scintillator detectors.

Chapter 5

Validation and Model

5.1 Introduction

The work presented thus far in this thesis has looked at experiments exploring light-related effects which may or may not alter the timing and energy performance of scintillator detectors. The results of this work were summarised in Section 4.4.3. In this chapter a theoretical description of light propagation within the scintillator crystal and the resulting effect upon the scintillator detector performance will be presented.

'Light transport' describes the propagation of light from its creation at the radiation interaction point, to its subsequent arrival at the photodetector. More precisely the light transport is defined as the variance in the travel time to the photodetector of optical photons from their creation. Modelling how optical photons created from a single interaction travel through the scintillator crystal be used to calculate the light transport contribution to the PDF. This modelling is done in two ways. Firstly an analytical expression is derived from the Poynting vector and applied to two infinite faces separated by a distance L. Secondly the analytical model is used to validate a Monte-Carlo simulation. This simulation of the light transport allows us to model more complex surface and bulk effects such as those described in previous chapters. In the next chapter more complex surface behaviours are discussed using this model.

The model presented in this chapter is an expansion of the Cramer Rao Lower Bound (CRLB)

method presented in [63]. Before describing this model a brief review of prior methods used to predict timing performance are discussed in Section 5.2. Following the there will be a brief introduction to the statistics used followed by a description of their application to the description of scintillator detectors. The model will then be used to predict increasingly complex representations of the scintillator detector. At each step, results collected from chapters 3 and 4 are used to determine the validity of the model.

5.2 Background

The application of likelihood statistics, and specifically Fisher Information, to scintillator detectors has several prior applications. In [70] the effect on the timing performance of gamma ray photons arriving in quick succession at a scintillator detector is calculated. It was shown that only very severe overlap of pulses need lead to severe degradation to the timing performance of scintillator detectors. This lead to the conclusion that multiple event separation and coincidence timing resolutions could be massively improved from their 1990's levels. In [71] several photodetectors are placed about a larger scintillator crystal to produce what is known as a monolithic scintillator detector. This paper presents the relationship between the localisation of the gamma ray photon conversion point in three dimensions and the spatial properties of the scintillator detector. This allows gamma ray events to be localised within the monolithic scintillator detector by TOF information. There are two main result of interest in this paper. Firstly increasing the size of the scintillator crystal is shown to significantly degrade the spatial resolution. Secondly wrapping the scintillator crystal with PTFE will "yield larger and more constant signal amplitudes, which may improve the timing and the energy resolution of the detector" [71]. This work was expanded in [38] to include the effect of noise. It was stated in this paper however that a full description of the timing performance due to modern photodetectors (SiPMs) contain non-linearities such as cross-talk and saturation which have yet to be fully described. In 2012 [24] looked at the relationship between the time resolution and the various contributions from the scintillator detector. This paper describes the calculation of the Cramer Rao lower bound (CRLB) for an ordered set of events. It is shown that significantly fewer ordered events will reach the CRLB quicker than a large number of unordered events. The implication is that knowledge of arrival times of individual photons at

the scintillator detector could surpass traditional analogue time pickoff techniques. The work in this paper has been expanded further in [72,73] to include a more comprehensive description of the contribution due to the photodetector, including digital SiPM measurements indicating the light transport contribution, synonymous with the spatial confinement, could be reduced or removed by multiple photodetectors.

5.3 Likelihood Statistics

5.3.1 Maximum Likelihood Estimation

The time resolution of the scintillator detector may be estimated from a probability density function (Probability Density Function (PDF)) describing the signal generated by a given particle interaction. To understand how this is accomplished, a (brief) introduction to Likelihood statistics is given.

The likelihood function is the probability of 'guessed' parameters for observed data. Whereas the PDF is the probability of data given parameters, the likelihood function is the probability of parameters given data. It is intuitive therefore to see that the likelihood function will reach a maximum when the parameters are the most likely. We therefore define

$$L(\theta|t) = p(t|\Theta) \tag{5.1}$$

$$\lambda(t|\Theta) = \ln p(t|\Theta) \tag{5.2}$$

where L is the likelihood function, p is the probability density function, λ is the log-likelihood function, t is a given observed event and θ is the parameter under interest. For N individual events, a random sample $\vec{t} = \{t_1, t_2, \cdots, t_n\}$, with no order implied, these equations become

$$L(\Theta|\vec{t}) = \prod_{i=1}^{n} p(t_i|\Theta) \tag{5.3}$$

$$\lambda_n(\vec{t}|\Theta) = \sum_{i=1}^{n} \lambda(t_i|\Theta) \tag{5.4}$$

As the likelihood function defines the probability the estimated parameters are correct, it is natural

to maximise L to find the most likely parameters for the sample $\vec{t}$. The definition above however will generally be zero, except for exceedingly close to the correct values, due to the product of many infinitesimally small numbers. Due to this we generally maximise the log-likelihood as the resulting parameters we find will be the same, but the distribution of the log-likelihood function about the optimal parameters will be smoother. This method is known as Maximum Likelihood Estimation (MLE) [47].

The observed events are the arrival times of individual photons produced by a particle interaction with the scintillator detector. The parameter of interest for the timing performance of a scintillator detector is the absolute time of arrival of the particle interaction. The standard deviation of the uncertainty of this parameter is the time resolution.

5.3.2 Fisher Information

The lowest potential uncertainty, for a known PDF and known number of samples, may be estimated using what is known as the Fisher Information. We define this as

$$I(\Theta) = \mathrm{E}[\Big(\frac{\partial\lambda}{\partial\Theta}\Big)^2] = \int_{t=-\infty}^{\infty} \Big(\frac{\partial\lambda}{\partial\Theta}\Big)^2 p(t|\Theta)dt. \tag{5.5}$$

Using the above equations it can be shown that

$$I_n(\Theta) = nI(\Theta) \tag{5.6}$$

The CRLB can be stated as

$$\boxed{\sigma(\Theta) \geq \sqrt{\Big(\frac{\partial m(\Theta)}{\partial\Theta}\Big)^2 \frac{1}{nI(\Theta)}}} \tag{5.7}$$

where $m(\Theta)$ is the bias factor, $\sigma^2(\Theta)$ is the variance in a statistic T estimating the parameter Θ. For cases where T is unbiased, in this case shows no variation in performance with time of collision, $m(\Theta) = \Theta$. The full derivation of equation 5.7 is given in appendix C.1. The square root of which is the standard deviation of the uncertainty in T; better known as the Cramer-Rao Lower Bound (CRLB). In this work we assume an unbiased estimator of the time resolution exists, therefore the

bias factor m is equal to Θ. As the time resolution of a scintillator detector is typically given in terms of the Coincidence Time Resolution (CTR), we can define the CRLB CTR as

$$\mathrm{CTR}_{\mathrm{CRLB}} = \frac{4\sqrt{\ln 2}}{\sqrt{nI(\Theta)}} \tag{5.8}$$

Essentially if we know the number of random samples we have and we know the PDF, we can calculate the Fisher Information and what is known as the Cramer-Rao lower bound (CRLB) of the parameter. As this gives a method independent way of determining the uncertainty in a parameter this is a powerful technique for determining the relative contribution of terms to N and the PDF.

In this section we will present contributions to the CRLB, beginning with the intrinsic; namely that relating to the scintillator crystal material properties. Following this we will present the inclusion of the photodetector. Both have been presented previously in [24], however in this work we present additional detail relating to calculating using discrete convolution. This method whilst slower than an analytical solution does offer a more generalised approach, allowing more complex contributions to the CRLB to be studied. The first of these, in section 5.5, relates to the skew of the photodetector contribution to the CRLB. Following this, in section 5.6, we present light transport and how it contributes also.

5.4 The intrinsic CRLB - The Scintillation Mechanism

As discussed in section 2.2.2, an ionising particle incident upon a scintillator crystal will create a cascade of electron-hole pairs. The recombination process in LYSO of these electron-hole pairs is given by a chain of two decay processes. These correspond to a rise and decay in a three level system, which is written as

$$N(t) = \frac{N_0}{\tau_d - \tau_r}(e^{-\frac{t}{\tau_d}} - e^{-\frac{t}{\tau_r}}) \tag{5.9}$$

where N is the number of scintillation photons at time t and τ_r, τ_d are the rise and decay constants respectively. The derivation of this form is given in appendix **??**. For LYSO these constants are 89 ± 13 ps and 43 ± 0.3 ns [24] respectively.

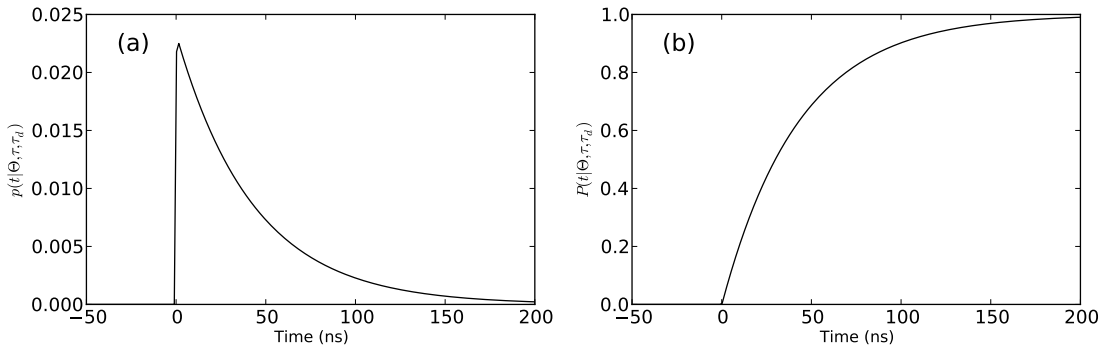

Figure 5.1: PDF (a) and CDF (b) for LYSO. A rise and decay time of 90 ps and 43 ns are used respectively [63]. A particle arrival time of zero is chosen.

Equation 5.9 can be recast as the PDF for scintillation by normalisation ($p(t) = \frac{N(t)}{N_0}$) producing

$$p_{\text{scint}}(t|\Theta, \tau_r, \tau_d) = \begin{cases} \frac{1}{\tau_d - \tau_r}\left[e^{\frac{-(t-\Theta)}{\tau_d}} - e^{\frac{-(t-\Theta)}{\tau_r}}\right] & \text{if } t \geq \Theta \\ 0 & \text{if } t < \Theta \end{cases} \tag{5.10}$$

where τ_r is the rise time, τ_d is the decay time and Θ is the particle conversion time within the scintillator crystal. The standard deviation in the uncertainty of Θ is the time resolution. In this work we taken both the rise and decay times as known such that

$$p_{\text{scint}}(t|\Theta, \tau_r, \tau_d) = p_{\text{scint}}(t|\Theta) \tag{5.11}$$

In figure 5.1 the PDF and CDF (cumulative density function) for LYSO are shown. Therefore from equation 5.8, assuming we know τ_r, τ_d and n we can estimate the intrinsic timing performance of a given scintillator crystal. We begin by looking at the effect of the number of samples for LYSO:Ce, shown in figure 5.2.

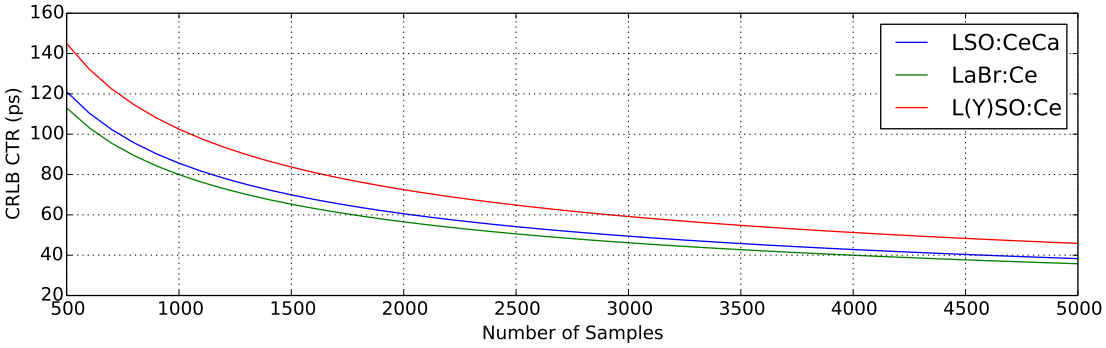

Figure 5.2: CRLB CTR for LYSO solely due to the number of independent photons detected for a given event.

It can be seen that increasing the number of samples detected reduces the time resolution seen as expected. More usefully it shows that for a SiPM with 3600 independent cells [18], a $\mathrm{CTR}_{\mathrm{CRLB}}$ of 54 ps could be achieved, assuming no other contribution. We can repeat this calculation, but this time hold n constant as 3600 and plot for varying rise and decay times. This result is shown in figure 5.3.

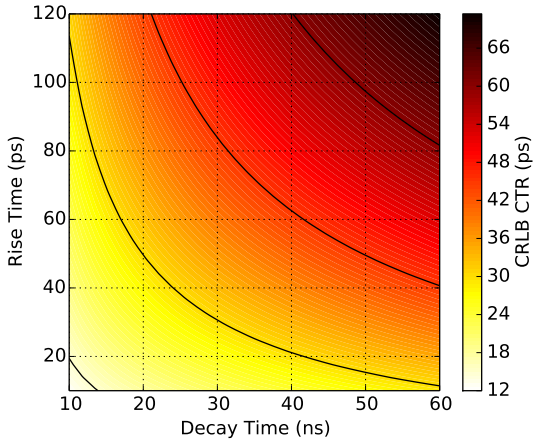

Figure 5.3: CRLB CTR for $n = 3600$ for varying rise and decay times in ps and ns respectively.

We notice that the rise time is the larger contribution to the lower bound in the time resolution than the decay time. This is consistent with prior work in several respects. Firstly small ordered sets of photon arrival times will achieve the same lower bound in the time resolution compared to large sets. As these photons will be the earliest detected, this implies the rising edge to be a

significant factor. Secondly as we shall see, additional contributions to the PDF of the scintillator detector will broaden the distribution; effectively causing a shallower rising edge to occur. Secondly from this plot we can see that the improved performance between LYSO:Ce and LYSO:CeCa is as expected [22].

5.4.1 Inclusion of the Photodetector

A given photon, successfully detected, will experience a random time delay within the photodetector. In a PMT this is due to the path length difference for amplified electrons travelling between dynodes. This effect, known as Transit Time Spread (TTS), is typically described by a clipped Gaussian [74]. As a PDF this is defined as

$$p_{\text{det}}(t|\eta,\mu) = \begin{cases} \frac{1}{\eta\sqrt{2\pi}} e^{-\frac{(t-\mu)^2}{2\eta^2}} & \text{if } (\mu - C) \leq t \leq (\mu + C) \\ 0 & \text{Otherwise} \end{cases} \tag{5.12}$$

where μ is the mean travel travel time through the photodetector, η is the standard deviation of the transit time through the photodetector (referred to as the transit time spread, TTS) and C is the clipping limit. η is also known as the Single Photon Time Resolution (SPTR). The clipping limit is typically at least 5η. The location and scale parameters of the Gaussian are typically given by manufacturer data sheets. For example for the XP2020 Q PMT these are 28 ns [17] and 273 ps [75] respectively. The TTS for the SiPM, specifically the MPPC S10931-050P, used this chapter is 70 ps unless otherwise stated[1]. To include this effect in the model of the scintillator detector, the PDF must be modified. This is accomplished by convolution, such that

$$p(t) = p_{\text{scint}} * p_{\text{det}} \tag{5.13}$$

$$\frac{dp(t)}{dt} = \frac{dp_{\text{scint}}}{dt} * p_{\text{det}} \tag{5.14}$$

Critically the above equations do not place any limit on the shape of the photodetector PDF. In the case of using a Gaussian a full analytical solution can be reached [24]. The contribution of the photodetector with respect to the SPTR is given in figure 5.4.

[1] private communication with Dr. Stefan Gundacker

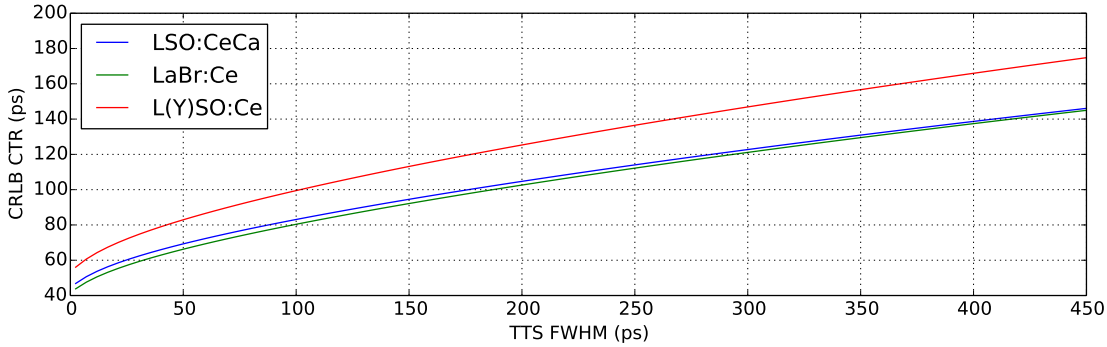

Figure 5.4: CRLB CTR for LYSO convolved with a Gaussian distribution describing the photodetector. In this case we have plotted the FWHM of the Gaussian distribution used rather than the scale parameter, μ. This is the more common experimentally measured parameter.

Firstly it's clear that as the TTS tends to zero we approach the limit of the intrinsic time resolution shown in figure 5.2. Secondly for TTS values over 100 ps, the change in the CRLB is approximately linear. A typical TTS value of 120 ps for n=3600 for LYSO results in a CTR_{CRLB} of 144 ps. Compared to the value of 54 ps observed without the photodetector, it is clear that this is a significant contribution to the time resolution.

5.5 Contribution of Skewness in the Photodetector Contribution

Previous work as looked at inclusion of the Gaussian photodetector and material properties contribution to the CRLB [24]. As a brief interlude, we will look at the contribution of a non-Gaussian TTS upon the CRLB. We will model this contribution using the skew Normal distribution [76]. The skew normal distribution is chosen for three reasons. Firstly real measurements of TTS do show skew [77, figure 2]. This figure is reproduced below in figure 5.8. In figure 4.2 the IRF is shown. This distribution will be the convolution of the laser's and the MPPC's response. In this the first peak can be seen to be negatively skewed. Secondly the difference (if any) from the regular normal distribution should be readily visible. This will also give an additional test of reliability as the two distributions should be indistinguishable for zero skew. Thirdly skewness is easily determined from the Single Electron Response, see also IRF. (IRF) of the photodetector.

By comparison with the results below, we can readily compare the CRLB observed.

The (clipped) skew Normal distribution [76] given by

$$p_{\mathrm{sn}}(t|\eta,\mu) = \begin{cases} \frac{2}{\eta} p_{\mathrm{det}}(\frac{t-\mu}{\eta})\,\mathrm{erf}(\alpha\frac{t-\mu}{\eta}) & \text{if } (\mu - C) \leq t \leq (\mu + C) \\ 0 & \text{Otherwise} \end{cases} \tag{5.15}$$

where α is a parameter related to the skewness and $\mathrm{erf}(x)$ is the error function. For various values for the skew, the log normal distribution is shown in figure 5.5.

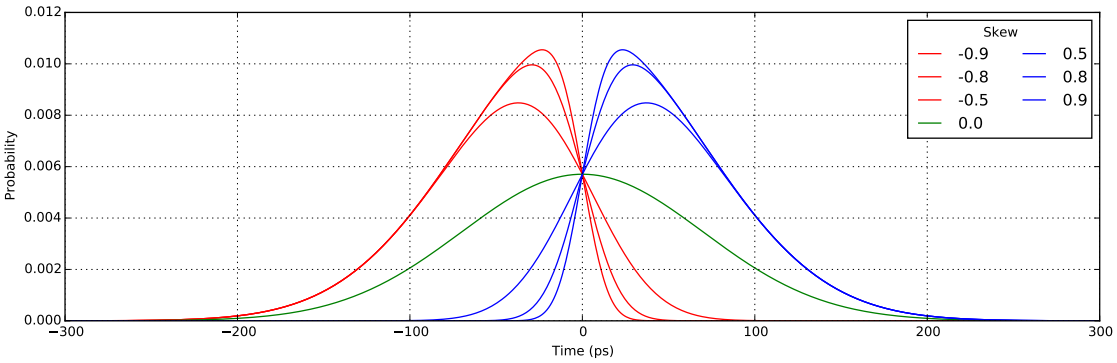

Figure 5.5: The skew normal distribution [76] shown for several values of α. Those with positive skew are shown in blue, those with negative skew in red and the Normal distribution (the case of zero skew) is shown in green.

Using an η=70 ps, we vary the α parameter and use equation 5.15 to determine the CRLB CTR as described in the previous section. Note that we plot the CRLB CTR against the FWHM of the skew normal distribution. For the normal distribution the FWHM is readily shown to be 2.355 multiplied by the scale parameter. However in the case of the skew normal distribution, it is measured directly for each combination of α and η. For positive, negative and zero skew we plot the CRLB CTR against FWHM in figure 5.6.

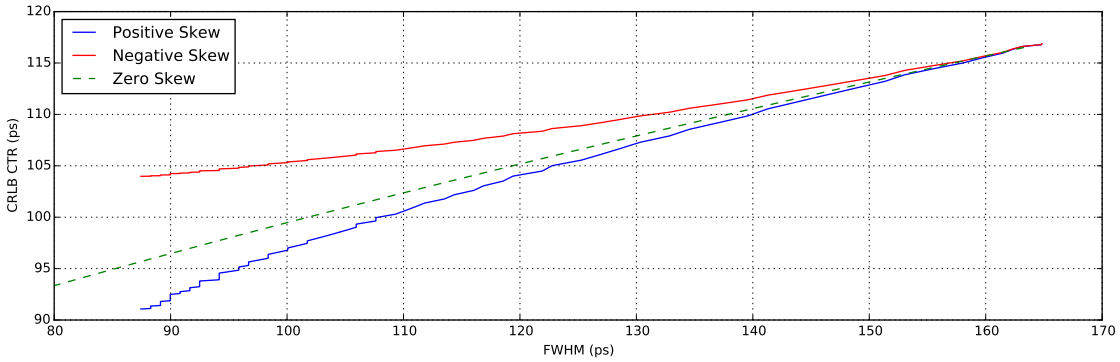

Figure 5.6: The CRLB CTR (in ps) against the FWHM (in ps) for the skew normal distribution. In blue are estimates with positive skew and in red are estimates with negative skew. The line for the Normal distribution with FWHM is also given as a green dashed line. All values meet at approximately 165 ps as expected (2.355×70 ps).

It can be seen that the photodetector distributions with positive skew possess potentially lower CRLB estimates, compared to those with negative skew where there is degradation. This effect increases with increasing skewness, reducing the FWHM of the distribution seen. In this figure we cap at a CRLB of approximately 90 ps for a skewness of ± 0.9 corresponding to positive and negative skewness respectively. Close to this value, the skew normal distribution tends to the half-normal distribution [78]. Of note from this figure it can be seen that if the skewness varies between interactions then so will the CRLB. This will be an additional contribution to the uncertainty in the CTR seen over multiple measurements. We can replot the above result in terms of the distribution's skewness rather than the FWHM as shown in figure 5.7.

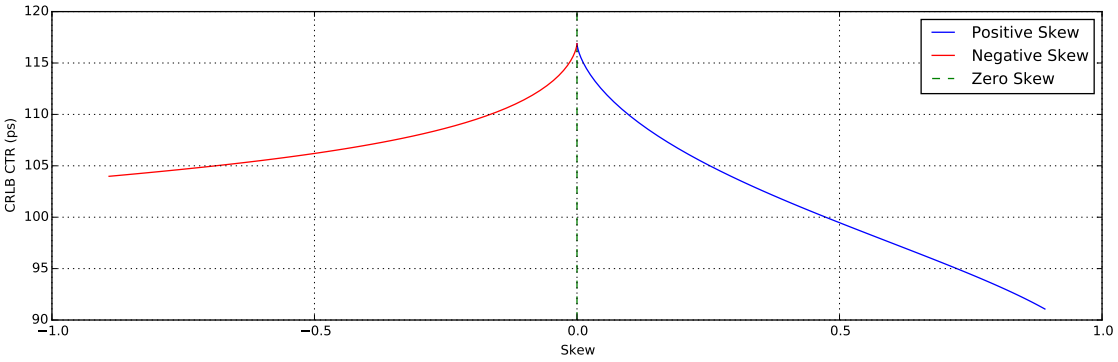

Figure 5.7: The CRLB CTR (in ps) against the FWHM (in ps) for the skew normal distribution. In blue are estimates with positive skew and in red are estimates with negative skew. The line for the Normal distribution with FWHM is also given as a green dashed line. All values meet at zero skewness as expected.

In this we can see any amount of skewness will reduce the CRLB CTR. Critically this says that how the shape of the TTS is determined for a given photodetector will matter. Simply measuring the FWHM of a photodetector's TTS and assuming a Normal distribution could lead to a significant overestimate in the CRLB CTR.

In figure 2 of [77], a typical SER is shown. This figure is reproduced below in figure 5.8.

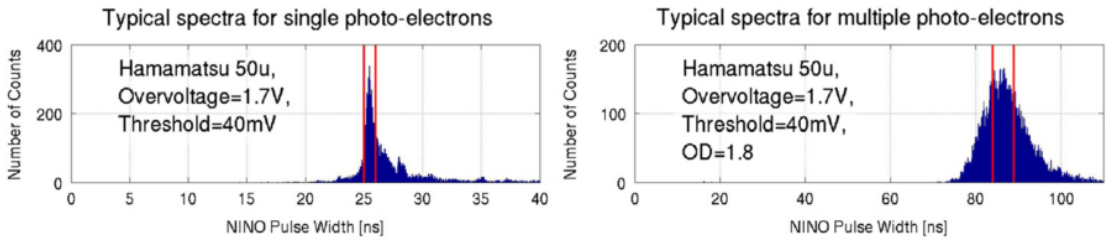

Figure 5.8: A typical single electron response is shown. The spectrum for the sum of several photoelectrons is also shown. This figure is reproduced from [77].

After extracting the data from this graph (left figure) and the skewness is found to be approximately 0.8. As shown in figure 5.7 this corresponds to a reduction in the potential CRLB CTR of 20%.

As we add additional contributions to the PDF later this chapter, we will assume a skewness of zero. This is for two reasons. Firstly it is easy find values for the TTS in reference but no systematic study has yet to been completed on the effect of skewness. Secondly we wish to reduce

the complexity of our model to ensure additional contributions are clearer to see.

5.6 Analytical Model for Light Transport

5.6.1 Derivation of the Analytical Model

We begin by looking at a point source of light with no preferred direction (isotropic) placed between two two-dimensional faces. The two faces are separated by a distance L. The source is set a distance (z) from one of the faces. The other face is therefore a distance $L - z$, where $L - z > 0$. Using the time-averaged Poynting vector, the power (P) incident per unit solid angle ($d\Omega$) can be defined as

$$\frac{dP}{d\Omega} = \frac{r^2}{2}\vec{n}.\vec{E} \times \vec{H}^* \tag{5.16}$$

where $\vec{n}$ is the direction of interest, $\vec{E}$ is the electric field and $\vec{H}^*$ is the complex conjugate of the magnetic field [79]. To model an isotropic light source, a spherical wave is used with equation 5.16 to find

$$\begin{pmatrix} \vec{E} \\ \vec{H} \end{pmatrix} = A_0 \begin{pmatrix} \hat{\theta} \\ \hat{\phi} \end{pmatrix} \frac{1}{r} e^{i\vec{k}.\vec{r}} e^{-i\omega t} \tag{5.17}$$

$$\therefore \frac{dP}{d\Omega} = \frac{A_0^2}{2}\vec{n}.\vec{r} \tag{5.18}$$

where $\vec{r}$ is the direction of propagation of the spherical wave. Integrating over the solid angle with ranges $\{\theta, \theta_1, \theta_2\}$ and $\{\phi, 0, 2\pi\}$ it can be shown that

$$P(\theta_1, \theta_2) = \int \frac{dP}{d\Omega} d\Omega = \frac{A_0^2}{2} \int_{\phi=0}^{2\pi} \int_{\theta=\theta_1}^{\theta_2} \sin\theta d\theta d\phi \tag{5.19}$$

$$= \pi A_0^2 (\cos\theta_1 - \cos\theta_2) \tag{5.20}$$

Consider θ_1 is zero with $\theta_2 = \theta$ we arrive at

$$P(\theta) = \pi A_0^2(1 - \cos\theta) \tag{5.21}$$

$$F(\theta) = \frac{P}{P_0} = \frac{1}{2}(1 - \cos\theta) \tag{5.22}$$

where P_0 is total power emitted by the single interaction. This can be seen to be $2\pi A_0^2$. To find the power per unit angle consider $\theta_1 = \theta$ and $\theta_2 = \theta + d\theta$, such that

$$dP = \frac{P_0}{2}(\cos\theta - \cos(\theta + d\theta)) \tag{5.23}$$

$$\therefore \frac{1}{P_0}\frac{dP}{d\theta} = \frac{1}{2}\sin\theta \tag{5.24}$$

Next we wish to expand this description to determine the fractional power per unit time arriving at one of the faces. For an isotropic source a distance z from the boundary we see

$$t(\theta) = \frac{nz}{c}\frac{1}{\cos\theta} = \frac{t_0}{\cos\theta} \tag{5.25}$$

$$\frac{d\theta}{dt} = \frac{1}{t_0}\frac{\cos^2\theta}{\sin\theta} \tag{5.26}$$

where n is the refractive index in the gap between the faces, c is the speed of light and t_0 is the minimum time to the z face. Combining this with equation 5.24 results in the rate of change of power with time giving

$$\frac{dP}{dt} = \frac{t_0 P_0}{2}\frac{1}{t^2} \tag{5.27}$$

Given a maximum allowed travel time, t_1, from equation 5.25 for the critical angle of the boundary, a PDF defining the light transport, $p_{\mathrm{LT}}(t)$ can be found by normalisation.

$$p_{\mathrm{LT}}(t|t_0, \theta_c) = A\int_{t=t_0}^{t_1} \frac{1}{t^2}dt = 1 \tag{5.28}$$

$$p_{\mathrm{LT}}(t|t_0, \theta_c) = \begin{cases} \frac{t_0}{1-\cos\theta_c}\frac{1}{t^2} & t_0 < t < t_1 \\ 0 & \text{Otherwise} \end{cases} \tag{5.29}$$

Equation 5.29 will correspond to light travelling in a direction towards the face only. For an isotropic source generated within a polished cuboid two 'modes' of light will be seen. These are one directly towards the photodetector, known as the forward mode, and another reflected back from the opposing face known as the backward. These modes will each carry a proportion of the total energy reaching the photodetector. The proportions we will be determined by the scintillator crystal's material, surface finish and any wrapping used. The time of arrival of each mode will be determined by the geometry and materials used. The minimum and maximum times of the forward modes will have the form

$$t_0 = \frac{nz}{c} \tag{5.30}$$

$$t_1 = \frac{nz}{c}\frac{1}{\cos\theta_1} \tag{5.31}$$

where θ_1 is the critical angle between the scintillator crystal and the photodetector. In this we assume perfect coupling (no air gap) at the interface. It is also assumed that all light falling outside the Total Internal Reflection (TIR) cone between scintillator crystal and air are lost. The backwards mode will have the additional complexity of the geometry and reflectance (R) of the scintillator crystal to include. The two times are

$$t_0 = \begin{cases} \frac{n}{c}(2L-z)(\frac{1}{\cos\theta_2}) & R = 0 \\ \frac{n}{c}(2L-z) & R \neq 0 \end{cases} \tag{5.32}$$

$$t_1 = \frac{n}{c}\frac{2L-z}{\cos\theta_1} \tag{5.33}$$

where θ_2 is the critical angle between the scintillator crystal and outer material (typically air). It is assumed that $\theta_1 > \theta_2$ as the refractive index mismatch between the scintillator crystal and the photodetector is typically low. The t_1 term in the backwards mode is given in terms of θ_1 for this reason. The form of t_0 is more complex as photons incident at low angles will escape the scintillator crystal[2] unless there is an additional property preventing their escape. Partial reflectance can by modelled by altering the proportion of energy given to each mode. The above definitions form the basis of the analytical description of the light transport PDF.

[2]see section 5.7 for inclusion of Fresnel reflection into the model.

In figure 5.9 the light transport PDF for a face separation of 20 mm, a centred interaction position and a refractive index of 1.8 (corresponding to LYSO) is shown. The scintillator crystal is surrounded by air and in contact with a glass window; thus giving critical angles θ_1 and θ_2 as arcsin $\frac{1.5}{1.8}$ and arcsin $\frac{1.0}{1.8}$ respectively.

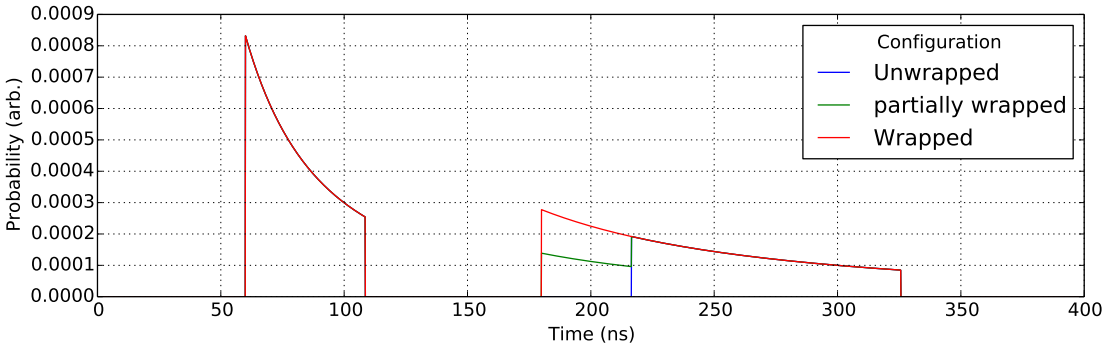

Figure 5.9: PDF for a polished scintillator crystal of $L = 20$ mm and $z = 10$ mm. The three configurations: unwrapped; partially wrapped and (specularly) wrapped, refer to reflectance values of 0, 0.5 and 1 respectively.

These distributions are plotted without normalisation to see the absolute change in the portion of energy coupled into the photodetector. In this case the forward mode, carrying 22% of the incident light, has a width of 50 ps regardless of reflectance. With increasing reflectance the amount of light reaching the photodetector increases from a total of 36% to 44%. The shape of the distribution matches the simulation shown in [22, figure 10].

The above analytical derivation makes few assumptions. Firstly we assume the entirety of the energy is emitted from a single point within the scintillator crystal, not over a line. For a sufficiently small region, this approximation is considered good [4]. Secondly there is no preferred direction of emission and no preferred direction of emission with time. Thirdly there's no relationship between energy of a given emitted photon and its time of emission. Given the spontaneous nature of electron-hole recombination, both these assumptions are expected to be true.

5.6.2 Analytical Light Transport Contribution to the CRLB

Using the specular light transport PDF we may now calculate its contribution to the CRLB CTR. To demonstrate the relative contribution of the light transport, we will calculate the CRLB each

time we include a new contribution. In figure 5.10 a flow chart of the CRLB calculation for each additional contribution included is given.

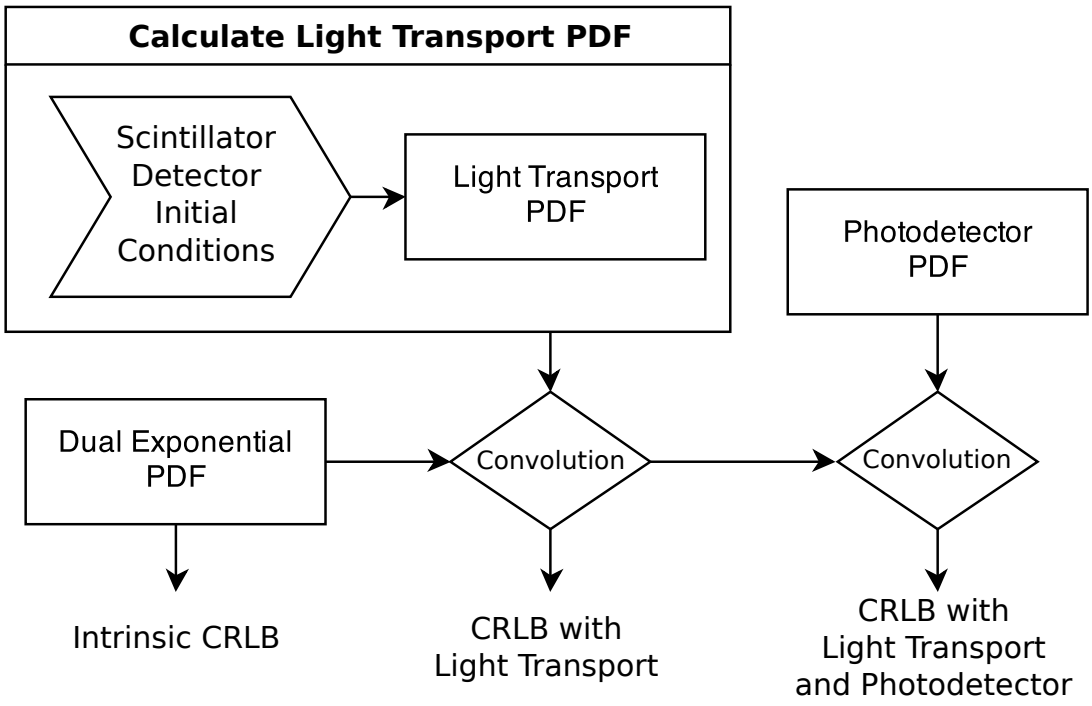

Figure 5.10: Calculation of the CRLB CTR with each of the three contributions. Three methods of calculating the light transport distribution are possible.

It can be seen that the CRLB CTR is calculated in logical sequence as each PDF would apply in the scintillator detector. For the analytical model we are essentially looking at the unwrapped configuration only. Therefore the number of events detected, n, needs be set appropriately. Therefore we choose a value of $\frac{3600}{2.3} \approx 1500$. The factor of 2.3 has been chosen as this is the drop seen in the light output when the wrapping is removed in light output measurements. See appendix A.2 for measurements and discussion of this ratio. The value of 3600 is chosen as there are 3600 independent cells [18]. This value is kept constant in all the following measurements unless otherwise stated. The CRLB CTR values for the unwrapped configuration using the analytical model is given in figure 5.11.

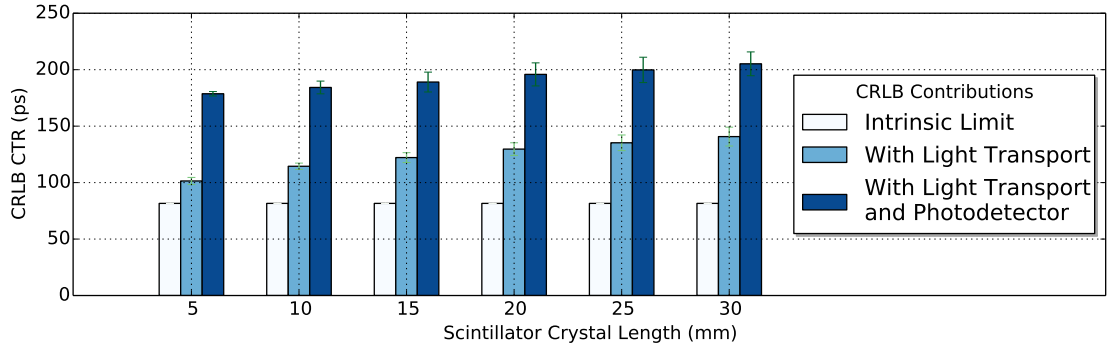

Figure 5.11: The CRLB CTR (in ps) is calculated for scintillator crystal lengths from 5 mm to 30 mm. The CRLB for the three contributions is calculated as described in figure 5.10.

In this, the CRLB values have been calculated for a range of DOI values across the scintillator crystal. A weighted mean of the CRLB values is then taken, based upon the gamma ray photon absorption length in LYSO. For 0.511 Mev gamma ray photons this is 12 mm [21] at 0.511 MeV. In this figure we can see several results. Firstly, as expected, the intrinsic limit CRLB due to the material does not vary with scintillator crystal length. Secondly with light transport we see that the CRLB does increase with scintillator crystal length. This matches our results from chapter 3. For a 30 mm scintillator crystal it can be seen that the light transport is responsible for approximately 30% of the CRLB. Therefore despite that the photodetector's contribution is currently larger, even for a TTS of only 70 ps, it shows that light transport plays a significant part in the degradation of the timing performance. The full results are given in table 5.1.

Table 5.1: The CRLB CTR for typical scintillator crystal lengths.

Scintillator crystal length (mm)	CRLB CTR Intrinsic limit (ps)	CRLB CTR ...and with Light transport (ps)	CRLB CTR ...and with photodetector (ps)
5	81.6	101.4±3.2	178.7±2.0
10	81.6	114.5±2.8	184.3±5.6
15	81.6	122.2±4.4	189.1±8.8
20	81.6	129.7±5.6	195.8±10.2
25	81.6	135.3±6.9	199.8±11.2
30	81.6	140.7±8.4	205.2±10.5

It should be noted that these results are for a low light output, in the unwrapped configuration. If we assume the light transport contribution does not change between configurations, we can

estimate the CRLB for the wrapped case. For example, for an LYSO-scintillator detector with a single crystal of length 20 mm the CRLB CTR becomes 129.1 ± 6.7 ps

5.6.3 Variation of the CRLB with Interaction Position

To compare to our radiation measurements described in Chapter 3, we can plot the CRLB against the depth of interaction (DOI). In figures 5.12, 5.13 and 5.14 we plot the CRLB CTR against DOI for 5 mm, 20 mm and 30 mm scintillator crystals respectively.

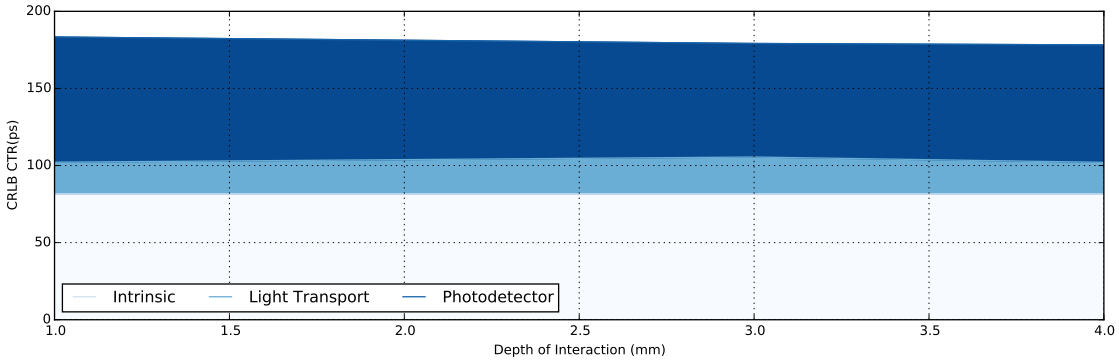

Figure 5.12: The CRLB CTR with DOI for a scintillator crystal of length 5 mm is shown. The peak to peak change from the lowest DOI to the highest is 183.4 ps to 177.3 ps.

In figure 5.12 the CRLB CTR against DOI for a 5 mm scintillator crystal is shown. We can see several things. Firstly the contribution of the light transport is at its lowest compared to the longer scintillator crystals. Secondly the change in the CRLB CTR with DOI is low; Only 183.4 ps to 177.3 ps peak to peak. This is a change of only 6.1 ps over the length of the scintillator crystal. Most records of high CTR performance are done using such short scintillator crystals

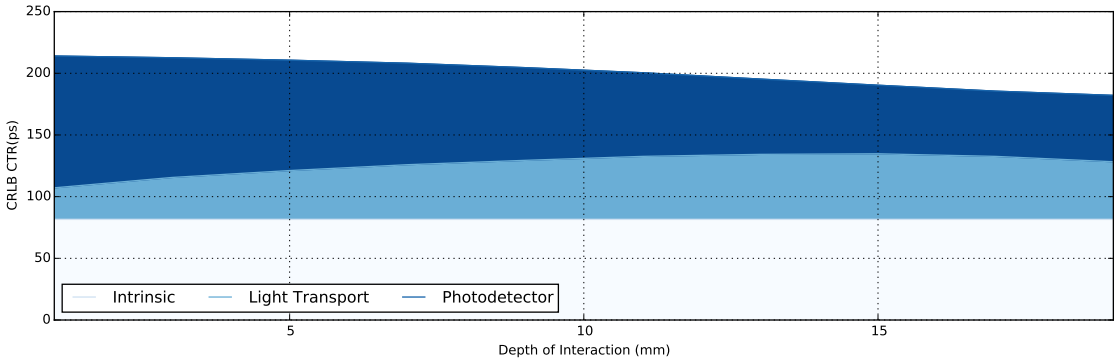

Figure 5.13: The CRLB CTR with DOI for a scintillator crystal of length 20 mm is shown. The peak to peak change from the lowest DOI to the highest is 214.0 ps to 182.1 ps.

In figure 5.13 the CRLB CTR against DOI for a 20 mm scintillator crystal is shown. In this the peak to peak variation is much larger, namely 31.9 ps from 214.0 ps to 182.1 ps.

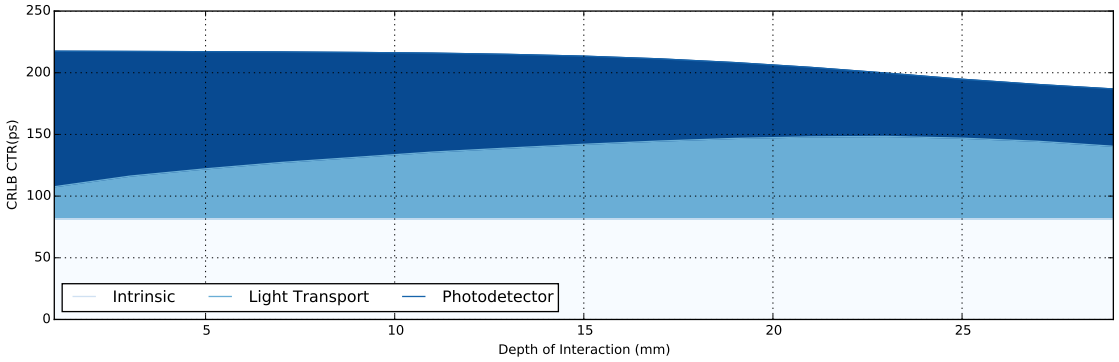

Figure 5.14: The CRLB CTR with DOI for a scintillator crystal of length 30 mm is shown. The peak to peak change from the lowest DOI to the highest is 217.5 ps to 186.8 ps.

Finally in figure 5.13 the CRLB CTR against DOI for a 30 mm scintillator crystal is shown. The peak to peak variation in this case is 217.5 ps to 186.8 ps giving a difference of 30.6 ps. However in the case of the 30 mm scintillator crystal the change is predominantly near where the DOI is close to the scintillator crystal length.

These results show that a drop in the CRLB CTR with DOI but only for long enough scintillator crystals and only at DOI values greater than half the scintillator crystal length. Below this half way mark, the CRLB CTR with DOI is fixed. The analytical results in figure 5.14 can be compared to the experimental results presented in figure 3.4. Looking at the blue triangle data points

representing the unwrapped measurements with DOI, it is possible the relationship shown does match that predicted by the analytical model. In table 5.2 the peak to peak data for the radiation measurements are given.

Table 5.2: The peak to peak values of the CTR against DOI measurements performed in chapter 3.

Sample	Configuration	Peak to Peak (ps)
20 mm LYSO:CeCa	Partially Wrapped	21.2
	Unwrapped	21.0
	Wrapped	17.9
30 mm LYSO:Ce (30A)	Unwrapped	28.5
	Wrapped	35.1
30 mm LYSO:Ce (30B)	Unwrapped	16.6
	Wrapped	23.2

We can see that for the unwrapped configurations the peak to peak (PTP) values are the same or lower than the values predicted from the model. This could be due to insufficient range in the measurements, namely that it is difficult to get reliable CTR measurements close to the edges of the scintillator crystal. Another, more probable solution is that in the DOI measurements a volume is excited by electronic collimation, not a fixed point. This could lead to an averaging effect which would damp out the change in the CTR.

In this work we consider the inclusion of this model of light transport to be correct for several reasons. Firstly the process is analogous to the process of transit time spread within photodetector. In both cases an individual quanta of information, namely a photon or photoelectron, is generated and will arrive at a given time with a known probability. As the CRLB model including the photodetector has been shown to be accurate [24, 72], it is likely that light transport can be treated in the same fashion. Secondly the analytical model describing light transport is simple and based on few assumptions. In the next section we will present a more complete model based upon a Monte-Carlo simulation of the scintillator crystal. In this we will see that the analytical model is a good description of the physical behaviour of light travelling through the system. Finally, several previous works have shown that degradation in the time resolution is present due to differences in geometry and surface effects. It is in the author's opinion that these effects can only be described by alterations to the light transport, and in this work the light transport PDF.

5.7 A Model Carlo Model based Description of Light Transport

In this section we present a Monte-Carlo simulation of the scintillator detector written by the author to generate the light transport PDF. Such a simulation allows much more complex physics to be included within the model. The simulation is open source and written in Python. The source code is available at `https://github.com/marksbrown/photontracing`.

The Monte-Carlo model works by simulating the progression of a large number of photons through a geometry until it reaches a sensitive surface. At this surface a photon may be considered to be 'detected'. At each 'time step' within the simulation the photon will progress to a new surface. The subsequent direction the photon travels in, if at all, will be determined by the probabilities assigned to various reflection models. Each of these models will be discussed in this section. After many such events are collected, the arrival times are histogrammed. The resulting distribution, after normalisation, gives the light transport PDF. As an added advantage of this method, the number of detected events can be estimated. This is done by

$$n = \text{Floor}(\frac{N_{\text{det}}}{N_{\text{gen}}}.4700) \tag{5.34}$$

where N_{det} is the number of photons detected by the photodetector face, N_{gen} is the number of photons generated in the run and 'Floor' takes the integer portion of the calculation. The value of 4700 is chosen from [24]. This is chosen as the maximum number of events detected per interaction for two reasons. Firstly this paper presents a metastudy of over a dozen papers on LYSO. The collected values from these works give the most reliable measure we can compare against thus far. Secondly as the purity and fabrication method of LYSO has improved over time, so has the light output [3]. Thirdly by comparison with equation 2.9, 4700 detected events corresponds to a scintillation yield in the range of 30,000 to 40,000 photons per MeV. Both of these points make 4700 a reasonable approximation.

5.7.1 Specular Contributions to the CRLB CTR

We will begin by replicating results discussed in the previous section on the analytical model.

In this section we will look at the behaviour of a $2 \times 2 \times 20$ mm^3 LYSO scintillator crystal. The excitation will be generated in the centre of the scintillator crystal, giving a DOI of 10 mm. The Monte-Carlo simulation will look at 100,000 photons per run. This is to ensure good convergence in the final result and ensure variance in the Monte-Carlo PDF is low.

Purely Specular

For purely specular reflection, the light transport PDF calculated using the Monte-Carlo model and the analytical model is shown in figure 5.15.

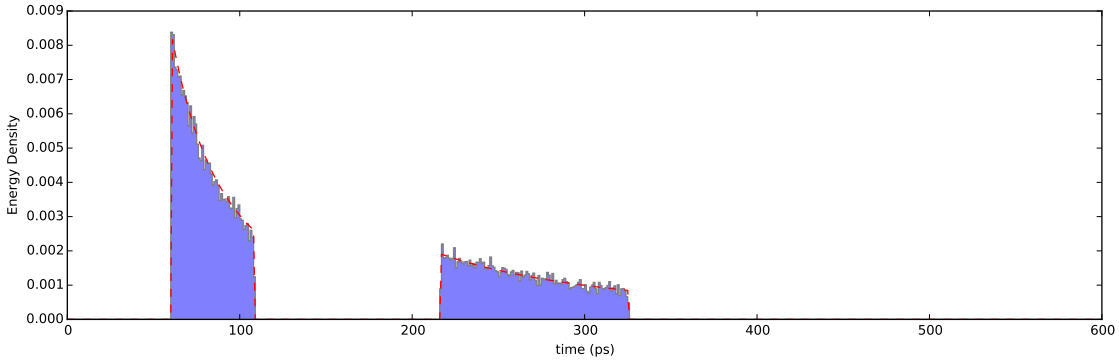

Figure 5.15: The light transport PDF is calculated from the Monte-Carlo model (shown histogrammed in blue) and from the analytical model (shown as a dashed red line). Both PDF's model a $2 \times 2 \times 20$ mm^3 LYSO scintillator crystal with a DOI of 10 mm.

In this figure we can see that the analytical model and the Monte-Carlo model match perfectly. In this simulation 78.2% of the generated photons escaped through all faces. 36.1% of light is seen to escape through the photodetector face. This corresponds to 1694 photons seen in the above figure. Using this PDF and this value we can estimate the CRLB CTR. The intrinsic CRLB CTR in this case is 78.4 ps. With the light transport the CRLB CTR becomes 126.1 ps. Finally with the addition of the photodetector the CRLB CTR becomes 194.8 ps. For a 20 mm scintillator crystal these values are in good agreement with table 5.1.

Inclusion of Fresnel

Next we will add Fresnel reflection. These are the amplitudes of transmission and reflection due to refractive index mismatch between materials. The derivation of the equations used can be

found in [79]. In figure 5.16 we show the light transport PDF along with the analytical model for comparison.

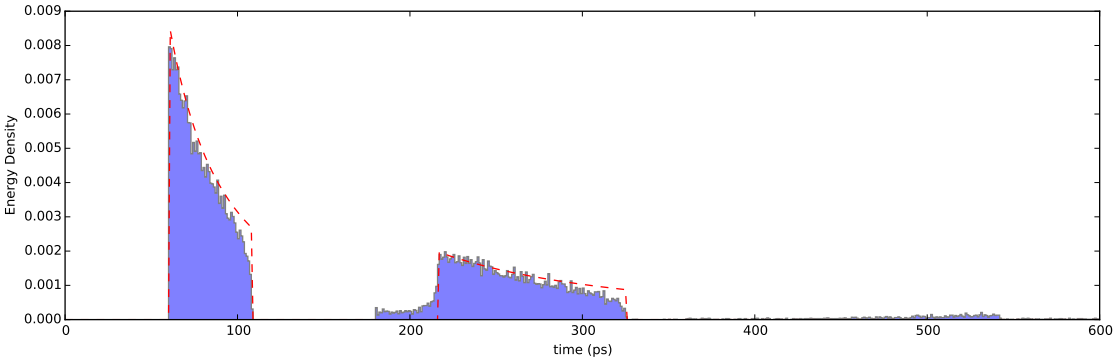

Figure 5.16: The light transport PDF is calculated from the Monte-Carlo model (shown histogrammed in blue) and from the analytical model (shown as a dashed red line). Both PDF's model a $2 \times 2 \times 20$ mm^3 LYSO scintillator crystal with a DOI of 10 mm. In this case we include Fresnel reflection.

In the above figure, the inclusion of Fresnel reflection has several effects. Firstly there is a visible tapering at the edges of both forward and backward modes. This is due to higher reflectance at oblique incidence angles close to the critical angle. Secondly we see a portion of photons from the backwards mode arriving before the bulk predicted by the analytical model. As discussed earlier in the chapter this will correspond to a non-zero reflectance. Thirdly we can see an additional mode after 400 ps. This corresponds to photons that did not escape from the forward mode to due the imperfect transmittance at the scintillator crystal/photodetector interface. In this case we see 78.4% of generated photons escape through any available face. Furthermore we see that 36.1% of generated photons escape through the photodetector face. Given that Fresnel reflection does not alter the direction of travel the lack of any change in the light output from the previous case is expected. However the number of detected events is now 1752. A minor increase we can attribute to non-zero transmittance through the side faces increasing the chance of some photons reaching the photodetector in sufficient time. Using this PDF we can estimate values for the CRLB CTR. In this case the intrinsic CRLB CTR is 77.1 ps. With the light transport contribution, the CRLB CTR becomes 127.6 ps. Finally with the inclusion of the photodetector, the CRLB CTR becomes 196.6 ps. This indicates that the contribution of Fresnel reflection upon the CRLB CTR for a

polished scintillator crystal is low. In this case below 1%.

Inclusion of Lobe

The final specular contribution we will see is Lobe reflection. This is whereby imperfections in the surface cause small deviations from the expected specular behaviour. In [54] this behaviour is modelled as a Gaussian distribution about the intended specular direction. The size of the deviation the paper predicts from measurement is 1.3°. In our own measurements in chapter 4 we see values similar to these.

Lobe reflection can be formally defined as specular reflection with an addition of a deviation vector, $\vec{m}$, of the form

$$\vec{m} = \underline{\underline{R}}(\vec{v}) \begin{bmatrix} m\cos(\phi_r) \\ m\sin(\phi_r) \\ 0 \end{bmatrix} \tag{5.35}$$

where $\underline{\underline{R}}$ is a 3×3 rotation to align the deviation vector such that $\vec{m} \times \vec{v} = 0$. $\vec{v}$ is the outgoing specular reflection vector without Lobe. Addition of the deviation vector, $\vec{m}$, is used to include the effect in the Monte-Carlo simulation. ϕ_r is a uniform random angle between 0 and 2π and m is the amplitude of the deviation. This is typically taken as the cosine of a sampling from a normal distribution with a scale describing the mean angular deviation from specular we predict. In this chapter we use a value of 1.3° [54].

In figure 5.17 we look at only the Lobe contribution without Fresnel reflection enabled.

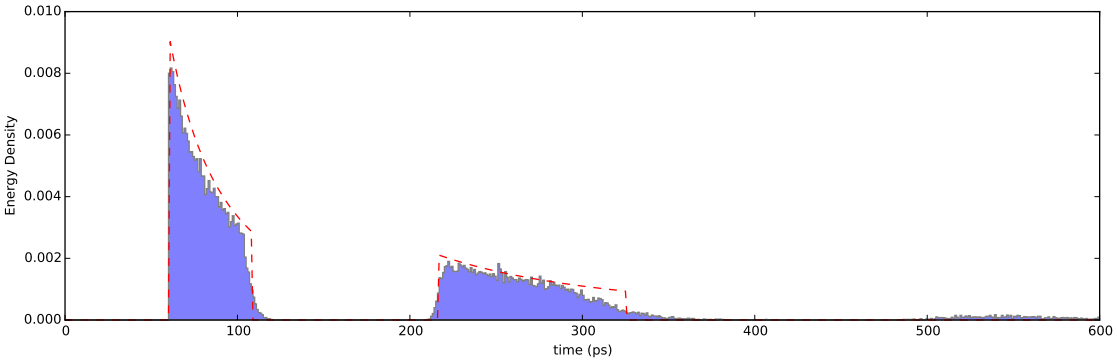

Figure 5.17: The light transport PDF is calculated from the Monte-Carlo model (shown histogrammed in blue) and from the analytical model (shown as a dashed red line). Both PDF's model a $2 \times 2 \times 20$ mm^3 LYSO scintillator crystal with a DOI of 10 mm. In this case we include Lobe reflection. A lobe angle of 1.3° is used to represent a polished surface [54].

In the Lobe reflection PDF shown above we can see several interesting effects. Firstly there is a small reduction in the amplitude of both the forward and backwards mode. Secondly there is a tail to both the forward and backward modes. Both effects correspond to photons initially destined to arrive on time, being deviated by the Lobe reflection.

In this simulation 99.7% photons escape. If we ran the simulation for a longer period this would tend to unity. This is for two reasons. Firstly we do not (yet) include bulk absorption and so photons exist forever. Secondly with sufficient time, a photon will receive a large enough deviation to reach a angle, with respect to a given face, below its critical angle and escape. The number of photons escaping through the photodetector face however is still low, namely 36.3%. This corresponds to 1870 detected events. This is an increase of over a hundred events compared to the purely specular Monte-Carlo model. Using this PDF we can estimate values for the CRLB CTR. In this case the intrinsic CRLB CTR is 74.7 ps. With the light transport contribution, the CRLB CTR becomes 126.1 ps. Finally with the inclusion of the photodetector, the CRLB CTR becomes 195.4 ps.

This is another small improvement in the CRLB over the purely specular case. This would indicate that low angle Lobe reflection, corresponding essentially to specular, is a negligible effect upon the CRLB CTR. In the next chapter we will explore larger angle Lobe reflection to determine if these have a larger effect.

Both Lobe and Fresnel

Finally, for completeness, we look at inclusion of both Lobe and Fresnel reflection, as shown in figure 5.18.

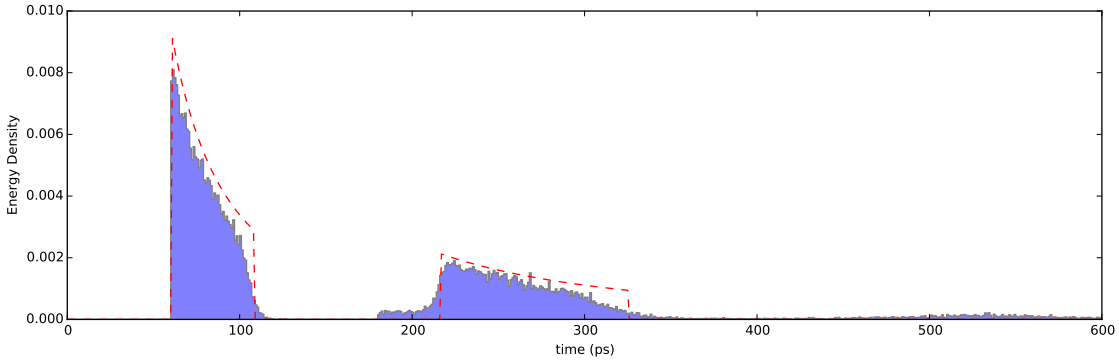

Figure 5.18: The light transport PDF is calculated from the Monte-Carlo model (shown histogrammed in blue) and from the analytical model (shown as a dashed red line). Both PDF's model a $2 \times 2 \times 20$ mm^3 LYSO scintillator crystal with a DOI of 10 mm. In this case we include Lobe and Fresnel reflection. A lobe angle of 1.3° is used to represent a polished surface [54].

In this 99.6% of light escapes with 1890 detected events corresponding to 35.9% detected. Using this PDF we can estimate values for the CRLB CTR. In this case the intrinsic CRLB CTR is 74.7 ps. With the light transport contribution, the CRLB CTR becomes 127.8 ps. Finally with the inclusion of the photodetector, the CRLB CTR becomes 197.6 ps. The full results of this section are given in table 5.3.

Table 5.3: CRLB CTR estimates for Fresnel and Lobe reflection contributions.

Fresnel	Lobe	Total Fraction Escaped	Detected Events	CRLB CTR Intrinsic (ps)	··· With Light Transport (ps)	··· With Photodetector (ps)
False	False	0.78	3676	78.4	126.1	194.8
False	True	1.00	4687	74.7	126.1	195.4
True	False	0.78	3685	77.1	127.6	196.6
True	True	1.00	4680	74.3	127.8	197.6

5.8 Discussion

In this chapter we have presented our preferred method for estimating the timing performance of scintillator detectors using a statistical inference technique known as Fisher information. We first use this technique to demonstrate that skewness in the photodetector PDF will change the expected CRLB CTR. In the section we show that a positive skewness of 0.8, such as one estimated from a real SER, will result in a CRLB CTR 20% lower than we expect. A more thorough study of skewness present using TCSPC with the MPPC in question could be useful in determining variation, if any, in the SER. As stated earlier, any variation in the SER will result in an increased uncertainty in the CRLB CTR and thus lead to a contribution to the error in any CTR measurement, regardless of DOI information.

Next we derive and present an analytical model for the light transport contribution within the scintillator crystal. This description of light transport is sufficient to model the effect of CTR degradation with scintillator crystal length. This can be understood as the variance of travel time for light transport increasing with scintillator crystal length. In terms of interaction position we can also see that we would predict some variation in the CTR. This variation is shown to be low and within experimental error compared to results presented in Chapter 3. We would recommend repeating the CTR against DOI measurements with two changes. Firstly reduce the volume of the radiation source to improve the effect of electronic collimation. This will reduce the effect of averaging which may be hiding the CTR variation with DOI. Secondly use an automated translation stage to alter the DOI. This will allow more measurements to be taken and in a more reliable fashion.

From the Monte-Carlo simulation results presented thus far, we would conclude that near-specular contributions converge to the same result as purely specular descriptions. In the next chapter we will explain the surface description to model more complex reflection processes. After a brief exploration of these properties describing the current system we will use this model to explore alternative modes of reflection.

Chapter 6

Exploration of Potential Methods to Improve the Timing Performance

Outline

In this chapter we will expand the CRLB model presented and validated in the previous chapter. The model describing the surface will be expanded to allow description of more complex effects, such as diffusive wrapping. Once done we will investigate some of these effect and determine their contribution to the timing performance. In doing so we wish to explore potential methods for improving the CTR of the scintillator detector. Note that in this chapter we will predominantly look at a scintillator crystal of size $2 \times 2 \times 20$ mm^3. This is due to its common usage in our previous measurements as well as its reasonable dimensions for actual use in a realistic gamma camera. In Section 2.2.3 the reasons behind this shape is discussed further. Finally it is worth noting that short scintillator crystals have been used to demonstrate very good CTR values [80]. As previously discussed, such short crystals will have poor sensitivity and are not useful in typical PET scanners.

6.1 The Two Layer Surface Model

6.1.1 Outline of Model

Scintillator crystals are typically wrapped or coated in a diffusive material to significantly increase the light output and improve timing and energy performance of the overall scintillator detector [69]. To model this behaviour within the Monte-Carlo simulation accurately, a two layer approach will be utilised. The schematic of the surface is given below in figure 6.1.

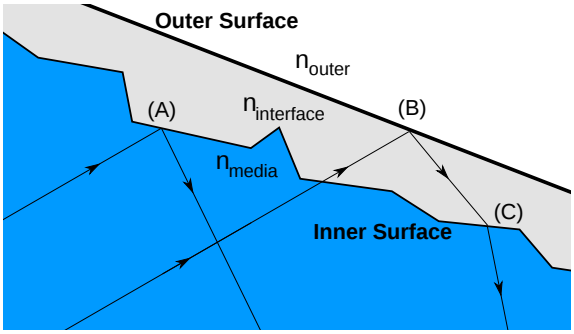

Figure 6.1: The two layer surface model employed within the Monte-Carlo simulation of photons within the scintillator crystal. There are three key interaction positions labelled as A, B and C upon the figure. These refer to the inner surface interaction, the outer surface interaction and the Snell's law interaction respectively. The three refractive indices, n_{media}, $n_{\text{interface}}$ and n_{outer}, refer to the material in which they are located.

In the above figure there are three positions, A, B, C, labelled. These can be described as

(A) **The inner surface interface.** Light reflected is described by specular and lobe reflections only. The probability of which is determined by usage of the Fresnel equations for unpolarised light[1]. The reflectivity parameter determines the probability of reflection back into the scintillator crystal. At this interface the parameter is set to zero, such that all reflections back into the scintillator crystal are due to the relative refractive index mismatch between n_{media} and $n_{\text{interface}}$ only. Transmitted light is deviated due to Snell's law before passing onto the next interaction.

(B) **The outer surface interface.** Light that has escaped the scintillator crystal is now within

[1]The Fresnel reflectance equations for the two linear (orthogonal) polarisations are chosen equally at random. Therefore we simply take the average of the TE and TM Fresnel values in each case.

a intermediary, interface, layer with thickness much greater than the light's wavelength[2]. At the outer surface only the reflectivity parameter is taken into account — Fresnel reflection is not taken into account. Any light not reflected is assumed lost. Reflected light is returned with a new direction determined by the reflection model describing the interface between $n_{\text{interface}}$ and n_{outer}.

(C) **Re-entry inner surface.** All photons reflected from the outer surface can have their direction of travel adjusted by Snell's law between $n_{\text{interface}}$ and n_{media}. No reflection or absorption is considered at this boundary[3]. This is based on the assumption that imperfect reflectance at the outer surface interface will prevent light propagation through the thick interface layer. This interaction can be switched off to model photons interacting at the interface layer rather than passing into it.

By incorporating refractive index mismatch at the two interfaces, the effect of intermediary materials can be investigated. In the next section we will expand work presented in the previous chapter to look at the effect of wrapping upon the CRLB CTR.

6.2 Incorporation of Diffusive Wrapping

An ideal diffuse material will scatter light into equal amounts per unit solid angle [81]. Known as a Lambertian emitter, the irradiance (power per unit solid angle) seen for a given polar angle θ is given by

$$E(\theta) = E_0 \cos\theta \tag{6.1}$$

where E_0 is the irradiance seen at normal incidence. For PTFE, a common wrapping material used with scintillator detectors, this scattering profile was observed Section 4.3. In this we saw the expected cosine behaviour with an additional specular Lobe component. When PTFE is wrapped about scintillator crystals the light output is seen to increase by a factor of 2.3 compared to the unwrapped case. For further results in area see Appendix A.2. Furthermore in figure 3.2 we can see

[2]Currently no time delay is implemented, however this would be simple to implement if required.
[3]Consideration of photons coupled into the interface layer is beyond the scope of this work.

that the quality of the wrapping will also affect the CTR observed. Our model should endeavour to explain both these effects.

In this chapter we will model PTFE as an ideal Lambertian emitter with unity reflectivity. This is to reduce the complexity of the model and allow a cleaner comparison with the unwrapped case discussed in the previous chapter. As in the previous chapter, discussed in Section 5.7.1, 100,000 photons are simulated per run. This is chosen to ensure the error is statistically insignificant. All other parameters are the same as described in the previous chapter, unless otherwise stated. To begin we will look at the effect of the interface layer upon the timing performance. In figure 6.2 the CRLB CTR with interface refractive index is shown.

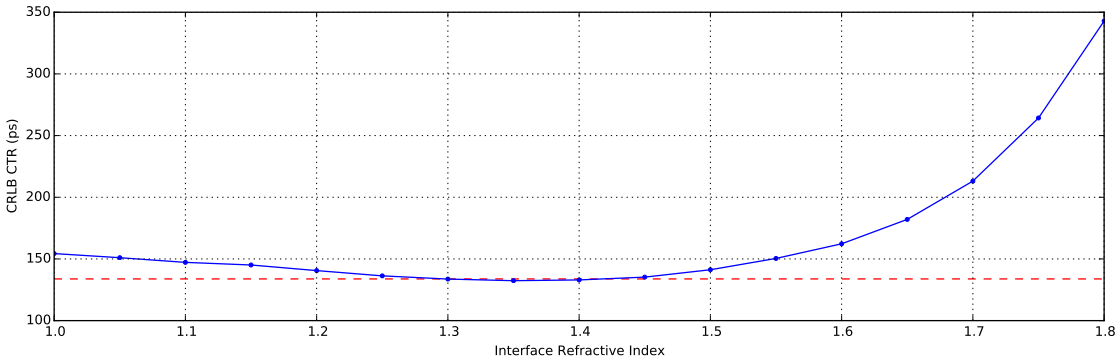

Figure 6.2: The CRLB CTR (in ps) is calculated for inclusion of PTFE with varying interface refractive index. It can be seen this reaches a minimum at 1.35 — The refractive index of PTFE.

From this figure we can see that imperfect coupling, below interface refractive index of 1.4, leads to a degradation in the CRLB CTR. This is primarily due to the drop in the light output. Above 1.35 the CRLB CTR is seen to dramatically increase.

To explore both cases we will look at three interfaces — air, PTFE and LYSO. These correspond to refractive indices of 1.00, 1.35 and 1.80 respectively. In figure 6.3 an interface refractive index of 1.00, corresponding to an air gap, is shown.

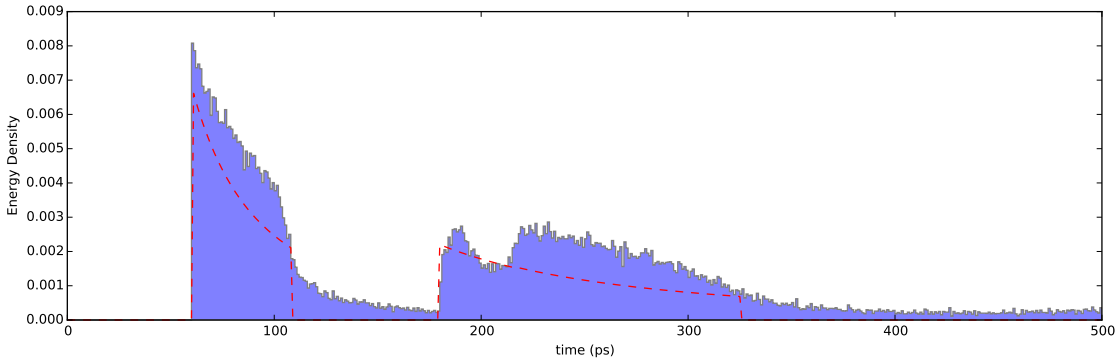

Figure 6.3: The light transport PDF calculated from the Monte-Carlo model with the inclusion of PTFE wrapping is shown. Poor coupling between the wrapping and scintillator crystal is implemented via the presence of an air gap ($n_{\text{interface}}$=1). The red dashed line corresponds to the analytical model, as described in the previous chapter, with 36% of energy escaping.

In the above figure 62.1% of the incident light escapes during the first 0.5 ns. This is a factor of 1.7 more than the Monte-Carlo case representing the unwrapped configuration. In this case the intrinsic CRLB CTR is seen to be 59.8 ps. With light transport this increases to 110.4 ps. With the photodetector, the CRLB CTR becomes 154.2 ps. This is an improvement of 43 ps or 22% in the CTR over the unwrapped configuration. Next we look at the 'ideal case'. In figure 6.4 an interface refractive index of 1.35, corresponding to perfect coupling with the wrapping, is shown.

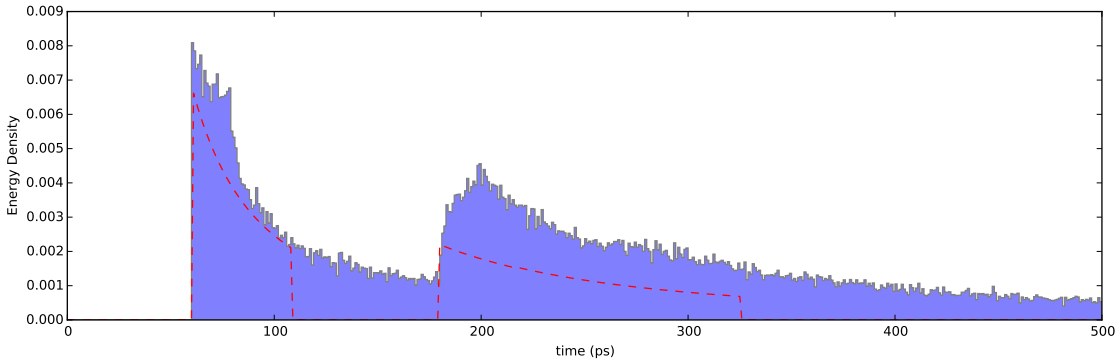

Figure 6.4: The light transport PDF calculated from the Monte-Carlo model with the inclusion of PTFE wrapping is shown. In this case good coupling is shown between the wrapping and the scintillator crystal ($n_{\text{interface}} = 1.35$). Such an interface would indicate perfect coupling between the wrapping and the scintillator crystal. The red dashed line corresponds to the analytical model with 36% of energy escaping.

In the above figure the CRLB CTR is seen to be 133.7 ps with 88% of incident light escaping

during the first 0.5 ns. This corresponds to a factor of 2.4 compared to the unwrapped configuration. This is slightly higher than the value seen in light output measurements, such as those in Appendix A.2. For this figure the intrinsic CRLB CTR is seen to be 50.3 ps. With the inclusion of light transport this increases to 102.1 ps. And with the photodetector the CRLB CTR becomes 133.8 ps. This an improvement of 64 ps or an improvement of 32%.

Comparing the two cases we can see that the CTR seen will be sensitive to the interface. Poor coupling, as seen in the Chapter 3, can lead to significant degradation in the CTR. The two cases show a difference of 20.4 ps or 13%. In table 3.4 a difference of 12% is seen between the best and worst 30 mm measurements. For 5 mm this is seen to be 10% and for 10 mm this is seen to be 9%. This would be weak evidence for the interface causing the time resolution degradation in the case of PTFE wrapping. Further study should look at diffusive coatings with different refractive indices up to 1.8 to determine if the relationship shown in figure 6.2.

Looking at both previous figures we can see that photons are arriving ahead, and about, the two modes seen for the specular cases only. This is consistent with a portion of the light not transmitted through the scintillator crystal normally reaching the photodetector earlier due to the presence of the PTFE wrapping. With good coupling this effect is even more pronounced showing strong increases over the two analytical modes alone. To determine if the shape of the light transport PDF is having a significant effect we can remove the contribution to the time resolution of the number of detected events. This done by comparing the ratio of their respective Fisher Information using, equation 5.8, to give

$$\frac{I_2}{I_1} = \frac{\mathrm{CTR}_2\sqrt{n_2}}{\mathrm{CTR}_1\sqrt{n_1}} \tag{6.2}$$

where I_i is the ith Fisher information, CTR_i is the ith CTR and n_i is the ith number of detected events. $\frac{I_2}{I_1}$ is the ratio of the Fisher informations. For the two CRLB CTR values from earlier in this chapter, 133.8 ps and 154.2 ps, a Fisher Information ratio of 1.04 is seen[4]. Using the above formula comparing the light transport CRLB values we see a Fisher Information ratio of 1.05. Both ratios imply that the predominant contribution to the CRLB CTR is the number of detected

[4]If $\frac{I_2}{I_2} = 1$ then $\sigma_1\sqrt{n_1} = \sigma_2\sqrt{n_2}$. Explicitly this means that the light transport PDF is not changing the timing performance.

events, not the curve shape itself.

Next we look at the case where the interface layer is set to a refractive index of 1.8. In this manner all photons will escape the scintillator crystal and interact with the PTFE. In figure 6.5 an alternative diffusive coating with a refractive index of 1.8 is shown.

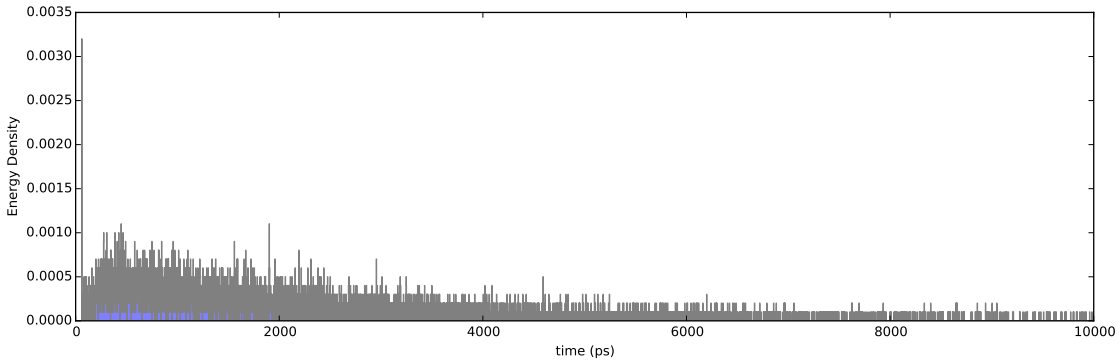

Figure 6.5: The light transport PDF calculated from the Monte-Carlo model with the interface layer refractive index set to 1.8. This can be interpreted as a diffusive coating of high refractive index rather than PTFE.

In the above figure the light transport PDF for a high refractive index ($n_{\text{interface}} = 1.8$) diffusive coating is shown. In this figure we can see a clear difference in the light transport PDF compared to the previous wrapped cases. In this case 15.3% of the light is detected in the first 0.5 ns. The intrinsic CRLB CTR is 49.8 ps in this case. With light transport, this dramatically increases to 249.0 ps. Finally with the photodetector the CRLB CTR becomes 269.3 ps. This is 72 ps, or 36% worse than the unwrapped case! The Fisher Information ratio between this model and the good coupling case is 2.7. Therefore we can conclude that the light transport PDF can significantly degrade the CTR however in optimal conditions this does not occur significantly.

Finally we can look at how the CRLB CTR varies with length. In figure 6.6 for good and bad coupling this is shown.

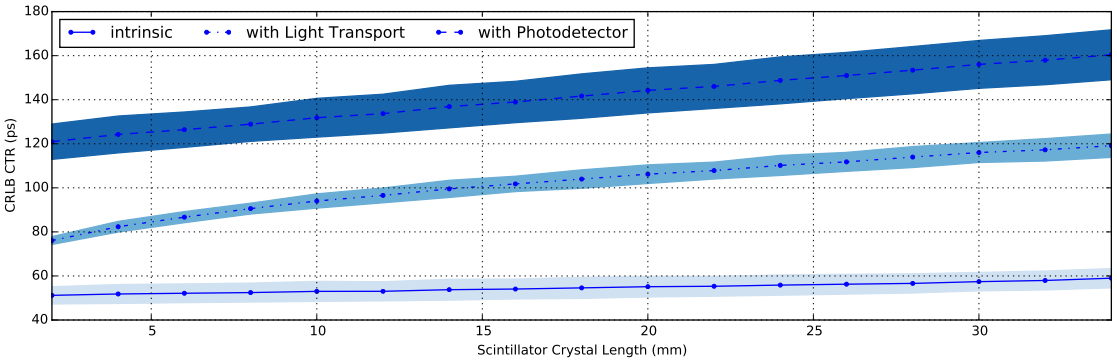

Figure 6.6: . The CRLB CTR with scintillator crystal length is shown with each contribution added in. The upper and lower bounds of each coloured region indicate the CRLB CTR calculated for the good and bad coupling cases, as described earlier in this chapter. The black lines indicate the mean between these two effects.

In this figure we show the variation in the CRLB CTR due to just the change in the refractive index of the interface layer. The black lines are the mean between the poorest (we expect) ($n_{\text{interface}}$=1) and the best ($n_{\text{interface}}$=1.35). Note that, since there is no material between the scintillator crystal and the PTFE, we do not expect the interface refractive index to exceed this value. We can see several interesting things in this figure. Firstly, as expected, the CTR degrades with increasing scintillator crystal length. Secondly the interface variation gives a first order estimate of the error in our CRLB predictions. For instance for a scintillator crystal of length 5 mm value of 130±20 ps is observed. This is a 15% error. Therefore for any improvement (or degradation) in the time performance to be clearly visible, we must aim to exceed this limit (or control the wrapping quality exceedingly carefully).

6.3 Alteration of Geometry

Before looking at more complex surface alteration models, we can consider non-cuboidal geometries. We will look at two such geometries — namely raised edge and trapeziums. We chose to look at these two geometries for a few reasons. Firstly, these two are chosen as both can be tessellated producing scintillator detectors comprised of many scintillator crystals. This is a common approach to maximise the available volume of coincidence and minimize the expense of photodetectors upon the final system. Secondly, these geometries will occupy a greater volume when placed into a ring

geometry, thus increasing the sensitivity of a resulting PET scanner constructed using them. The effect of this has been discussed in [82]. Thirdly, alteration of the surface angles with respect to one another would be a cheap method of altering the travel time through the scintillator crystal of generated optical photons.

6.3.1 Raised Edge Geometry

We will first look at the raised edge. In figure 6.7 three examples (one being the cuboid case) of the raised edge geometry are shown.

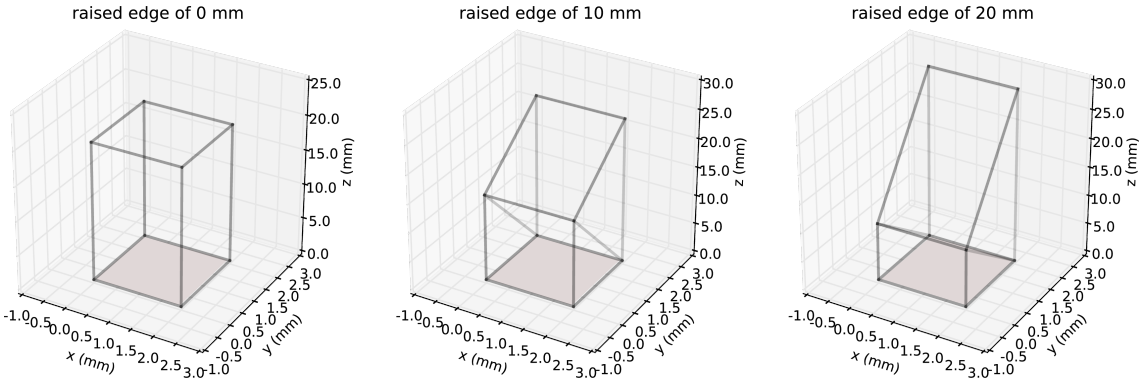

Figure 6.7: Three raised edge geometries are shown for a fixed cuboid length of 20 mm. The shaded face indicates the location of the photodetector.

To ensure the interaction position relative to the top and bottom does not change, the length of the scintillator crystal is reduced as the raised edge is increased. In this case we hold the depth of interaction in the middle of the scintillator crystal. To determine if the curve shape is related to the angle between the raised edge face and the photodetector or the excitation position, the CRLB CTR with scintillator crystal length for this geometry is calculated. In figure 6.8 the CRLB CTR (in ps) is calculated for a $2 \times 2 \times L$ mm^3 cuboid altered by introduction of a raised edge from 0 mm to L mm. In this case we look at three scintillator crystal lengths — namely 10 mm, 20 mm and 30 mm.

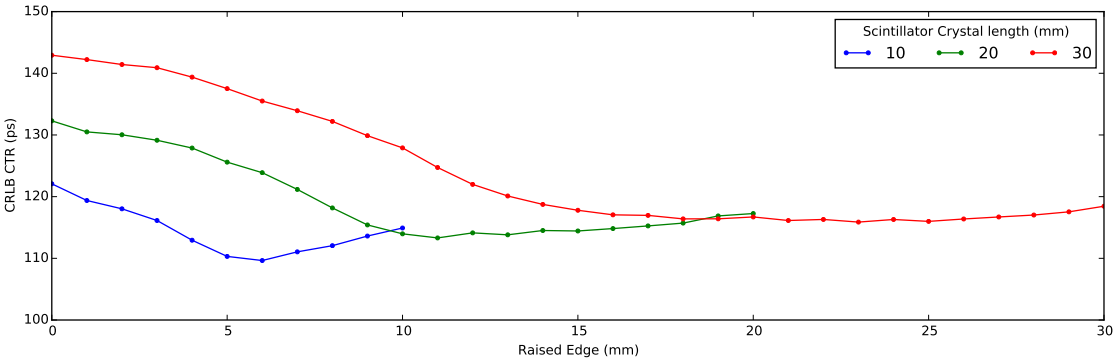

Figure 6.8: The CRLB CTR (in ps) is calculated for scintillator crystals of length 10 mm, 20 mm and 30 mm.

In the above figure we see several things of interest. Firstly in all three scintillator crystal lengths, the same shape is observed with raised edge. The results of which are given below in table 6.1.

Table 6.1: The minimum CRLB CTR (in ps) values for the raised edge geometry are given.

Scintillator Crystal Length (mm)	Minimum Position (mm)	Regular Cuboid CTR (ps)	Raised Edge CTR (ps)	Difference (ps)
10	6	122.1	109.6	12.4 (10.2 %)
20	11	132.3	113.3	19.0 (14.3 %)
30	23	142.9	115.9	27.1 (18.9 %)

These show a minima in the CRLB CTR at 6 mm, 11 mm and 23 mm for the 10 mm, 20 mm and 30 mm scintillator crystal lengths respectively. In each case there is an improvement in the CRLB CTR over the cuboid geometry. For the 20 mm case,an improvement in the CTR of 19 ps or 14% compared to the regular cuboid geometry is seen. In all three cases there is a convergence to approximately 117 ps. This would indicate that there is some universal degradation effect upon the time resolution in all three cases. To observe why this is, we can look at the light output with raised edge. The light output (expressed as a percentage) is given below in figure 6.9.

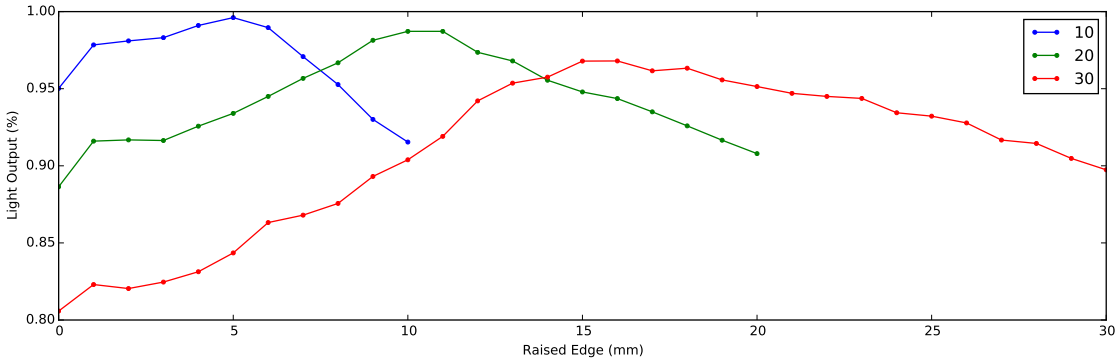

Figure 6.9: The light output (expressed as a percentage) with raised edge (in mm) is given for various scintillator crystal lengths.

In the above figure we can see that the light output reaching the photodetector increases to a maxima near the half way position of each scintillator crystal. In the case of the 20 mm scintillator crystal the light output increases by 10% from 89% to 99% from a raised edge of 0 mm to 10 mm. Using equation 6.2 would only explain an increase in CTR of 5% — Less than half the improvement shown above. Furthermore beyond this position we see the same drop off — indicating there is an optimal raised edge in each case and a degradation effect beyond this. Intuitively it can be seen that for high values of a raised edge, photons are reflected into high angles with respect to the photodetector. Therefore a larger portion of the backwards mode no longer escapes within the time period defined by the two (specular) modes. Finally we can look at the light transport PDF below in figure 6.10 for a raised edge of 10 mm and a scintillator crystal length of 20 mm.

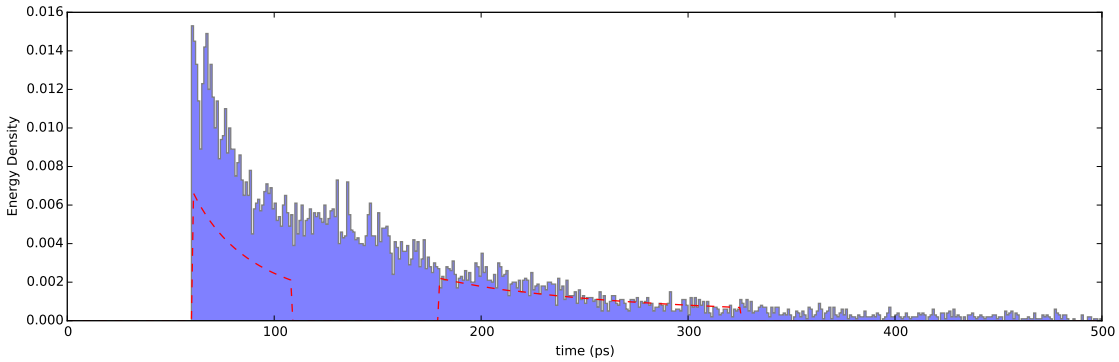

Figure 6.10: The light transport PDF for a raised edge of 10 mm for a $2 \times 2 \times 20$ mm^3 LYSO scintillator crystal.

In this figure there are several things we can observe. Firstly we can see a significant increase in the proportion of light reaching the photodetector sooner than the forward mode would predict for the unwrapped configuration. This effect leads to a large proportion of light arriving during the forward mode that would not do so in the regular cuboid geometry. Secondly the light arrives in a continuous fashion, rather than split into the two modes.

From the results in this section we would conclude that alteration of the face opposite the photodetector could be of some benefit to improving the time resolution. We will discuss this result further at the end of this chapter.

6.3.2 Trapezium Geometry

Instead of altering one face, we alter four to produce a trapezium geometry. We will consider a cuboid of volume $2 \times 2 \times 20$ mm^3 altered as shown below in figure 6.11.

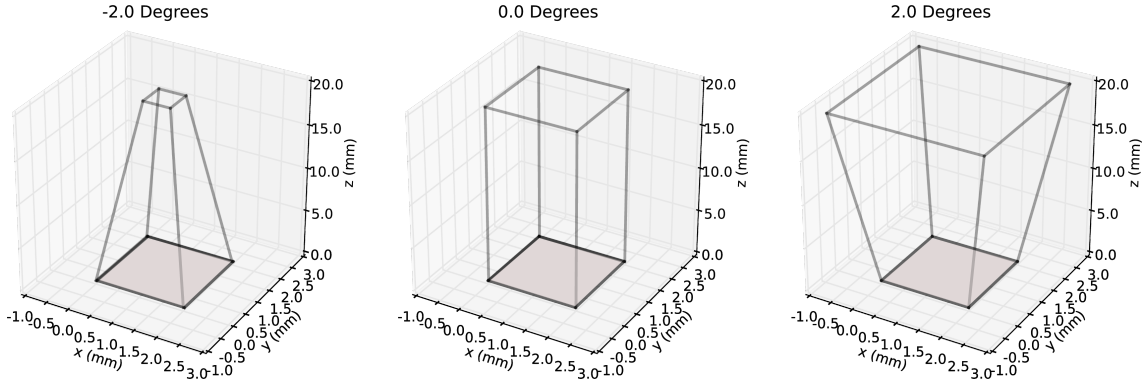

Figure 6.11: Three trapeziums defined by their angle, θ, relative to the photodetector face (shown shaded). All trapeziums are defined altered from a cuboid of dimensions $2 \times 2 \times 20$ mm^3. The shaded face indicates the location of the photodetector.

In this figure we demonstrate negative, zero and positive θ trapeziums. θ is the angle between the photodetector surface normal and a lateral face. For simplicity we keep the lateral faces tilted at the same angle as one another and fix the length of the trapeziums to 20 mm. The CRLB CTR (in ps) is calculated for varying θ below in figure 6.12.

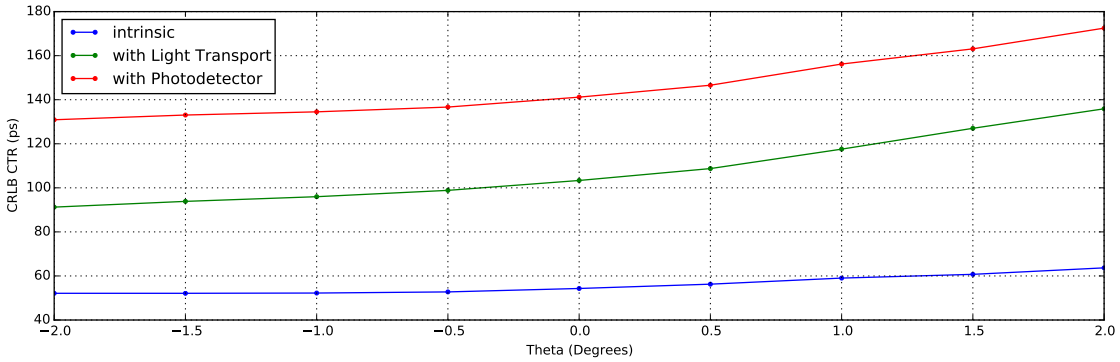

Figure 6.12: The CRLB CTR (in ps) calculated for different trapezium defined by an angle relative to the photodetector face normal.

For positive θ, there is degradation in the CRLB CTR. This is most likely due to an increasing portion of the forward mode arriving later at the photodetector simply due to specular reflection. As this will only be affected by the light output changing we can see that the proportion of photons arriving in the first 0.5 ns drops, thus leading to degradation in the time resolution. In figure 6.13 below we can see the light output with θ.

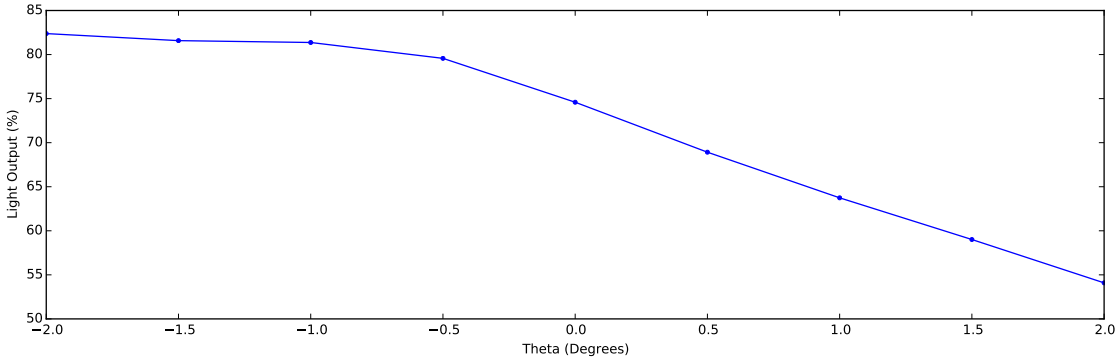

Figure 6.13: The light output with the angle θ for the trapezium geometry is shown.

In this case it can be seen that the light output drops significantly with positive θ. For positive θ little improvement in the light output is visible however the time resolution is seen to improve. At $-2°$ a CTR of 130.9 ps corresponding to a drop of 10.3 ps from the regular cuboid is seen. This corresponds to an improvement in the CTR of 7%. Interestingly this drop is not matched by a corresponding increase in light output, implying that the improvement is solely due to the change

in the light transport PDF.

In both the raised edge and the trapezium geometry it can be seen that alteration of the angle photons are scattered at will alter the time resolution seen. This would indicate that a mechanism for reducing the travel time to the photodetector, via scattering, from the interaction position will improve the time resolution. This will be explored further in Section 6.5.

6.4 Top Face Alteration

Much work has been completed in the investigation and creation of structures to improve light transmission through the top face of the scintillator crystal [83–85]. This work is predicated on the understanding that photons reflected due to refractive index mismatch (Fresnel and total internal reflection) lead to increased travel time for a portion of the forward mode. By reducing or removing this effect, it is hoped the CTR will be improved. In this section we will present results comparing three scenarios. These are

1. A LYSO scintillator crystal coupled to the photodetector with a layer of optical grease of refractive index 1.4 [44]. This is the case as described earlier in this chapter.

2. The same as case one, but the grease layer is replaced with an idealised Bragg grating. In this case we assume all photons incident below the critical angle are transmitted through the interface to the photodetector. This is modelled by switching off Fresnel reflection. However a secondary test for incident angle below and above the critical angle is still performed.

3. As case one, but the grease layer is replaced with a scattering structure. In this case all photons incident are transmitted through the interface to the photodetector, regardless of incident angle. This modelled by assuming no Fresnel reflection or critical angle test.

In figure 6.14 we find that the light transport PDF is not significantly altered from that presented in figure 6.4.

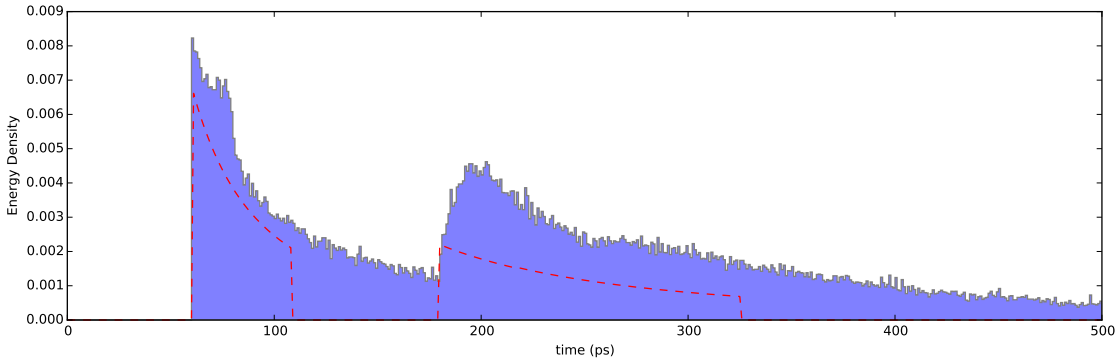

Figure 6.14: The light transport PDF with the inclusion of a scattering structure to improve coupling between the scintillator crystal and the photodetector present. The red dashed line corresponds to the analytical model with 36% of energy escaping.

In the above figure we find that the light output reaches 93.4%, an improvement over the 88% seen without it's presence. However this only results in an increase in the CRLB CTR to 128.9 ps from 133.7 ps — An improvement of less than 4%. This is well within the experimental error of measurement shown in Chapter 3. For the inclusion of a Bragg grating the results are essentially identical. The CRLB CTR reaches 128.8 ps for a light output of 93.4% in the first 0.5 ns. The change in the light transport PDF from the 'normal' wrapped configuration is shown below in figure 6.15.

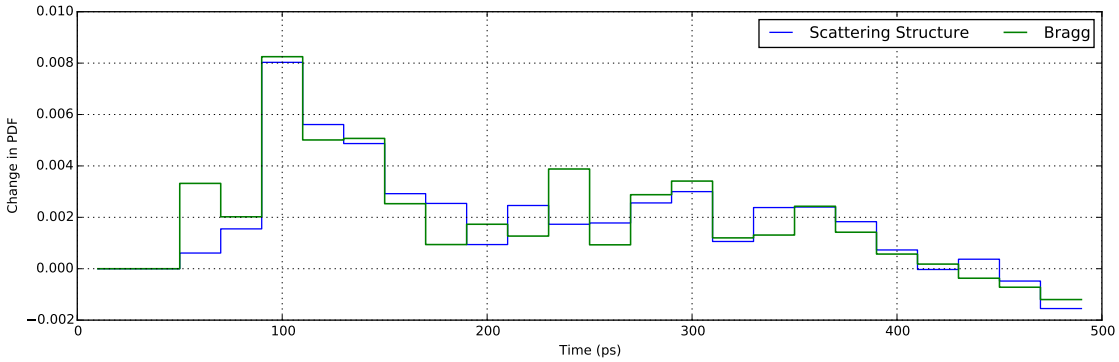

Figure 6.15: The difference in the light transport PDF with the inclusion of a Bragg grating or scattering structure compared to the wrapped configuration is shown. In this figure a bin width of 20 ps has been used to highlight the change in the PDF in a clearer fashion.

In the above figure we can see that the presence of any structure at the top face to improve coupling does increase the proportion of energy arriving earlier. The lack of difference between

the two cases implies that high angle photons are not a significant contribution to the CTR. In this wrapped configuration these photons will escape through the lateral faces and interact with the PTFE tape. A portion of which will then be transmitted with a shorter time than would be expected to the photodetector. Of these photons, which would be below the critical angle, the effect of the scattering structure and the Bragg grating would be the same — namely to negate Fresnel reflection. To further explore this effect we can repeat the above measurements, but in this case for an unwrapped scintillator crystal. In this case the change in the light transport PDF can be seen below in figure 6.16.

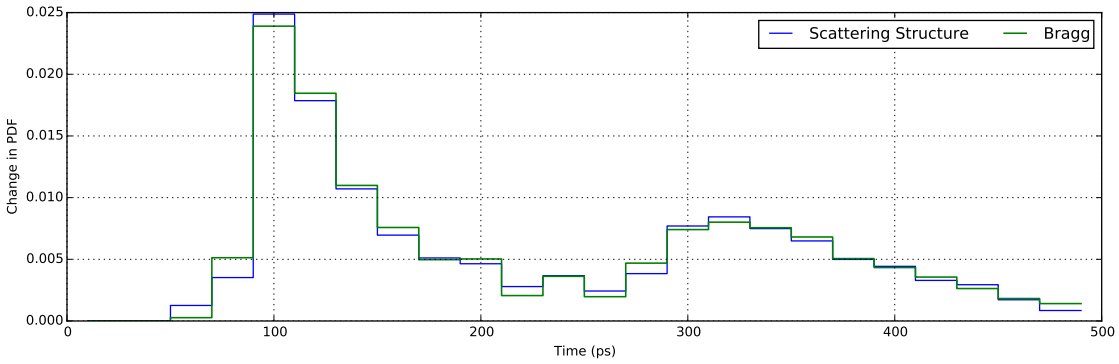

Figure 6.16: The difference in the light transport PDF with the inclusion of a Bragg grating or scattering structure compared to the unwrapped configuration is shown. In this figure a bin width of 20 ps has been used to highlight the change in the PDF in a clearer fashion.

In this figure a much more marked improvement in the light transport PDF is visible. Again there is little difference between the two cases. This larger improvement in the light transport PDF is borne out in the improvements in the CRLB CTR seen. The light transport PDF for the unwrapped configuration with the scattering structure present is given below in figure 6.17.

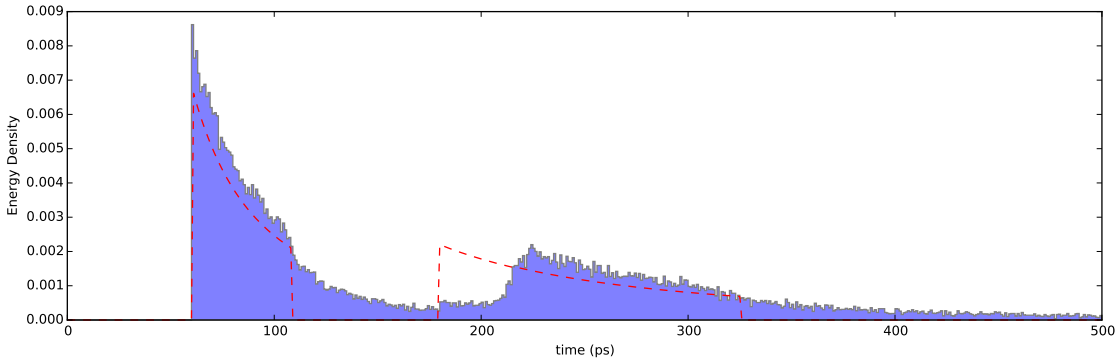

Figure 6.17: The light transport PDF with the inclusion of a scattering structure to improve coupling between the scintillator crystal and the photodetector present for the unwrapped configuration is shown. The red dashed line corresponds to the analytical model with 36% of energy escaping.

In the above figure a taper beyond the forward mode is seen. These photons would not escape in the unwrapped case as these correspond to photons trapped by refractive index mismatch. For this light transport PDF the CRLB CTR becomes 172.4 ps, from a value of 198.2 ps for the unwrapped configuration — thus demonstrating an improvement of 13%. The light output increases from 35.1%[5] to 48.7%. A very similar improvement is seen for the Bragg grating. The improvement in the CRLB is much larger (13% compared to 4%) in the case where no wrapping is present. We would conclude that photons arriving at high polar angles with respect to the photodetector can contribute to the time resolution. In the case of inclusion of wrapping, these photons are scattered at the lateral faces, overcoming the critical angle limitation due to the refractive index mismatch. When there is no wrapping, the scattering structure fulfils this role.

6.5 Lateral Face Alteration

In Section 6.3 it was seen that the angle of the lateral face relative to the photodetector will alter the time resolution. In this section we will look at exploring this further by creation of arbitrary reflection profiles. These profiles are presented without any justification for their physical possibility. The aim is to identify the relationship between angular confinement and the timing performance. Application of these profiles to one or more faces of the scintillator crystal will explore

[5]This value is slightly lower than that presented in the previous chapter due to the use of optical grease. As the grease used has a refractive index lower than the glass, there is a minor drop in the light output due to this.

the potential for improvement using such profiles. These will correspond to idealised scattering profiles for a potential nanostructure to be designed to perform. One such structure allowing theta confinement will be discussed in the next chapter.

6.5.1 Uniform Distribution

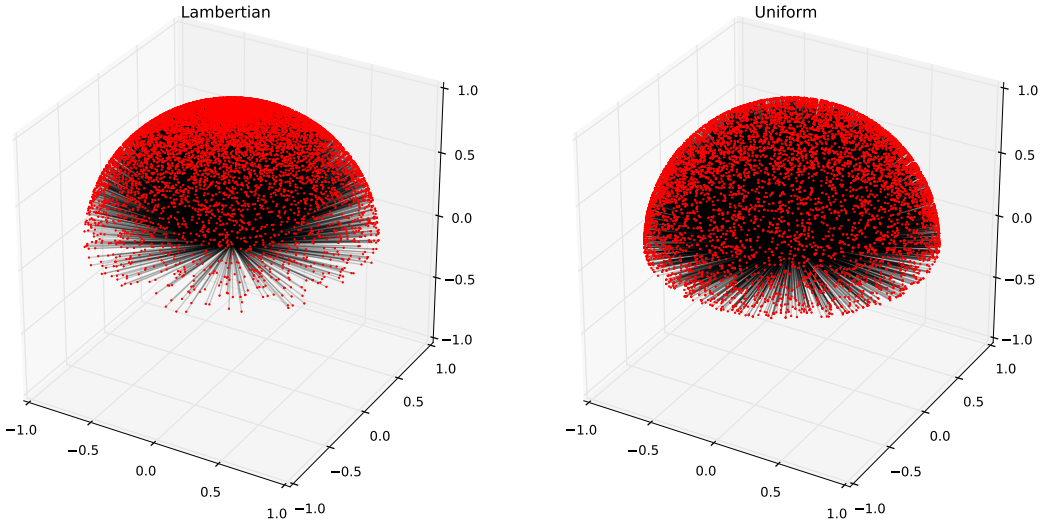

Figure 6.18: Uniform reflection profile compared to Lambertian profile showing 10,000 reflected photons.

To begin we will look at an unconfined case, namely photons given a random direction into a hemisphere [86]. This, compared to the Lambertian case discussed earlier in this chapter, is shown in figure 6.18. The difference between the two is made much more apparent if we calculate the polar angle of a large number of generated reflected photons, such as in figure 6.19.

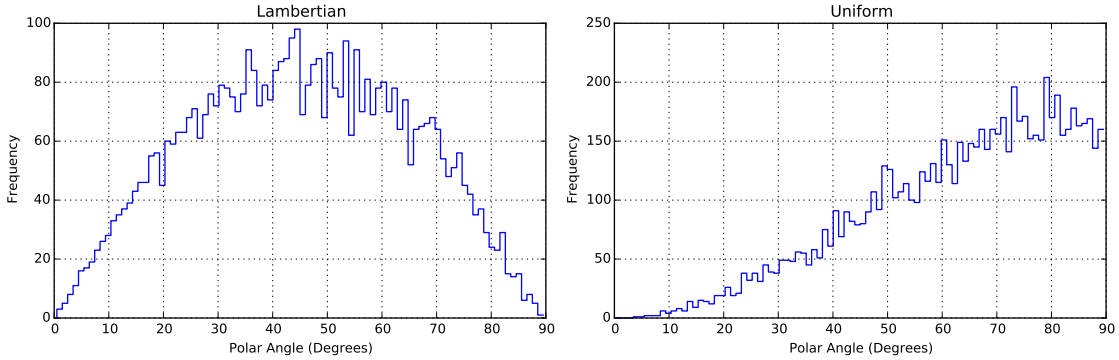

Figure 6.19: Histograms of the polar angle of Lambertian compared to the uniform directions are shown. Note that a sine correction is applied to correct for changing polar angle bin size.

In this figure we can see the expected cosine behaviour of the Lambertian distribution. In this section we will look at three cases using the uniform distribution. These are

1. None — Only PTFE is used. This corresponds to the wrapped configuration. This is the control in each case. In the following we assume good coupling, $n_{\text{interface}} = 1.35$ (see section 6.2).

2. Single — A single *lateral* face is converted to the given reflection profile.

3. All — All faces apart from the photodetector face (including the bottom face) are covered in the given reflection profile.

Using this uniform distribution for the three cases we calculate the CRLB CTR for various interface refractive indices. This is shown below in figure 6.20.

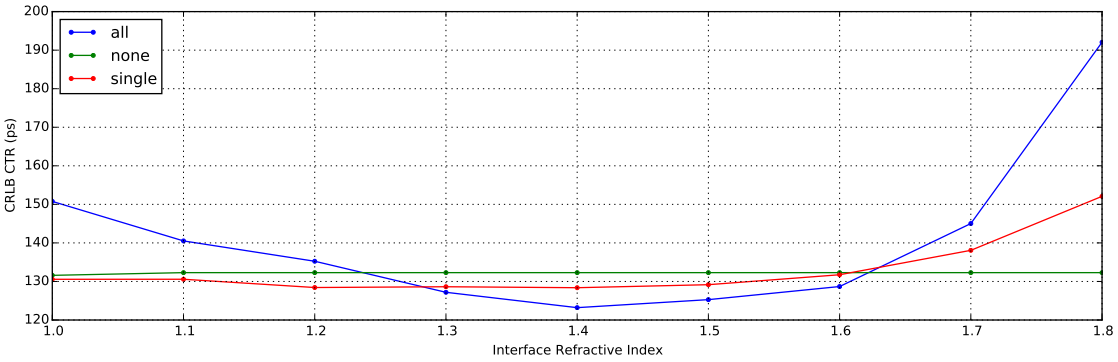

Figure 6.20: The CRLB CTR (in ps) is calculated for inclusion of the uniform reflection profile for various interface refractive indices.

In this figure we can see there is a minimum in the CRLB CTR for the all surfaces case at an interface refractive index of 1.4 — Corresponding to half way between 1.8 (the refractive index for LYSO) and 1.0 (for air). Note that the interface refractive index between the PTFE and LYSO does not change in the above figure, only between the customised surface and the scintillator crystal. It can be seen that both for the single and all case there are regions where the CRLB CTR is improved. At the minimum, this improvement is small — 3.9 ps (or 3%) for the single case and 9.1 ps (or 7%) for the all case. In the next two sections we will look at confining the uniform distribution. Any improvement should be larger that both of these values to attribute any improvement due to the confinement in question.

6.5.2 Polar Angle Confinement

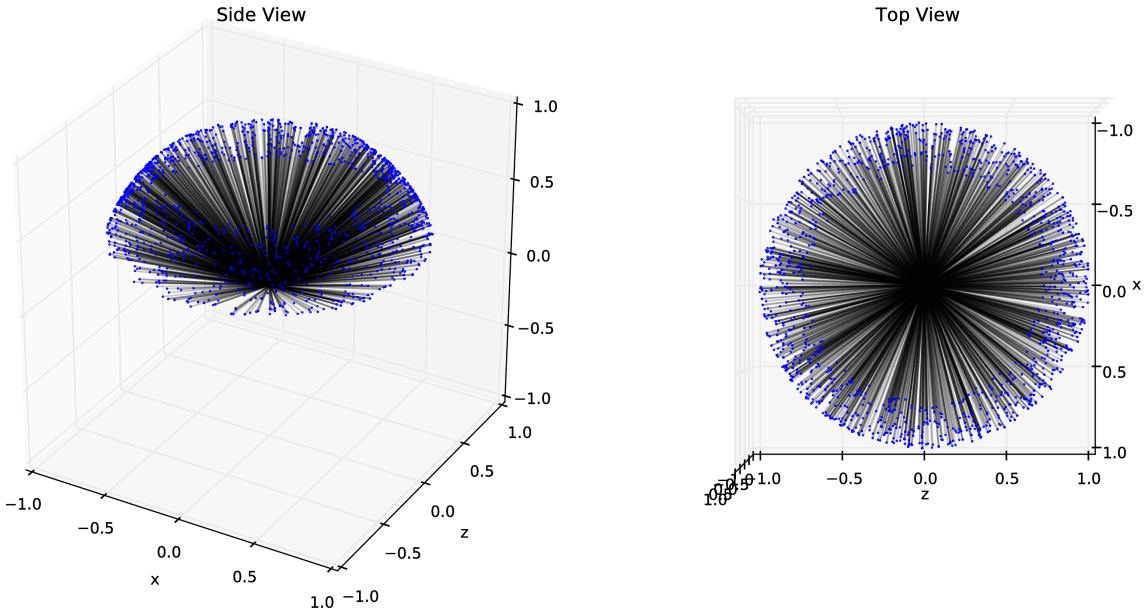

Figure 6.21: Reflection profile of 2000 reflected photons confined within polar angle range (θ_1, θ_2) shown. The polar angle range shown is between 40° and 70°.

In figure 6.21 the uniform distribution is altered to give polar angle, referred to as θ, confinement. In this case we defined a minimum and maximum angle, namely θ_1 and θ_2. For instance, in the figure above polar angles of 40° and 70° are shown to demonstrate the idea.

Polar angle confinement is attempted for a couple of reasons. Firstly, in section 6.3, it was seen that altering the angle that photons exit a face can change the time resolution. Photons with high angles with respect to the lateral faces will potentially reach the photodetector quicker than those trapped on slower paths. Secondly a Lambertian emitter, such as PTFE, has limited scattering into high angles however inclusion is seen to improve the time resolution. Therefore a 'designed' scattering surface could improve the time resolution.

As we wish to scatter photons incident at low angles, with respect to the lateral face surface normals, into high angles, but not affect those already at high angles, we can utilise the interface layer. In this manner we will alter the interface refractive index to prevent photons at low incident angles escaping, and thus interacting with the customised surface. In figure 6.22 we alter the interface refractive index for scattering into θ_1 and θ_2 of 80° and 90° respectively. These angles

are chosen as they reflect 'good confinement' and potentially scatter a good portion of photons toward the photodetector quicker than a comparable case using PTFE.

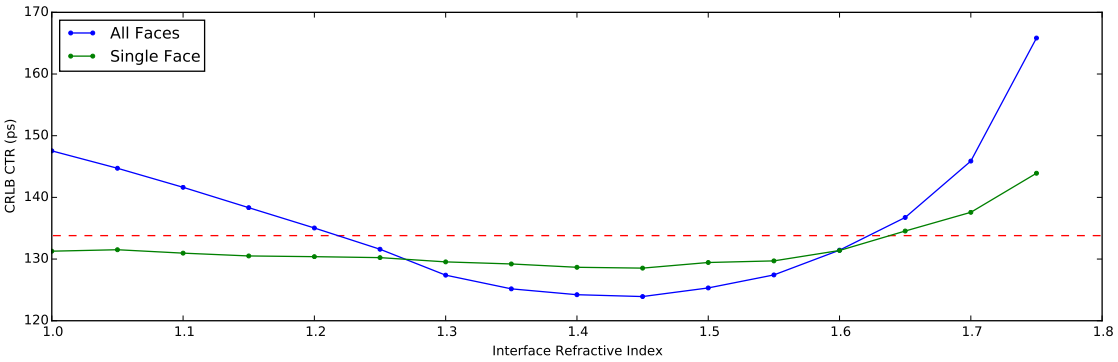

Figure 6.22: The CRLB CTR (in ps) is calculated against the interface refractive index. The optimal CRLB CTR with PTFE (as shown in figure 6.4) is given as a red dashed line. The green line shows the effect of changing one lateral face to the customised reflection profile. The blue line shows the effect of changing all faces, bar the photodetector face to the customised reflection profile.

At an interface refractive index of 1.4, the case with all faces altered (bar the photodetector face) sees an improvement of 9.9 ps or 7%. For a single lateral face altered this improvement is 5.3 ps or 4%. There is also an increase in the light output of 4.6% and 8.9% between for the single and all face cases respectively. As shown earlier in the chapter, using equation 6.2, these improvements in the light output correspond to improvements in the CTR by 2.5% and 5% respectively. The size of such an improvement is therefore minor and potentially not visible within experimental error. Furthermore we see the same levels of improvements for the uniform distribution. As the improvement in the CTR is at least in part due to the light transport PDF, the changes seen are given in figure 6.21.

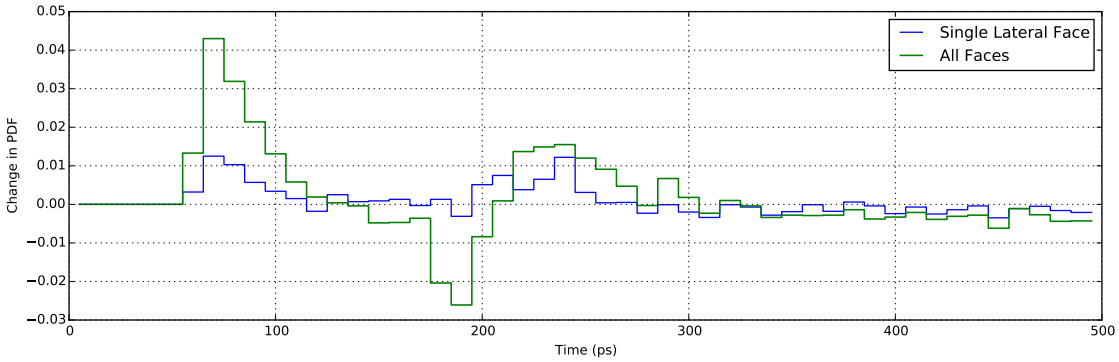

Figure 6.23: The change in the light transport PDF for inclusion of theta confinement surfaces is shown. A bin width of 10 ps is chosen to show the change. An interface refractive index of 1.4 is used.

In this figure we can see an improvement in the forward mode for both the single and all cases. Curiously we also see a degradation in the backwards mode in the all case. This would indicate that photons are being shifted between the modes in a positive fashion. The minor improvement in the CTR observed is most likely due to the limited reduction in the variance of photon path length to the scintillator crystal. This improvement however is much more attributed to the shift from Lambertian to uniform rather than from Lambertian to polar angle confinement.

6.5.3 Azimuthal Angle Confinement

In figure 6.24 photons are confined by azimuthal angle with respect to the surface normal.

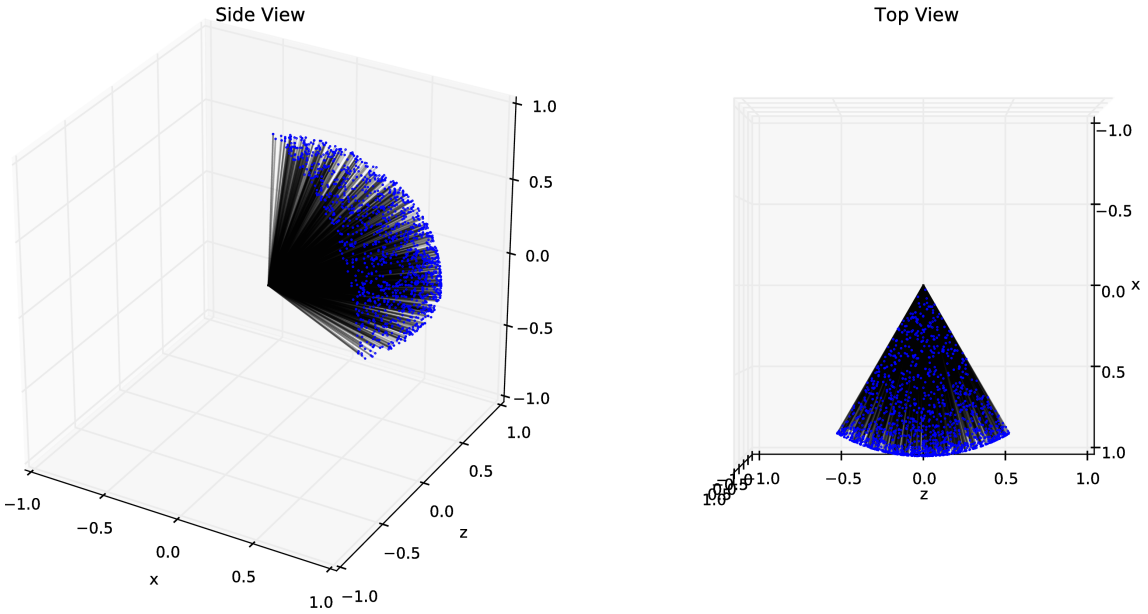

Figure 6.24: Reflection of photons from an idealised surface with phi confinement only. In this case a $\Delta\phi$ of 60°, in the positive x direction, is shown.

In this case we can see that there is a range of azimuthal angles which is forbidden. In this case photons outside the range of$-30°, 30°$ about the positive x direction are not allowed. Therefore the ϕ confinement angle, $\Delta\phi$, is 60°.

Azimuthal angle confinement can be used to reduce the number of photons reflected toward the bottom face. Therefore this model will lead to explicitly shorter path lengths. This is because photons from the backwards mode will be preferentially scattered towards the photodetector.

To begin we will look at the case where the interface layer refractive index is 1.8. This will maximise the number of photons interacting with the customised reflection layer. Following this we can explore the effect of the interface refractive index in this case. In figure 6.25 and figure 6.26 the CRLB CTR (in ps) is calculated against confinement angle, $\Delta\phi$.

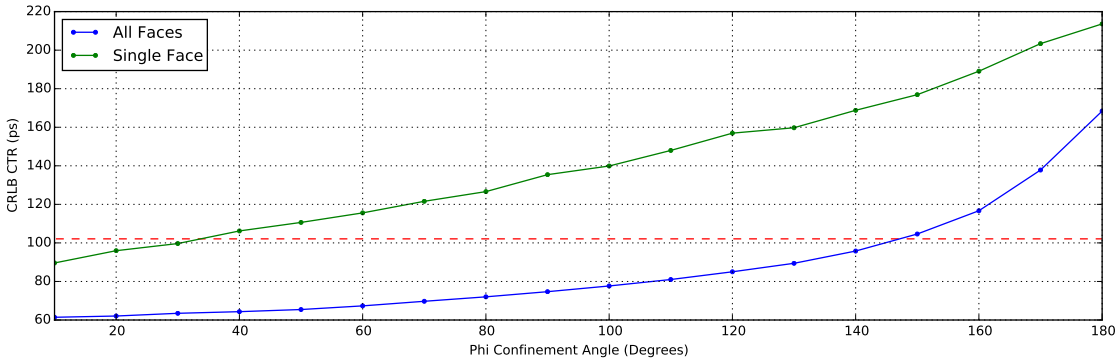

Figure 6.25: CRLB CTR (in ps) against confinement angle ($\Delta\phi$), including light transport, in the direction towards the photodetector face only. The red dashed line shows the performance of the good coupling case from PTFE in comparison. Green and blue lines correspond to single and all face coverage respectively.

In the above figure we see the CRLB CTR calculated with inclusion of the light transport contribution only. We initially look at just the light transport contribution (without the photodetector) to isolate the azimuthal angle confinement. It can be seen that for a single face, a high proportion of confinement is required to exceed the PTFE example — less than 30°. When the azimuthal angle confinement takes place on all lateral (and rear) faces there is a dramatic improvement in the timing performance. This is even more fascinating that it only requires minimal phi confinement to see performance greater than the PTFE good coupling case. In this case less than 150° will lead to timing performance beyond the wrapped configuration. This result confirms what we had discussed in chapter 3 about the importance of the geometrical contribution. This is an important result as it would potentially overcome the degradation in the time resolution due to scintillator crystal length. Below in figure 6.26 the CRLB CTR is calculated for the same phi confinement model, but this time including both the light transport and the photodetector contributions.

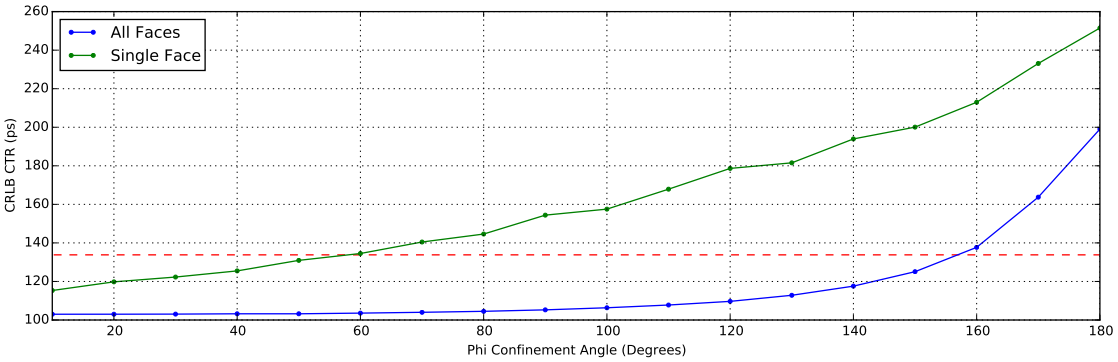

Figure 6.26: CRLB CTR (in ps) against confinement angle ($\Delta\phi$), including light transport and the photodetector, in the direction towards the photodetector face only. The red dashed line shows the performance of the good coupling case from PTFE in comparison. Green and blue lines correspond to single and all face coverage respectively.

There are few changes from the case including solely just the light transport shown in figure 6.25. Firstly inclusion of a single (lateral) face, with the phi confinement model, will now cause an improvement below 60° phi confinement rather than 30°. Secondly with all faces covered in such a phi confinement model, we surpass the wrapped configuration after 160° rather than 150°. Furthermore in this latter case after 90° the CRLB CTR reaches a minimum value of 103 ps. This is an improvement of 30.8 ps or 23% compared to the wrapped configuration. These changes can most likely be explained by the relative size of their contributions compared to the Gaussian describing the photodetector. As the light transport contribution goes below 70 ps, this becomes negligible compared to the larger photodetector contribution. As we discussed in section 5.4.1 a modern SiPM has a TTS FWHM value of 165 ps. Encouragingly this method of phi confinement offers a way of reaching sub-100 ps scintillator detectors if the photodetector contribution can be reduced further. In figure 6.25 values of 60 ps could be possible with LYSO as the scintillator crystal.

The reason for this dramatic improvement can be seen clearer if we observe the light transport PDF for these cases. In figures 6.27 and 6.28 the light transport PDF for the inclusion of the azimuthal angle confinement for the single and all cases are shown. These are for the high confinement cases, namely a min ϕ of $-10°$ and a max ϕ of $10°$.

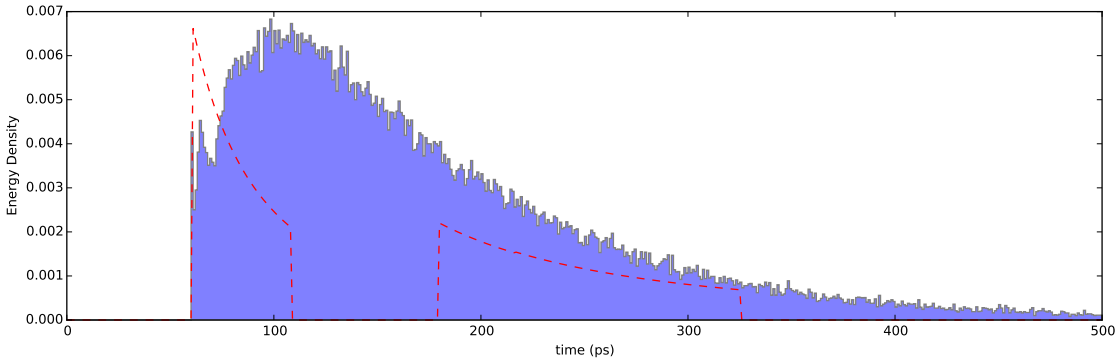

Figure 6.27: The light transport PDF with inclusion of an azimuthal angle confinement for a single (lateral) face altered. The red dashed line corresponds to the analytical model with 36% of energy escaping.

In the above it can be seen that the forward mode is shown to have dramatically increased in size relative to the PTFE good coupling case. This despite a minor drop in the initial portion of the forward mode leads to near complete light extraction in the first 500 ns. In the case of all faces, shown below, this effect is much more pronounced.

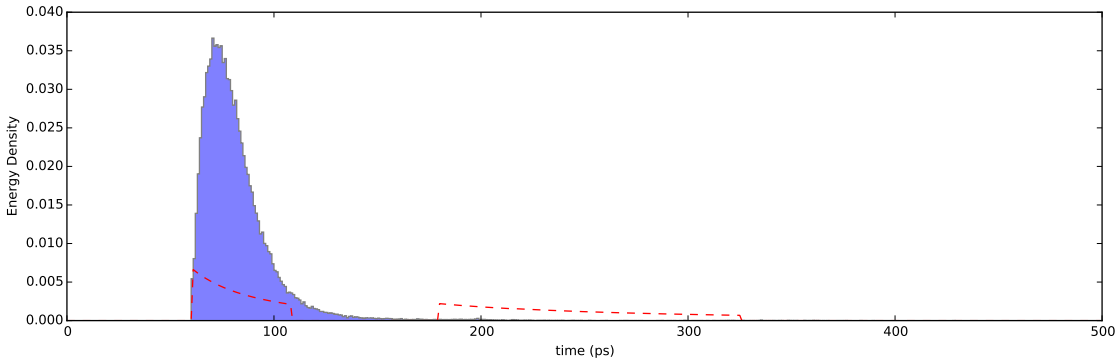

Figure 6.28: The light transport PDF with inclusion of an azimuthal angle confinement for all lateral and bottom faces altered. The red dashed line corresponds to the analytical model with 36% of energy escaping.

In this case it's clear that the forward mode has been significantly improved due to the inclusion of the azimuthal angle confinement. A portion of the improvement in the CRLB CTR can also be attributed in the increase in the light output — In this case close to all the light escapes within the forward mode.

Again using equation 6.2 the Fisher ratio can be calculated. This gives values of 1.09 and

1.22 for the single and all cases respectively. Therefore we can conclude that azimuthal angle confinement not only increases the light output it also improves the light transport, reducing its contribution to the CTR.

6.5.4 Highly Directed Confinement

In this final case we utilise both azimuthal angle and polar angle confinement. This can be considered the idealised light transport case for a cuboidal geometry. In figure 6.29 an example of this high confinement is shown.

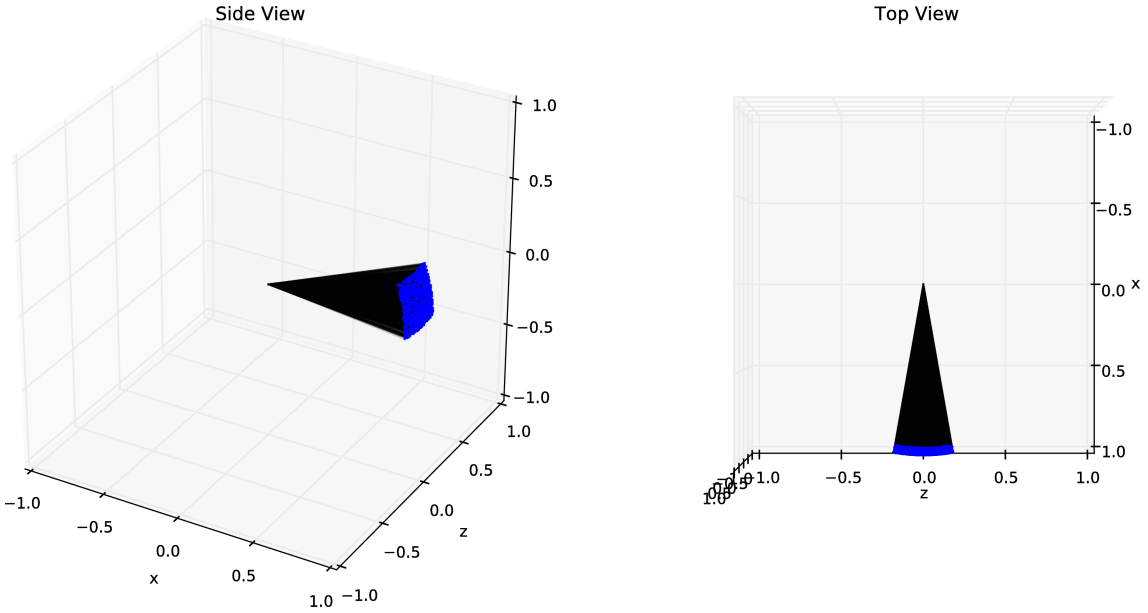

Figure 6.29: Reflection of photons from an idealised surface with azimuthal and polar angle confinement. In this $\Delta\theta$ is 20° and $\Delta\phi$ is 20°.

The calculations described in the previous section are now repeated for varying $\Delta\phi$ but with a significantly reduced $\Delta\Theta$ of 10°. The results of which are shown below in figure 6.30.

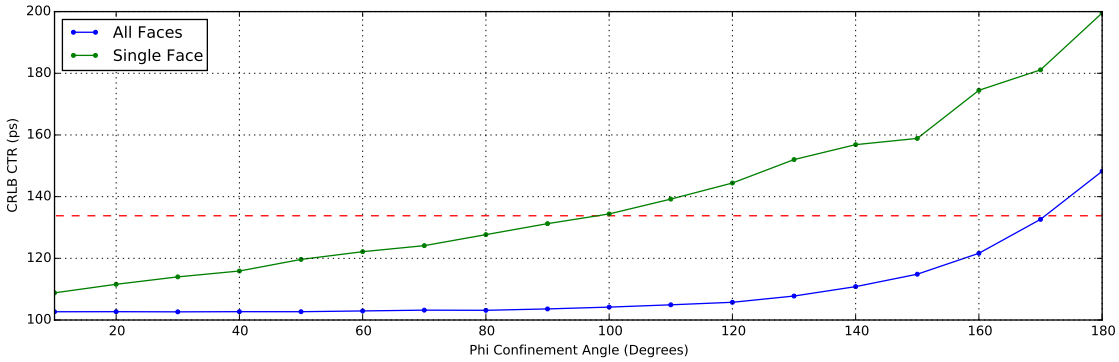

Figure 6.30: The CRLB CTR (in ps) is calculated against $\Delta\phi$ for the highly confined model. The red dashed line shows the performance of the good coupling case from PTFE in comparison. Green and blue lines correspond to single and all face coverage respectively.

In this figure we can see several changes from figure 6.26. Firstly the single face will now cause improvement for any $\Delta\phi$ below 100° rather than 60°. Secondly for all faces changes an improvement will be seen for any $\delta\phi$ below 170°. This latter case essentially corresponding to θ confinement only as described in section 6.5.2. In the limiting case where $\Delta\theta$ and $\Delta\phi$ tends to zero, the lowest CRLB CTR seen is still 103 ps. This effect is attributed due to the photodetector contribution once again becoming the only contribution of any significant size.

6.6 Discussion

In this chapter we have presented both existing and potential mechanisms for improving the timing performance of scintillator detectors. We began with the inclusion of PTFE (diffusive wrapping). Exploration of the variance introduced by differences in wrapping coupling offers a good description of the variation in CTR observed in Section 3.4. For good coupling, this set the benchmark that all potential improvements must match. Importantly in this section we determined that the interface refractive index is of critical importance in light transport. This matches the results presented in Section 3.4.

The work on PTFE looked at an idealised Lambertian emitter. This was for two reasons. Firstly introduction of additional variables would add additional complexity and make it more difficult to isolate the effect of diffusive scattering upon the timing performance. Secondly incorporation

of incident angle dependent scattering is a complex topic and would require further expansion of the photon simulation tool. Once done this would allow inclusion of scattering profiles from BRDF measurements performed using the imaging sphere. Similar work has been performed before in [66]. In this it was seen that near-specular, Lobe, reflections could be fairly approximated but more complex surfaces still had a large deviation.

In the next section we looked at geometrical alteration to improve the timing performance. In this we found that both raised edge and trapezium geometries would lead to improvements in the CTR. Further work should look at improvements once incorporated into tessellating bulk scintillator detectors to determine if sensitivity can be improved whilst maintaining or improving the timing performance.

Finally we looked alteration of the reflection model itself. In this we aimed to confine photons into preferential directions to determine if this would not only increase the light output but reduce the variance in light transport PDF. It should be noted that the alterations are presented without reference to how such phase changes would be implemented. Our aim is purely to observe the effect of angular confinement, not to explain how to accomplish this.

We began by looking at uniform, isotropic, scattering. Crucially this approach requires no control over the far-field. In this we found that, for an appropriate choice of interface refractive index, an improvement of 7% over the PTFE case was possible. The same level of improvement was seen for polar angle confinement. This would imply that isotropic scattering improves the CTR regardless of outgoing polar angle. To explore this we looked at azimuthal angular confinement. In this we found dramatic improvements in the timing performance. In some cases it was seen that the light transport contribution could be rendered negligible compared to the photodetector contribution to the PDF. Finally we looked at inclusion of both types of confinement. When this is done it is seen that the lower bound determined by the photodetector contribution is not reduce however it is reached for poorer confinement quicker.

As we will see in the next chapter, accomplishing such scattering structures presents many challenges. Not least that coherent scattering of isotropic incoherent light into useful far-field patterns is not within the abilities of phase-based scattering. However to demonstrate one potential direction of work we will look at producing polar angle confinement using arrays of dipole scatterers.

Future work in this area should look at inclusion of the effect of losses upon the CTR. Bulk

losses can already be understood as a drop in the light output and modelled using equation 6.2. Surface losses due to light escaping or ohmic losses should be explored further to determine the lower bounds on the performance of such surfaces.

Chapter 7

Polar Angle Confinement by Reflection from Scattering Array

7.1 Introduction

7.1.1 Outline

In this chapter we will present a prototype design for preferentially scattering light into high polar angles. In the previous chapter we discussed the benefits of such structures upon the timing performance. We look at polar angle, rather than azimuthal angle, confinement for two reasons. Firstly simulating and optimising an azimuthal angle structure will require significantly more run time. This is because there is no (longer) any azimuthal angle symmetry to exploit. Due to this, such an optimisation will require many incident directions to be simulated to accurately predict the final performance. Secondly polar angle confinement is a smaller alteration from specular reflection. Essentially we require the outgoing angle to exit at a marginally higher exit angle — thus shallower with respect to the surface. Such deviations from specular reflection are discussed in [87]. In this paper the introduction of a phase gradient to alter the relationship between incoming and outgoing directions is discussed.

To begin we will explore past and present work that have incorporated top and lateral scintillator crystal surface alterations to improve scintillator detectors. Following this we will establish the

initial conditions of the system in terms of light as well as a metric to quantify any improvement. The remaining bulk of this chapter will focus on the methodology of designing such a structure for incoherent light using the scattering differential cross section.

7.1.2 Nomenclature

An array of two dimensional scatterers upon an interface between two media will be referred to as a metasurface. A metasurface is a metamaterial confined to two dimensions. As in metamaterials, desirable bulk scattering behaviour is engineered however much less material is used. Furthermore due to the thinness of such structures there is potential for lower losses [88]. Since the interaction position within the scintillator crystal cannot be controlled, the metasurface should be designed such that an isotropic source of photons is created directly below it. In this approach we see that for the interaction position to always appear below the metasurface, the scattering structure must be periodic.

7.2 Background

7.2.1 Top Face Alteration

The biggest studies in this field are alteration of the top face [84, 89]. As discussed in the previous chapter in Section 6.4, the aim of such an alteration is to increase the coupling efficiency. The reasoning for such work is based upon the principal that the travel time variance through the scintillator crystal is small relative to the light output contribution to the time resolution. As we showed in Chapter 6, this is a valid assumption. In cases where there is poor coupling between the scintillator crystal and the photodetector, namely cases where optical grease cannot be used, top face alteration methods are effective [90]. However I would conclude there are two main issues with this direction of research. Firstly to accommodate higher sensitivities needed for PET, longer scintillator crystals must used. This will lead to an increase in the geometrical contribution to the time resolution. Furthermore losses will be predominantly through lateral faces. Secondly in most scenarios, including in PET, optical grease can be used. As presented in Chapter 6 we would conclude that incorporation of idealised top face alteration will lead to minimal time resolution

improvement.

New work in this field [85, 91, 92] looks at fabrication of such devices. In all three cases, light output has been seen to improve between a high refractive index media, such as LYSO, and air. No work thus far has demonstrated improvement with optical grease in place. These studies however are useful for work presented in this chapter as they discuss simulation methodology. With reference to these papers, this will be discussed in Section 7.2.3.

7.2.2 Lateral Face Alteration

Lateral face alterations look at either improving DOI information extraction [93] or increasing the light output at the top face by increased scattering [64]. In the former case the work looks into improving the spatial resolution within a bulk scintillator crystal. The latter paper looks at laser etching patterns into a lateral face of a scintillator crystal. In doing so they aim to increase reflectivity back into the scintillator crystal and thus reduce losses. The paper shows a 90.4% increase in the light output (without optical grease present). Interestingly this is the only reference found to look into this novel methodology. There is one prior reference to alteration of the lateral face in [7] on page 46 discussing Anger cameras. The schematic shown from the reference is given in figure 7.1.

Figure 7.1: Light propagating from a single position within a scintillator crystal. Diffusive layers are present at the top and bottom of the image. The top is considered to be highly reflective. The sides are considered to be highly absorbing. The photodetector is present at the bottom face. This image is taken from [7].

In this figure the 'aspect ratio', that is the ratio of the length compared to the pixel area, is reversed to that used in PET. In this case we utilise absorbing layers on the lateral (side) faces to improve spatial resolution. This is due to a much higher proportion of photons reaching the photodetector without collisions with the lateral faces. There are no known references to lateral face alterations with the aim to preferentially scatter photons towards the photodetector.

7.2.3 Proposed Designs

Ideally we wish to construct a metasurface capable of the confinement behaviours described in the previous chapter. Any such structure should work within the constraints specified by light produced within the scintillator crystal. These being

1. Generated optical photons are incoherent, broadband and unpolarised.

2. Photon emission occurs from a single point and has no preferred direction.

3. Every generated optical photon carries information.

In this chapter we will endeavour to lift some of these restrictions by calculation of the differential scattering cross section using analytical methods. We will now discuss each of these three conditions in greater detail and how they will be dealt with in this work.

The First Condition

As each photon has no phase relationship with any other, each will be treated as a plane wave source in simulation. Unpolarised light is treated in all simulations by summation of orthogonal polarisation modes for a given incident wave in the far field. In tools such as FDTD Solutions [94], broadband simulations can be performed. To reduce the number of variables, in this chapter simulations will be performed at the peak wavelength for photon emission within LYSO only — namely 420 nm. In [95] a similar method is presented showing scattering structures functioning across a wide range of wavelengths.

These studies have an additional advantage. Namely that full control of the phase of reflected light for both orthogonal polarisations has been demonstrated [95–97]. This control of the directionality will be essential in our structure's design.

The Second Condition

This condition is the most difficult to account for. This is due to the large range of wavevectors the structure needs to act upon. For LYSO the range of wave vectors of interest can be defined as

$$\vec{k} \cdot \vec{n} = \frac{2\pi}{\lambda} \hat{k} \cdot \hat{n} \tag{7.1}$$

$$\therefore k_{\min} = \frac{2\pi}{\lambda_{\max}} \cos\theta_{\max} \tag{7.2}$$

$$\therefore k_{\max} = \frac{2\pi}{\lambda_{\min}} \tag{7.3}$$

where $\vec{k}$ is the wave vector of an incoming optical photon, λ is its wavelength, $\vec{n}$ is the scintillator crystal's surface normal and $\theta_{\max}$ is the maximum angle between the surface normal and incoming photon we wish to consider. The minimum wavelength in this work will be 400 nm as this corresponds to the edge in the rapid decrease in absorption length of LYSO. The maximum wavelength as determined from figure 4.3, will be at least 500nm. As discussed in the previous chapter, utilisation of an interface layer allows us to reduce the number of photons the metasurface will interact with. Therefore the maximum angle will depend upon the refractive index mismatch between the scintillator crystal and the interface refractive index. From the previous chapter, for polar angle confinement a interface refractive index of 1.4 gives the maximum improvement. Therefore we need a critical angle of 51°. It should be noted that the incident angle of an incoming photon will have a much larger effect upon the range of wavevectors needed. Therefore in the following work we will focus on a single wavelength with multiple incident polar angles.

Secondly, most simulation tools are poorly designed to deal with multiple incoming incoherent directions. In FDTD simulations, such as [94], it is possible to simulate broadband interactions simultaneously. Simulation of unpolarised light requires two runs. Simulations of multiple incoming directions from plane wave sources, enough to fairly simulate a cone of unpolarised light quickly runs into runtime issues. This is prior to optimisations or parameter sweeps. In prior work simulations typically look at a single wavelength of a single polarisation at normal incidence. In [84] CAMFR [98] is used for these calculations. In this case normal incidence is used. In [85] the computational difficulty is acknowledged. In this paper, Rigorous Coupled Wave Analysis (RCWA) is utilised with a 2D cross section of the structure. The individual cone shape used

as the singular structure is then optimised in FDTD. This approach allows polar angles to be investigated much more thoroughly for both polarisations as RCWA in 2D is much quicker than FDTD in 3D. In [92] an unspecified FDTD method averages dipoles emitting in the x, y and z planes relative to the structure. The most promising computational method found thus far is in a thesis [99]. In this, a structure optimisation technique known as the Adjoint method is described. On page 97, a method outlining the improvement of an anti-reflection coating is described. In this the optimisation strategy looks at improving the 'worst performing mode' in each iteration. In this way, the net performance of the system can be improved iteratively.

The Third Condition

As shown in [24] ordered photon information rapidly approaches the CRLB. Furthermore the standard inverse square root behaviour with light output ties light output to the time resolution. In both cases, losses will lead to time resolution degradation. Therefore any additional losses due to the metasurface must be minimised.

High reflectance values of up to 80% have been observed with metallic scatterers [96]. Furthermore as there is no transmission through a metallic interface, composed of such scatterers, losses will be significantly reduced. A high cross section will ensure that interacting photons are scattered a minimal number of times before reaching the photodetector. If this cannot be achieved then the reflectance must be near ideal to ensure losses due to the metasurface are minimised. As long as losses are very minimal, any scattering structure with good reflectance and a useful far-field pattern should perform better than a purely diffusive wrap. This is because photons will interact with lateral faces many times before reaching the photodetector.

7.3 Calculation of the Differential Scattering Cross Section

For a single sufficiently small scatterer, with respect to the incident light's wavelength, a single electric dipole will be induced. The magnitude of the induced dipole moment with respect to the incident electric field will determine the strength of scattering into a particular solid angle. By collections of such scatterers we are able to create a phase difference between dipoles and thus tune the far-field pattern to a desired shape.

To calculate the far field pattern of an array of electric dipoles we will need to calculate the differential cross section. This is defined as

$$\frac{d\sigma}{d\Omega} = \frac{k^4}{(4\pi\epsilon_0 E_0)^2}\Big|\sum_j \left[\vec{\epsilon}^*.\vec{p}_j e^{i\vec{q}.\vec{x}_j}\right]\Big|^2 \tag{7.4}$$

where σ is the cross section, k is the wavenumber of the incoming radiation, E_0 is the amplitude of the incoming radiation, ϵ_0 is the permittivity of free space, $\vec{\epsilon}$ is the polarisation of the outgoing radiation, $\vec{p}$ is the (induced) electric dipole moment, $\vec{q}$ is the elastic scattering vector and $\vec{x}_j$ is the position of the jth scatterer [79, eqn 10.18]. For an identical series of electric dipoles the dipole term will be removed from the sum leaving

$$\frac{d\sigma}{d\Omega} = \frac{k^4}{(4\pi\epsilon_0 E_0)^2}|\vec{\epsilon}.\vec{p}|^2 F(\vec{q}) \tag{7.5}$$

where $F(\vec{q})$ is known as the structure factor. This term is discussed further in Section 7.3.1.

One of the main advantages of calculating the differential scattering cross section in this manner, is that unpolarised light can be accounted for directly. By representing unpolarised light as two orthogonal polarisations we can define

$$\therefore \frac{d\sigma_\parallel}{d\Omega} = \frac{k^4}{(4\pi\epsilon_0 E_0)^2}|-\vec{p}.\vec{n}_0 \times (\vec{n}_0 \times \vec{n})|^2 F \tag{7.6}$$

$$\therefore \frac{d\sigma_\perp}{d\Omega} = \frac{k^4}{(4\pi\epsilon_0 E_0)^2}|\vec{p}.(\vec{n}_0 \times \vec{n})|^2 F \tag{7.7}$$

$$\frac{d\sigma}{d\Omega} = \frac{d\sigma_\perp}{d\Omega} + \frac{d\sigma_\parallel}{d\Omega} \tag{7.8}$$

where $\vec{n}_0$ is the incident direction vector, $\vec{n}$ is the scattered direction vector and $\vec{k}$ is the wavevector of the incoming wave. In Appendix D.1 the derivation of the two orthogonal modes is given.

It can be seen that there are now two terms which we must determine to design the metasurface. These are the structure factor, F and the induced dipole moment, $\vec{p}$. In the next subsections we will discuss the derivation of these two terms.

7.3.1 Derivation of the Structure Factor

For the elastic scattering vector, $\vec{q} = k(\vec{n}_0 - \vec{n})$, the structure factor in two dimensions is defined as

$$F(\vec{q}) = \Big| \sum_{x_{12}} e^{i\vec{q}.\vec{x}_{12}} \Big|^2 \tag{7.9}$$

where $\vec{x}_{12}$ is the position of the (x_1, x_2) scatterer. Therefore if the positions of scatterers are known, the structure factor can be calculated. A periodic array in two dimensions can be written as

$$\vec{x}_{12} = \hat{x}(U_1 d_1 \cos\theta_1 + U_2 d_2 \cos\theta_2) + \hat{y}(U_1 d_1 \sin\theta_1 + U_2 d_2 \sin\theta_2) \tag{7.10}$$

where U_1, U_2 are integers defining each scatterer position, θ_1 and θ_2 are the angles with respect to the x axis and d_1 and d_2 are their separation distances respectively. Substituting equation 7.10 into 7.9 results in

$$F = \sum_{U_1,U_2} |\exp(ik(\vec{n}_0 - \vec{n}) \cdot (\hat{x}(U_1 d_1 \cos\theta_1 + U_2 d_2 \cos\theta_2) + \hat{y}(U_1 d_1 \sin\theta_1 + U_2 d_2 \sin\theta_2)))|^2 \tag{7.11}$$

$$F = \sum_{U_1} |\exp(iU_1 f(d_1, \theta_1))|^2 \sum_{U_2} |\exp(iU_2 f(d_2, \theta_2))|^2 \tag{7.12}$$

where $f_i = d_i(\vec{q} \cdot \hat{x} \cos\theta_i + \vec{q} \cdot \hat{y} \sin\theta_i)$. The summation can be solved analytically by

$$F = \Big| e^{if_1} \frac{1 - e^{ikN_1 f_1}}{1 - e^{if_1}} \Big|^2 \Big| e^{if_2} \frac{1 - e^{iN_2 f_2}}{1 - e^{if_2}} \Big|^2 \tag{7.13}$$

$$F = \frac{1 - \cos N_1 f_1}{1 - \cos f_1} \frac{1 - \cos N_2 f_2}{1 - \cos f_2} \tag{7.14}$$

which results in

$$F = \frac{\sin^2 \frac{N_1 f_1}{2}}{\sin^2 \frac{f_1}{2}} \frac{\sin^2 \frac{N_2 f_2}{2}}{\sin^2 \frac{f_2}{2}} \tag{7.15}$$

where N_1 and N_2 are the number of scatterers in each axis. Unless otherwise stated, this is the form of the structure factor used in this chapter. This calculation assumes no secondary effects

due to multiple scattering within the metasurface.

7.3.2 Derivation of the Induced Dipole Moment

The dipole moment $\vec{p}$ will be induced by incident light. The relationship between the incident electric field $\vec{E}_{\text{inc}}$ and the dipole moment is

$$\vec{p} = \epsilon_m \alpha \vec{E}_{\text{inc}} \tag{7.16}$$

where ϵ_m is the relative dielectric constant of the media and α is the polarisability of the scatterer. The polarisability of a sphere is defined as

$$\alpha = 4\pi a^3 \frac{\epsilon - \epsilon_m}{\epsilon + 2\epsilon_m} \tag{7.17}$$

where ϵ is the relative dielectric constant of the sphere and a is the sphere radius [79]. In this work we wish to look at more complex scatterer shapes. This is with the aim of maximising interactions with ranges of incoming directions and minimise in others. In these case the polarisability must be treated as a tensor. For spheroids the polarisability tensor has three components of the form

$$\alpha_i = 4\pi abc \frac{\epsilon_i - \epsilon_m}{3\epsilon_m + 3L_i(\epsilon_i - \epsilon_m)} \tag{7.18}$$

where i is the axis under interest, ϵ_i is the relative dielectric constant in this axis, a, b, c are the ellipsoids semiaxes and L_i is the geometry factor [100, eqn 5.32]. There are three forms the spheroid can take. These are

1. Oblate — Flattened sphere
2. Spherical — Zero eccentricity sphere
3. Prolate — Needle-like (nematic) sphere

In this work we are interested in the oblate case. This is for two reasons. Firstly this much more closely resembles the circular disks which are discussed in previous work on metasurfaces. Secondly the magnitude of the induced dipole moment will be significantly lower for high angles of incidence.

This is due to significantly reduced thickness in this axis. This is a desirable behaviour in this work as high angles photons should remain so rather than interact with the metasurface. The geometry factor for the oblate case ($a = b$) is

$$L_i = \frac{g(e)}{2e^2}\left[\frac{pi}{2} - \tan^{-1} g(e)\right] - \frac{g^2(e)}{2} \tag{7.19}$$

$$g(e) = \sqrt{\frac{1-e^2}{e^2}} \tag{7.20}$$

$$e^2 = 1 - \left(\frac{c}{a}\right)^2 \tag{7.21}$$

where e is the eccentricity of the oblate spheroid. Critically these are arranged such that the 'different' axis is aligned in z. For an eccentricity tending to zero, the geometry factor tends to $\frac{1}{3}$.

Utilising equation 7.22 and the oblate spheroid polarisability it is possible to analytically calculate the induced dipole moment. This takes the form

$$\vec{p} = \epsilon_m \alpha e^{i\vec{k}\cdot\vec{r}} e^{-i\omega t} \vec{E}_0 \tag{7.22}$$

where $\vec{r}$ is the position of the dipole, $\vec{k}$ is the wavevector, $\vec{E}_0$ is the amplitude and plane of oscillation of the incident plane electric field. More complex polarisabilities can be found numerically [101].

7.4 Proposed Metasurface Design

7.4.1 Method

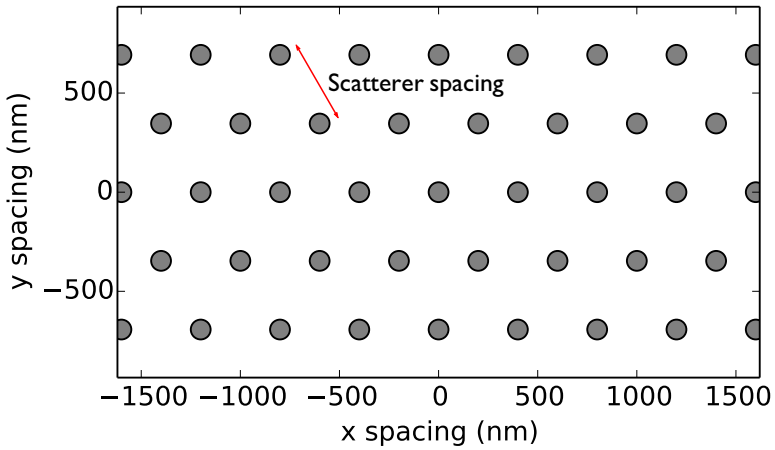

Figure 7.2: A hexagonal array of scatterers forming a metasurface. In this case the key parameter, namely the scatterer spacing, is shown.

In figure 7.2 the periodic array that will be optimised is shown. A hexagonal array is chosen as it is a closer match to the symmetry of the incoming light source. Equation 7.10 will take the form

$$\vec{x}_{12} = \frac{d}{2}[\hat{x}(U_1 + 2U_2) + \hat{y}(\sqrt{3}U_1)] \tag{7.23}$$

In this chapter we will optimise the scatterer spacing, d and hold the spheroids shape constant. This is due to our primary focus being the structure factor's influence upon the far-field pattern. Future work utilising more complex simulation, such as FDTD, can investigate the far-field behaviour of individual scatterers. In figure 7.3 the metric for the performance of a metasurface is shown.

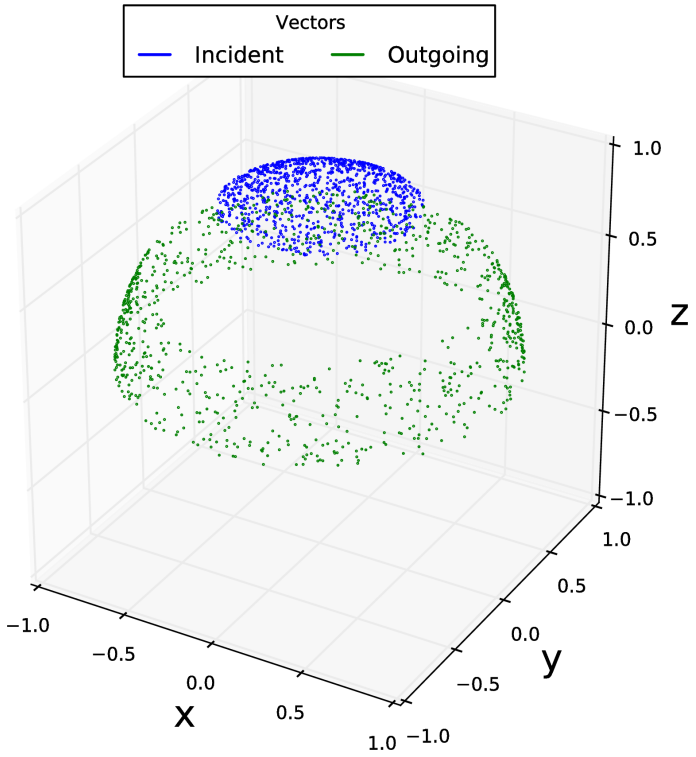

Figure 7.3: Idealised incoming and outgoing directions are shown for a polar angle confinement metasurface.

In this figure it can be seen that a cone of randomly generated incoming photons becomes a random direction in a theta confined outgoing pattern. Mathematically we can determine the performance of such a metasurface over multiple incoming directions by

$$M(\theta|\Delta\theta) = \frac{1}{M(0|\frac{\pi}{2})} \int_{\theta'=\theta}^{\theta+\Delta\theta} \frac{d\sigma}{d\Omega}(n|n_0) \cos\theta' d\theta' d\phi'$$

where M is the fraction of the far-field pattern within the desired theta range, n is the outgoing vector of interest, n_0 is the incoming vector of interest, θ is the minimum polar angle and $\Delta\theta$ is the range of polar angles acceptable.

In the next section we will utilise code[1] to produce a parameter sweep of the dipole spacings. In this initial study we will implement Aluminium oblate spheroids. This was chosen as a material as its refractive index was known, it has a plasmonic resonance close to the emission range of LYSO

[1] Available at `https://github.com/marksbrown/DipoleArray`

and its usage in other metasurfaces was evident [102]. Each scatterer will have a fixed height of 1 nm and a radius of 50 nm. These parameters are chosen as they are significantly below the wavelength of incident light. Therefore only electric dipoles will be induced. Secondly the low thickness of 1 nm is chosen to ensure low scattering cross section at high polar angles of incidence. These parameters are chosen as a first approximation of the individual scatterer shape. Further work will need to be performed to determine the optical shape, size and material. In this manner the scattering differential cross section will be predominantly controlled by the structure factor. A 1000 by 1000 hexagonal array of such spheroids is embedded within a dielectric material matching the refractive index of LYSO. This is considered sufficiently large to model an infinite array.

The performance of the metasurface should be compared to the proportion scattered into the desired polar angle range for an isotropic (no preferred direction) surface. For an isotropic emission source we can calculate the proportion of light expected into a given range of angles by integration over solid angle. The fraction scattered in an angle θ or higher would be given by

$$\frac{f}{f_0} = \cos\theta \tag{7.24}$$

where $\frac{f}{f_0}$ is the fraction of light from an isotropic source emitted into angles greater than θ and less than $\frac{\pi}{2}$[2]. For instance, for a minimum angle of 80°, we would expect to see 17%. Therefore any value from a metasurface greater than this indicates it is possible to beneficially alter light greater than that of an isotropic source (essentially depolishing the lateral faces). For multiple incoming directions this is a useful comparison to make.

7.4.2 Normal Incidence Results

To begin we look at incoming light at normal incidence only. We will look at spacings from 200 to 600 nm in 5 nm increments. This range is chosen as it covers the emission region of LYSO with good clearance each side. The results of these simulations are given below in figure 7.4.

[2]Integration of $d\Omega = \sin\theta' d\theta' d\phi'$ for $\{\phi', 0, 2\pi\}, \{\theta', \theta, \frac{\pi}{2}\}$.

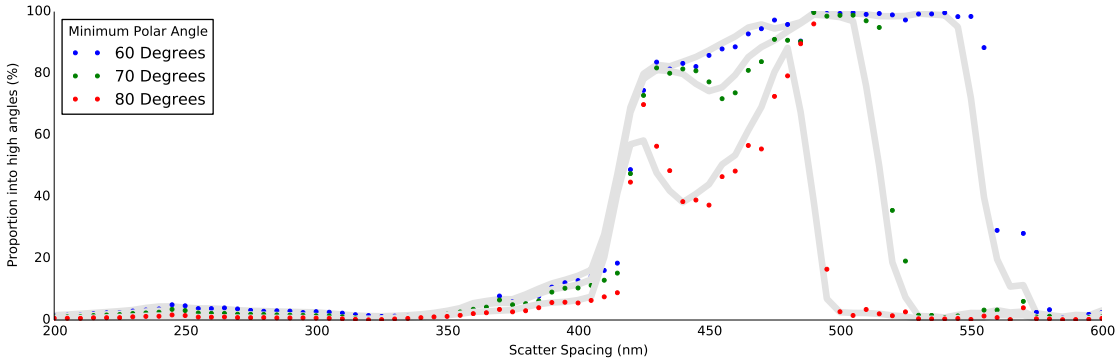

Figure 7.4: Calculation of the proportion of light scattered into polar confinement of 60° to 90° shown in blue, 70° to 90° shown in green and 80° to 90° shown in red with scatterer spacing in nanometres. The grey lines are a moving average for each case. In this case incident light comes from normal incidence only.

In the above figure it is seen that it is possible to scatter nearly all light into a chosen polar angle confinement. For increasing polar angle confinement in the outgoing direction, the narrower the region corresponding to 100% becomes. In figure 7.5 the scattering cross section for varying scatterer spacing is shown.

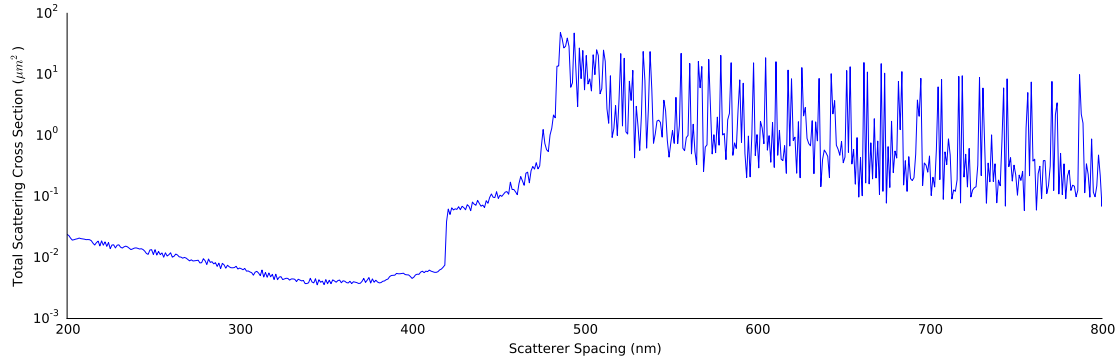

Figure 7.5: Calculation of the scattering cross section for varying scatterer spacing. In this case incident light comes from normal incidence only.

In this case it is clear that the scattering cross section is insignificant below a scatterer spacing of approximately 500 nm. Secondly there is a clear edge at 420 nm. This matches the incident light wavelength. The low cross section below this would indicate there is poor coupling between the metasurface and light at this wavelength. We would therefore see a scatterer spacing of 500 nm would be a good starting position for further optimisation of the metasurface.

7.4.3 Isotropic Source Results

We begin by expanding the previous model to many incoming directions. This is modelled by simulating a range of incident polar angles and weighting the results by a cosine factor to match the distribution shown in figure 6.19. In figure 7.6 the result of this is shown.

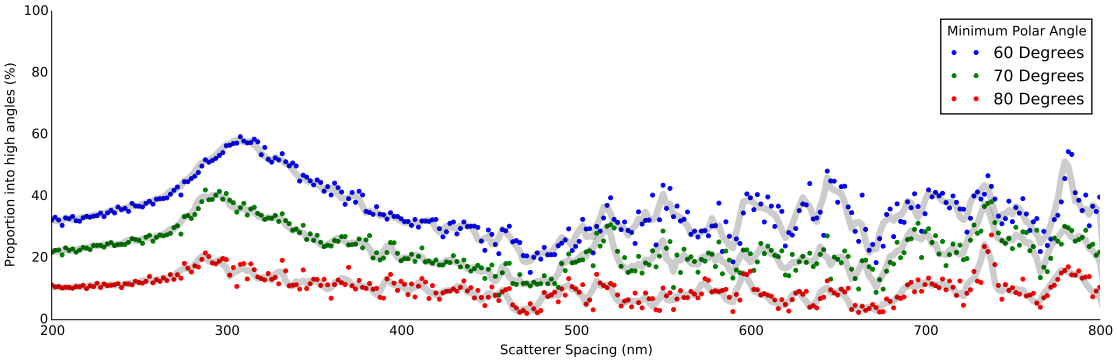

Figure 7.6: Calculation of the proportion of light scattered into polar angle confinement of 60° to 90° shown in blue, 70° to 90° shown in green and 80° to 90° shown in red. In this case incident light comes from an isotropic source.

From this figure we can see several things. Firstly for good confinement, namely between 80 and 90 degrees, only 10% of incident photons will be scattered into the desired direction. This is lower than the proportion stated in equation 7.24. Despite this if there are no ohmic losses, and the number of collisions with the lateral faces is high, then over many such collisions a good proportion of light will be preferentially scattered into the preferred confinement. This is due to individual photons interacting with the lateral faces multiple times on their propagation to the photodetector. Secondly the best performance is seen about 300 nm. The inverse cosine of the incident wavelength and the scatterer spacing $\frac{300}{420}$ comes out to 45°. This strongly indicates that the scatterer spacing is linked to a mean incident wavenumber. Thirdly the variation in performance is seen to be lower than in the normal incidence case. Given the broadband nature of incoming light it is unsurprising that the metasurface shows poorer performance.

To determine the potential effectiveness of such structures with the inclusion of an interface layer, we limit the isotropic incoming source to polar angle regions. In figure 7.7 incident polar angles up to 30 degrees are considered. As discussed previously, this corresponds to an air gap between the scintillator crystal and the metasurface.

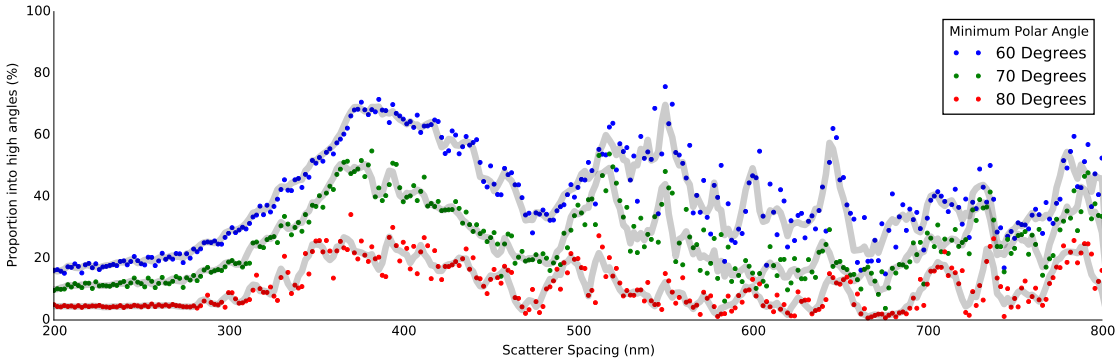

Figure 7.7: Calculation of the proportion of light scattered into polar angle confinement of 60° to 90° shown in blue, 70° to 90° shown in green and 80° to 90° shown in red. In this case incident light comes from between 0 and 30 degrees. This corresponds to a critical angle between LYSO and air.

In the above figure it can be seen that the proportion of light scattered into the desired confinement is improved compared to the isotropic case. In this the peak performance is seen near 380 nm. For the 10 degrees of polar angle confinement, shown in red, 40% of light is scattered. This is over double that expected from purely an isotropic source.

More realistically we can look at an interface layer corresponding to a refractive index of 1.4. In the previous chapter this was seen to have the optimal performance improvement for polar angle confinement. In figure 7.8 incident angles up to 51 degrees corresponding to this interface layer.

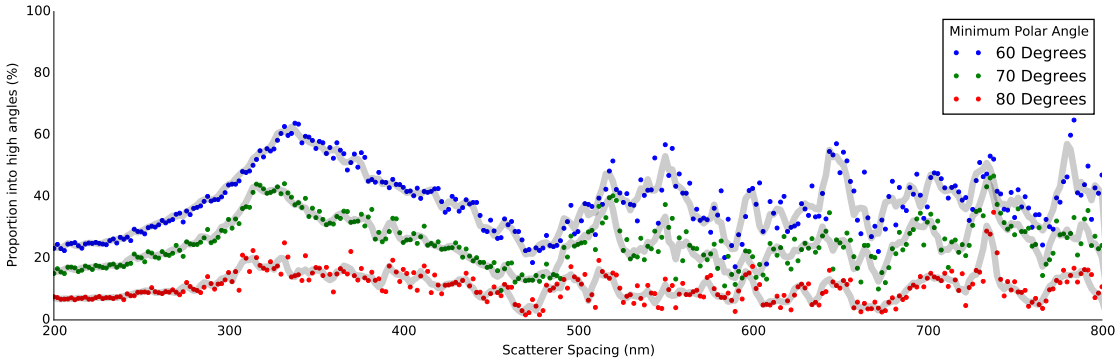

Figure 7.8: Calculation of the proportion of light scattered into polar angle confinement of 60° to 90° shown in blue, 70° to 90° shown in green and 80° to 90° shown in red. In this case incident light comes from between LYSO and a refractive index of 1.4. This corresponds to the optimal interface layer refractive index as discussed in the previous chapter.

The above shows a similar shape and performance to that of figure 7.7. In this case the optimal performance at 400 nm has 20% scattered into the desired angular range. This is comparable to the isotropic scattering case value of 17%. The implications of this result will be discussed fully in Section 7.5.1.

In figure 7.9 the scattering cross section for the optimal interface layer cases are shown with varying scatterer spacing below in figure 7.9.

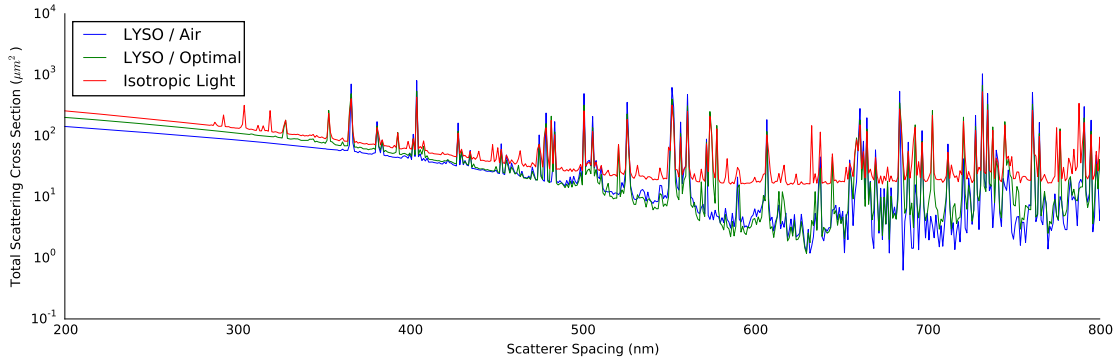

Figure 7.9: Calculation of the scattering cross section for varying scatterer spacing in nanometres. In this case incident light comes from an isotropic source, a segment cone of an isotropic source defined by the LYSO/air boundary and the same between LYSO and n=1.4.

In this case the scattering cross section performed is much more uniform across the range of scatterer spacing. This implies variation due to differences in incident direction are evened out. The overall performance is good compared to normal incidence. Further study (and improvement) of the scattering cross section will require additional work.

7.5 Discussion

7.5.1 Work Completed

In this chapter we have presented a method for simulation and optimisation of a metasurface when many incident directions are an essential part of the design. This method was demonstrated by looking at the performance of a polar angle confinement design. Most simulation tools are ill-equipped to manage multiple incoming directions as is necessity in this work. Furthermore most photonics look at either coherent light sources, or a much lower range of wavevectors.

To overcome these obstacles we have written software to calculate the scattering differential cross section. The resulting performance is quantified using a confinement metric. The hexagonal array of oblate spheroids proposed in this chapter would allow preferential scattering into high polar angles of a wide range of incident photons. However there are several assumptions underlying this approach. Firstly scatterers must be small enough to induce only electric dipoles. There must not be an 'inter-scatterer' interactions. Crucially the work presented thus far does not include the effect of the boundary between the scintillator crystal and an interface layer. Nor does it include any reflecting layer beyond this. We assume that severely oblate spheroids, namely those with a thickness of 1 nm in this work, are approximately disks. Finally we assume no losses thus far, despite using metallic scatterers.

The results presented in this chapter do not show significant improvement over a comparable isotropic case. This is due to the similarity in the proportions scattered in the polar angle confinement and the isotropic case. Furthermore given our polar angle confinement result predicting minimal improvement, if any, over the isotropic scattering case it would be a poor choice to fabrication. This design was investigated primarily due to its simplicity. Furthermore the tools written will work well for more complex designs, such as azimuthal angle confinement. In short — the final result might not be promising but the technique is.

7.5.2 Future Research

Given the unique nature of the photonics requires for scintillator detectors I would suggest several methods going forwards. Firstly Losses must be exceedingly minimal. Throughout this thesis, and in prior work, it has been shown that scintillator detector performance is sensitive the number of optical photons detected. Any reduction in this number must be offset by significant changes to the light transport PDF. There is recent work which utilises dielectric instead of metal in nano-scaled structures [103, 104]. Whilst utilising dielectrics will reduce the scattering cross section, it will also allow near-perfect reflectance values.

In [95] combinations of different scatterers are repeated to produce what is referred to as a supercell. I would suggest investigation of supercells for optimisation of scatterer placement. In figure 7.10 this idea is applied to the metasurface in this work.

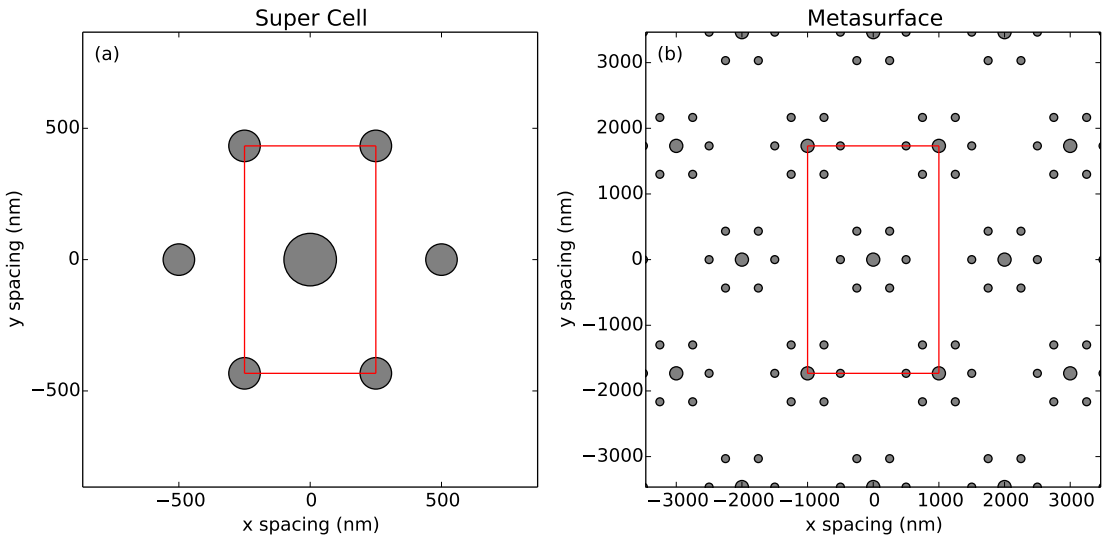

Figure 7.10: Proposed design for improving control over metasurface design.

In this figure it can be seen that combinations of different scatterers can be arranged into a hexagonal periodic array. In this manner it is possible to tune different parameters of the supercell to different requirements. There are several examples of successful application of supercells to various examples [88, 95, 97].

Using such supercells it would be interesting to explore whether 'ϕ exclusion' regions could be defined. As discussed in the previous chapter, even minimal reductions in the range of ϕ away from the photodetector can lead to significant improvements in the time resolution. Future work should look into the potential of improving both θ and ϕ confinement.

Next to be completed would be a rigorous study of scatterer design using computer simulation, such as FDTD. Once the scatterer arrangement is completed the supercell can be designed In figure 7.11 a proposed design for this is shown.

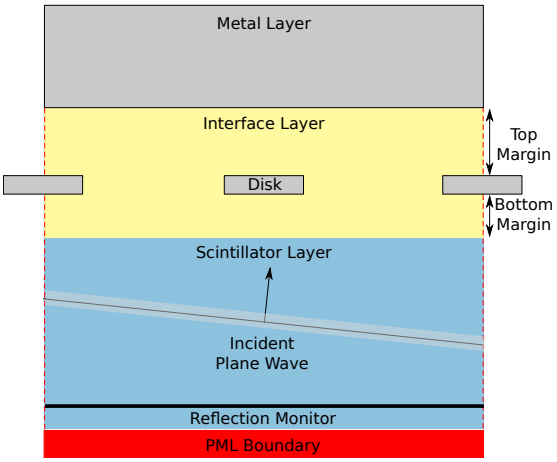

Figure 7.11: Cross section of an FDTD simulation including important details labelled.

In this figure there are three things to be optimised. These are the top margin, the bottom margin and the shape of each scatterer. As discussed earlier in the chapter, the Adjoint method can be used to optimise a design despite many free parameters. In this case this would allow much finer control over each scatterers shape. This would even allow a selection of incoming directions to be modelled during the optimisation.

7.5.3 Potential Other Methods

Given the high number of free parameters in the incoming light it may make more sense to look at techniques that do not rely on coherent light to function. Such methods include patterning, laser etching [64], graded refractive index (known as GRIN) or material matching. Patterning would look at larger structures on the lateral faces. Patterns such as chevrons to reduce the portion of light scattered backwards might be an effective technique to investigate further. Laser etching looks at introducing tuned roughness on the surface and the resulting effect on light output and timing performance. In [64] this has been investigated demonstrating improved light output. Other work has looked into the contribution of roughness and found it can improve the timing performance [105]. The final, and perhaps simplest method, would be to search for diffusive materials with a high reflectivity and measure their reflection profile using a reflection goniophotometer. If the reflection profile has some element of azimuthal confinement this would lead to an improvement over traditional diffusive materials such as PTFE.

Chapter 8

Conclusion

8.1 Work Completed in this Thesis

In Chapter 3 radiation measurements, published in PLOS ONE in 2014 [8], are presented. New work demonstrates no relationship between interaction position and the timing performance of the scintillator detector. Furthermore it was shown that the quality of the wrap about the scintillator crystal will the timing performance. Measurements of the timing performance degradation with scintillator crystal length are also presented. The implications of these results are discussed further in Section 3.6.

In Chapter 4 optical measurements of LYSO and PTFE are presented. Two sets of new measurements are presented in this work. Firstly, TCSPC measurements look at the alteration to light propagation through the scintillator crystal directly by observing changes to the lifetime data of LYSO. TRES measurements on LYSO show no discernible change in the lifetime data with wavelength within experimental error. Next it was shown that the surface roughness of a single lateral face will increase the light output by a factor of two. However no change in the lifedata data was visible. When excitation position is varied, as was done in section 4.2.5, a difference in lifetime data was visible. Furthermore in the 'near' position the light output was third higher. These results are discussed further in section 4.4.1.

Next reflection goniophotometer measurements of LYSO and PTFE were presented. In LYSO,

the difference on and off axis for reflection from a polished or roughened surface is shown. It was seen that the roughening of a lateral face of a LYSO scintillator crystal leads to scattering into high polar angles. Furthermore light output is seen to increase with roughening for normal incidence cases. The PTFE results show the predominantly Lambertian behaviour expected for the diffusive material regardless of incident direction. The implications of these results are discussed in 4.4.2.

The results collected from both experimental chapters are used in Chapter 5 to validate a new statistical model. The model, based on maximum likelihood statistics, incorporates a light propagation contribution which we refer to as the light transport. Light transport in the model is used to predict the effect of light propagation through the scintillator crystal upon the timing performance of the scintillator detector. The light transport is modelled both analytically and by simulation. In the former case the degradation in the timing performance with scintillator crystal length is demonstrated. In latter we would conclude that near-specular contributions converge to the same result as purely specular descriptions. An additional result looked at asymmetry in the photodetector contribution. It was shown that a positive skewness of 0.8, such as one estimated from a real SER, will result in a CRLB CTR 20% lower than we expect for a symmetric photodetector distribution. Further discussion of the Fisher Information model is found in section 5.8.

In Chapter 6 the model is used to look at more complex surface and geometrical effects. The incorporation of wrapping into the model, via the simulation, is shown to explain the scintillator crystal length and quality of wrap contributions to the timing performance. Following this two alterations to the geometry, raised edge and trapezium geometries, are shown. Both geometries can improve the timing performance as well as the sensitivity of the overall PET scanner.

Next the surface reflection model is altered to incorporate polar and azimuthal angular confinement. This is explored to determine potential scattering structure designs which would improve the timing performance. It was shown that minimal improvement is found for polar angle confinement alone, however incorporation of azimuthal angle confinement can significantly improve the timing performance. Azimuthal angle confinement was shown to render the light transport contribution to the time resolution negligible compared to the photodetector contribution. In section 6.5.4 one optimal reflection model is shown. In this, a CRLB CTR of 103 ps, for a $2 \times 2 \times 20$ mm^3 LYSO scintillator is possible for minimal azimuthal angle confinement if the model is applied to all lateral (and rear) faces. In section 6.6 the discussion for this chapter is presented.

In the last chapter, Chapter 7 a method for design and optimisation of metasurfaces using the scattering differential cross section is presented. To demonstrate this method of calculating the scattering differential cross section a polar angle confinement structure is designed.

8.2 Discussion of Work Presented

In this thesis we have endeavoured to understand light and its role in scintillator detectors. In this manner we wish to determine not only a logical set of rules that describe the system, but also a model which would allow potential methods for improvement to be explored. Construction and design of new scintillator detectors is difficult and expensive. This is especially compounded by unintended changes in one part of a complex system, such as PET, altering the performance in another. At the beginning of this PhD, our initial aim was to implement some method of coupling light out of the lateral faces of the scintillator crystal into waveguides. These flat thin waveguides would propagate light to ends of the scintillator crystal and into the photodetectors. Critically the reasons for why this would improve, or indeed degrade, the performance of the scintillator detector was unknown. Prior work on the incorporation of photonic crystals at the top face had recently demonstrated no clear improvement in the timing performance or light output, when grease was present. Indeed no improvement over optical grease has yet to be seen. From this, I determined that I had the problem backwards. It was not to determine what photonics would improve the timing performance, but if photonics could improve the timing performance. It is this question which I have aimed to answer in this work.

8.3 Criticisms of the work performed

There are several assumptions underlying the work in this thesis. In this section I will list the key points and my justifications therein. Firstly we have made no attempt to specify an unbiased estimator for calculation of the CRLB. It is known that discriminators are not unbiased [24,106] and therefore will contribute to the timing degradation of the overall scintillator detector. We assume that the contribution of this effect is negligible and that there is minimal distinction between a well calibrated discriminator and the result from an ideal unbiased estimator.

Secondly the results presented in Chapter 6 rely on arbitrary phase shifts with no concern for what is physically allowed by laws such as Etendue in optics. Whilst such rules do place limitations on what is allowed by optics we would make two assumptions. Firstly alteration of wavelength or minor loss of energy is allowed for some alteration of the confinement of light. Secondly, the degree of confinement required to improve the timing performance is minimal (see figure 6.30). Thirdly and finally the results shown in the chapter are to demonstrate the effect of the reflection model and geometry. These results present possible avenues for further work, some of which are discussed in the next section.

8.4 Proposed Studies

Going forwards there are several promising lines of enquiry that should be investigated. Firstly the DOI measurements should be repeated with an automated stage. Alteration by hand could alter the electronic collimation and introduce a systematic bias. Furthermore, with a stage, many more measurements per scintillator crystal could be found. Ultimately this would lead to a lower experimental error and place a further bound on the change in the CTR with interaction position.

Secondly a simple study which could be performed, would be multiple attempts at wrapping a scintillator crystal and measuring the resultant timing performance. In this work, this was attempted at most three times (see table 3.4). With multiple attempts and a more methodical approach, the size and variation in the 'wrapping degradation' contribution could be surmised. In Chapter 6 this variation is claimed to be due to a mismatch in the interface between the wrapping and the scintillator crystal. It would be interesting to see to what effect this is true. For instance, painting the scintillator crystals with varying diffusive paints of different refractive indices would give an indication of this effect. I would also recommend a study into metallic coatings of the lateral faces. A simple test, such application of gold leaf, would give valuable data with respect to changes in the CTR and light output.

For the optical results there are many more studies potentially possible. For TCSPC, the biggest issue is ensuring a small region of high confinement. Repeating the measurements with a lower wavelength, sub-400 nm, pulsed laser would be an excellent start. Furthermore utilising larger scintillator crystals, or materials which show strong absorption in useful wavelength ranges,

would allow the near/far results to be explored further. Ideally timing measurements using x-rays (or higher energies) would allow the effect of radioluminescence to be incorporated into these results.

The imaging sphere results are truncated in some respects due to the incalcitrance of the machine's software! Whilst each measurement may take minutes in theory, in practice each measurement requires several calibration steps. Breakdowns, faults and conflicting results led me to distrust a great many of the images resulting from the apparatus. Going forwards, the machine itself is exceedingly powerful and will offer detailed results of material properties that cannot be obtained in any other way easily. Work presented in [54] shows incorporation of BGO surface reflection measurements into Look Up Table (LUT) used in Geant4 [107]. This allows BRDF measurement to be directly incorporated into simulations. No work has yet added new look up tables to Geant4. Measurements performed using the imaging sphere would be able to produce new such tables. These would be exceedingly important in not only scintillator detector research but also PET. GATE [108] is a radiology simulation tool based on Geant4. As previously mentioned LYSO is the chosen material of new generation scintillator detectors. More information about these would lead to more realistic simulations and hopefully designs for next generation PET scanners.

The maximum-likelihood model presented currently does not incorporate bulk or surface losses. These contributions must be explored to determine if they are a larger effect than would be expected from the inverse square root behaviour shown in equation 5.8. Another addition would be looking at incorporation of multiple scintillator crystals or photodetectors. This would allow bulk scintillator detectors to be investigated further.

Finally as to the scattering structures. The software written should be able to determine if azimuthal angle confinement is possible with metasurfaces. If so, an optimal arrangement of scatterers should be determined. From this, rigorous electromagnetic simulations looking at a wide range of incident angles should look at design of the scatterer itself. I believe the most promising line of work will look at incorporation of techniques to count the negatives of increasing the scintillator crystal length. Sensitivity for whole body PET images must be improved. Longer scintillator crystals are a good first step in this aim. This can be accomplished by incorporation of additional photodetectors, allowing DOI information to be determined. Or indeed by inclusion of azimuthal angle confinement at the lateral faces of the scintillator crystal.

8.5 Summary

In this thesis new experimental results performed at UCL and CERN are used to validate an extended Fisher Information model. The new model incorporates light transport, allowing predictions of various effects upon the scintillator detector performance. Alteration of the geometry or surface reflection model is shown to improve the time resolution. This thesis concludes with a description of one method to design altered surface reflection structures, known as metasurfaces.

Appendix A

Direct Measurement

A.1 Background

A.1.1 Measurement of the Time Resolution

Idealised Measurement

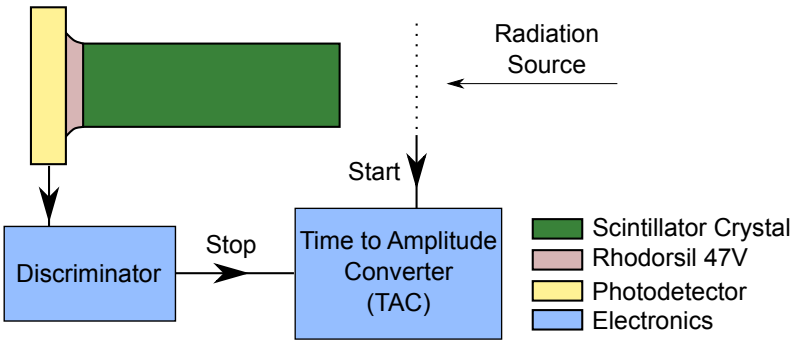

Figure A.1: Schematic of an apparatus to measure the time resolution of a scintillator detector. A quantum of radiation passing the dotted line will produce a perfect start signal. The subsequent interaction of the radiation with the scintillator crystal will be detected by the photodetector. The discriminator will produce a logical pulse when a sufficient signal from the photodetector reaches it. The resulting difference in time between the start and stop signal is fed into a computer and histogrammed to produce a relative time delay distribution. An example in theory is shown in figure A.2.

The determination of the uncertainty in the true arrival time of an ionising particle can be accomplished using the apparatus shown in figure A.1. When a single high-energy particle passes through the dotted line a perfect start signal is sent to the time-to-amplitude converter (Time-to-Amplitude Convertor (TAC)). If the particle interacts with the scintillator detector a pulse of optical photons will be produced. This signal, assuming it meets the criteria of the discriminator, will produce a logical pulse which is fed into the TAC as the stop signal. The TAC, assuming the time difference between the two pulses is sufficiently low, will produce an output pulse with charge proportional to the difference in arrival time between associated start and stop signals. Collections of many such events will produce a list of the relative delay in arrival time between start and stop signals. For a perfect scintillator detector we would expect a fixed difference in time due to the physical difference in travel time between the signals, with zero variance.

In reality the apparatus shown in figure A.1 would generate the curve seen in figure A.2.

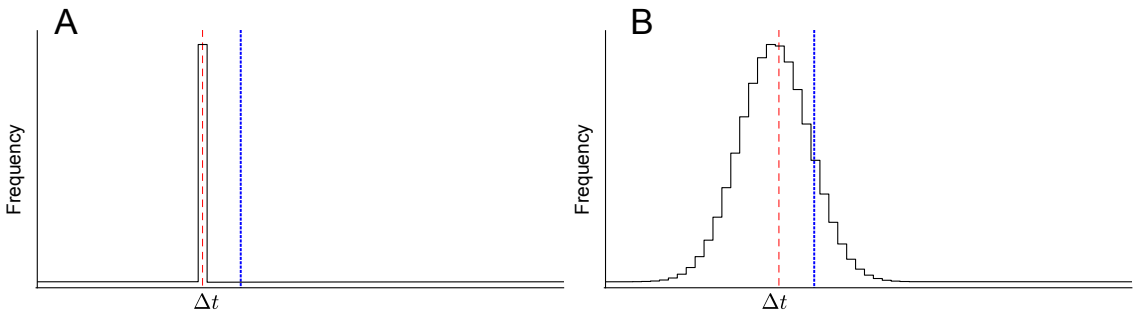

Figure A.2: Difference in arrival time between start and stop signals histogram for apparatus shown in figure A.1. In A we see the ideal performance where we see no variance in the relative arrival time. In B we see a Gaussian distribution centred on the mean difference in arrival time. These will be referred to as the delay peak and the delay peak centroid respectively. The standard deviation of this delay peak is the time resolution of the scintillator detector. The blue dotted line shows the true difference in time in the two paths to the TAC. The red dashed line shows the mean difference between the start and stop signals. The difference between the two vertical lines is the systematic error of the scintillator detector.

In figure A.2 we see two key pieces of information. Firstly we note that the standard deviation of the Gaussian distribution (the delay peak) is known as the time resolution. Secondly a systematic error introduced by the scintillator detector will not be explicitly visible. On the figure a blue dotted line indicates the true arrival time of a particle at the scintillator detector. The difference between this and the mean of the Gaussian distribution, indicated by the red dashed line, is

the mean systematic time error of the scintillator detector. The ideal timing performance of a scintillator detector would possess zero statistical and systematic error.

Measurements in Reality

In the idealised apparatus we have made the assumption that the variance in time between a particle passing through the dotted line of figure A.1 and a signal being generated is effectively zero in comparison to the variation introduced by the scintillator detector. This assumption will only hold true where the uncertainty in the start signal is far lower than that of the stop. Two such methods where this assumption holds are Time Correlated Single Photon Counting (TCSPC) and the Delayed Coincidence method.

To measure the time resolution using the apparatus previous discussed would require a pulsed gamma ray source. To overcome this limitation we typically measure the time resolution of two identical scintillator detectors, simultaneously. This is accomplished by detection of gamma-gamma correlation events generated by Sodium-22.

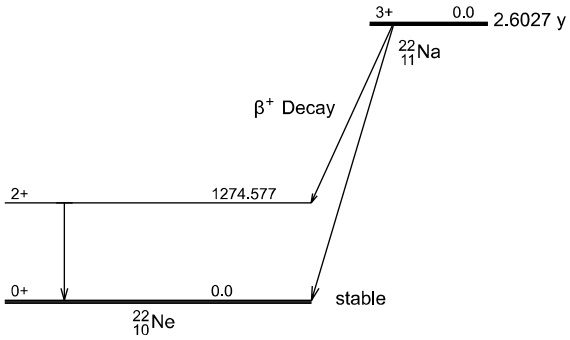

Figure A.3: Sodium-22 (Na22) emits a positron (an anti-electron) causing the creation of Neon-22 in an excited nuclei state. This decays to the ground state by the emission of a 1.2MeV gamma ray photon. The positron will subsequently annihilate with an electron causing the creation of a $\gamma\gamma$ pair travelling in opposite directions due to momentum conservation.

In figure A.3 the decay spectrum of Sodium-22 is shown. Whilst there is an angular relationship between the emitted positron and 1 MeV gamma due to momentum conservation, there is no angular relationship between the 1MeV gamma and the 0.511 MeV gamma ray photon pair. However due to the rapid decay time of the Ne22 excited state the three gamma-ray photons will be correlated in time. For most purposes the higher energy gamma ray photon is ignored.

By placing a positron-emitting source, like Sodium-22, half way between two identical scintillator detectors we can determine two pieces of information. Firstly the full-width-half-maximum (FWHM) of the measured Gaussian distribution is known as the coincidence time resolution, or CTR. Secondly the centroid of our data, the mean time delay between the two scintillator detectors should be close to zero for two identical scintillator detectors. Thus giving us a measure of the systematic error. The Gaussian distribution produced in a convolution of two Gaussian distributions describing the individual scintillator detector's relative timing delay.

A.2 Light Output Measurements

A.2.1 Overview

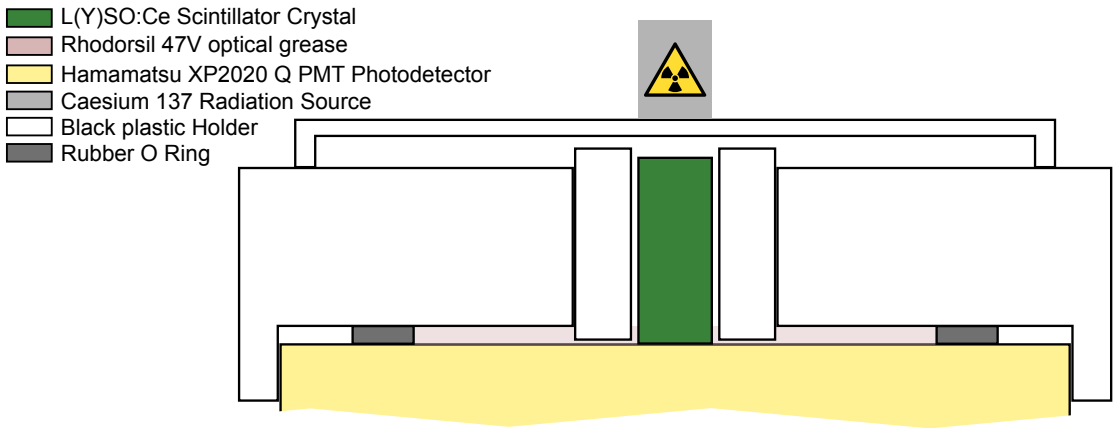

Figure A.4: A cross-section of the cylindrically-shaped light output apparatus. On top of a Photonis XP 2020 Q photomultiplier tube [17], shown in yellow, sits an opaque black plastic holder. Within this sits the scintillator crystal sample centred in the optimal position over the photomultiplier glass window. Directly above the scintillator crystal Cs-137 emitting 662 keV gamma ray photons.

In this experiment a calibrated Photonis XP2020 Q photomultiplier tube (PMT) has been used to estimate the light output. The light output is the number of photons detected per event per MeV. This is accomplished by determining the location of a known photopeak within the calibrated energy spectra of the Photomultiplier Tube (PMT). Due to the excellent linearity offered by the PMT, and the stability of measured properties such as gain, variation in the light output due to external factors such as the wrapping and optical grease may be determined. This experiment is

useful in addition to previous measurements as PMTs demonstrate excellent linearity with energy and stability with temperature in comparison to SiPMs. Both properties lead to more reliable estimates of the number of photons detected. As discussed in chapter 5, the time resolution is directly influenced by the number of photons detected. In these measurements we wish to determine the contribution of the the wrapping and optical grease upon the light output. Two optical greases, with refractive indices 1.4 and 1.6, from Cargille Laboratories were used with two Proteus $2 \times 2 \times 5$ mm^3 LYSO:Ce scintillator crystals.

A.2.2 Experimental Method

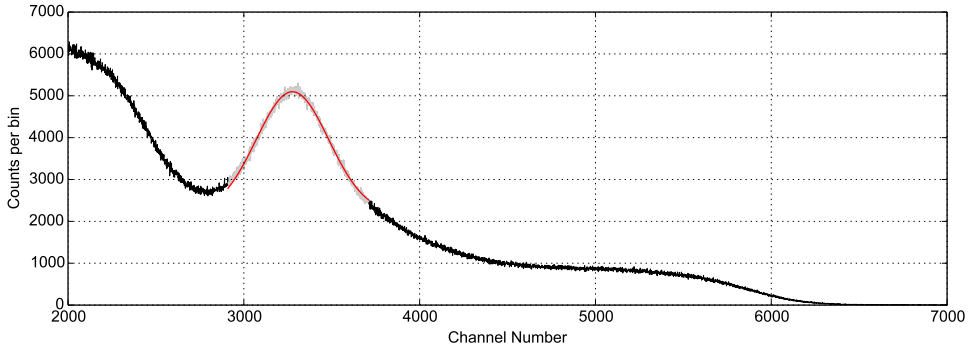

Figure A.5: A typical energy spectra measured for a Proteus LYSO:Ce scintillator crystal. The photopeak region, show in light grey is fitted to using a scaled Gaussian, shown in red to determine the photopeak location and scale parameters. These correspond to the light output and the uncertainty in the measurement respectively. The measurement shown uses a wrapped 5 mm scintillator crystal with an optical grease with refractive index of 1.4 and an attenuation of 15dB.

In figure A.4 a cross section of the cylindrical light output apparatus is shown. In this a rubber O ring sits upon the PMT glass window (shown in yellow) to prevent seepage of optical grease, shown in pink. A top this sits a two part opaque black plastic holder. This serves two purposes. Firstly to prevent light from scintillator crystal faces not in contact with the PMT from being detected. Secondly the holder will centre the scintillator crystal upon the PMT glass window. As the quantum efficiency can vary across the glass window, holding centred will negate this as a source of error. Above the scintillator crystal, shown in green, sits a black plastic cap with an Caesium 137 662 keV γ source placed upon it. The PMT is connected to an amplifier and analogue-to-digital convertor (ADC) connected to a PC. The incident charge of every event falling

within the range of the ADC, tuned by selection of attenuators prior to amplification, is recorded on the PC.

Using the photopeak's location (ch), the photoelectron and light output, N_{Phe} and N_{Ph} respectively, can be calculated using

$$N_{\mathrm{Phe}} = \frac{q_{\mathrm{ch}}\,\mathrm{ch}\,10^{\frac{dB}{10}}}{q_e G} \tag{A.1}$$

$$N_{\mathrm{ph}} = q_{\mathrm{eff}} N_{\mathrm{Phe}} \tag{A.2}$$

where (with default values in brackets) q_{ch} is the charge per channel of the ADC (160fC); ch is the fitted photopeak centroid position; dB is the attenuation applied to the PMT before arriving at the ADC; q_e is the charge of an electron (1.602×10^{-19}C); G is the gain of the PMT (1.2×10^7)[1] and q_{eff} is the quantum efficiency of the PMT for the LYSO emission (0.22). As the energy of the Caesium 137 photopeak (662 keV) is known we can now define the light output, that is the number of photons detected per MeV as

$$\mathrm{LY} = \frac{N_{\mathrm{ph}}}{E_\gamma} \tag{A.3}$$

where E_γ is the energy of the photopeak in MeV (0.662 MeV). The error in the light yield is calculated from the standard deviation in the photopeak.

[1] A known sample is recorded prior to every measurement. If the calculated light output of the sample is seen to change, the gain is scaled appropriately to adjust for the alteration in the PMT's performance. This was found not to be required in the measurements presented in this chapter.

A.2.3 Light Output Results

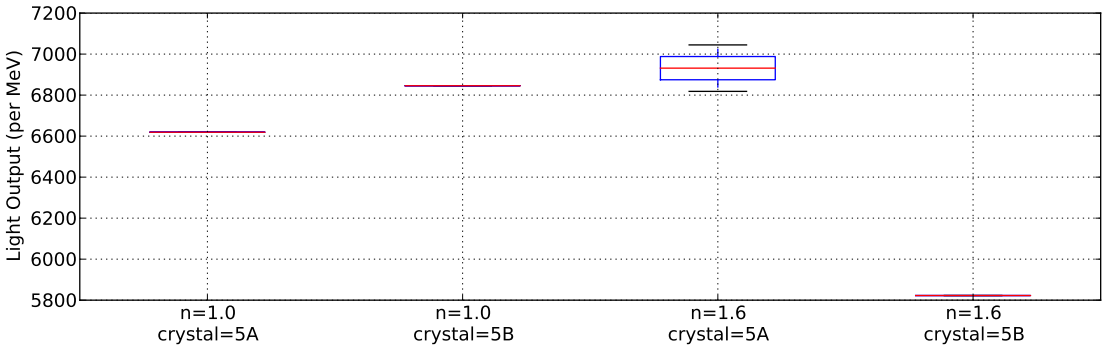

Figure A.6: Boxplots of light output results grouped by scintillator crystal and optical grease for the unwrapped configuration.

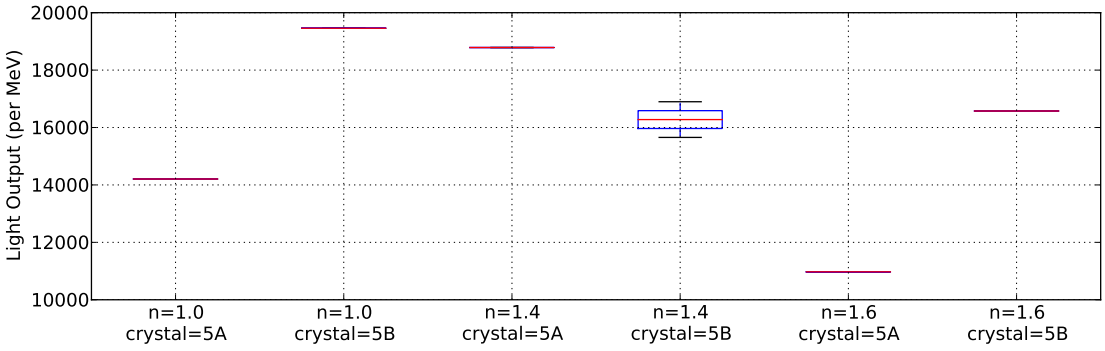

Figure A.7: Boxplots of light output results grouped by scintillator crystal and optical grease for the wrapped configuration.

In figures A.6 and A.7 boxplots of the light output (per MeV) grouped by optical grease and scintillator crystal are given for unwrapped and wrapped measurements respectively. In these plots only crystals standing vertically upon the PMT (the top orientation) are given. In table A.1 results for the 5A and 5B scintillator crystals are given. Also shown are two optical greases with refractive indices 1.4 and 1.6. Those listed as 'None' use no optical grease.

Table A.1: Light output (LY) per MeV measurements performed using Photonis XP2020 Q PMT.

Scintillator Crystal	Configuration	Orientation	Optical Grease n	LY (per MeV)
5A	unwrapped	top	None	6620±20
5B	unwrapped	top	None	6850±30
5B	unwrapped	top	1.6	5820±20
5A	unwrapped	top	1.6	6820±30
5A	unwrapped	top	1.6	7040±50
5B	unwrapped	side	1.6	14520±10
5B	unwrapped	side	1.6	20060±20
5A	wrapped	top	None	14210±40
5B	wrapped	top	None	19460±90
5A	wrapped	top	1.4	13710±760
5A	wrapped	top	1.4	14190±130
5B	wrapped	top	1.4	15660±80
5B	wrapped	top	1.4	16900±20
5A	wrapped	top	1.4	18790±60
5A	wrapped	top	1.6	10810±320
5A	wrapped	top	1.6	10970±20
5B	wrapped	top	1.6	16580±30
5B	wrapped	top	1.6	16640±150

Firstly we note that the inclusion of PTFE tape wrapping causes the largest change to the light output. In the case of the top orientation measurements, we take the mean across the unwrapped and wrapped measurements, irrespective of optical grease. These give values of 6630 ± 13 per MeV for the unwrapped scintillator crystals compared to 16079 ± 21 per MeV for the wrapped. This is an increase in the light output by a factor of 2.4. Secondly all measurements show no positive effect due to the inclusion of optical grease. Two possible explanations are that the layer of fluid being too thick; thus attenuating the signal reaching the PMT. Alternatively the scintillator crystal is coupling to the photodetector face sufficiently well without the additional layer; such that any benefit of inclusion of optical grease is negligible. Thirdly we notice a clear increase in the light output for the side orientation of the scintillator crystal compared to the top orientation. In this case the area in contact with the PMT increases from 4 mm^2 to 20 mm^2 between the top and side orientations. We see an increase in the light output of between 2.5 and 3 in this case.

A.2.4 Light Output Discussion

Our results show a clear increase in the light output with the inclusion of wrapping about the scintillator crystal. The ratio between the two configurations' light output is in good agreement with previous measurements given in [22]. In this case the light output increases with a ratio of 46:100 (see table VI) between the unwrapped and wrapped configurations. This is an increase of 2.2; in good agreement with the ratio of 2.3 seen in our own measurements. No clear result was seen from the optical grease measurements. This (lack of) result is in agreement with [109].

Appendix B

Indirect Measurement

B.1 Reflection Goniophotometer Measurement Procedure

B.1.1 Preparations

These steps must be followed to ensure the Imaging Sphere is ready for operation.

- Pull red stop button and press green button to start - A clunk should be heard.
- Switch on light source and monochromator, plug in camera.
- Ensure all three USB cables are plugged into the laptop before switching on. See above image.
- Switch on laptop and login '9.08 lab' with password 'radiantzemax'.
- Turn on IS-SA tool. If software is working there will be no errors.
- Create new measurement file in software for EACH samples measurement.

B.1.2 Calibration of Imaging Sphere

The calibration must be performed daily or whenever the aperture/fibre optic is moved. Each calibration is only valid for the angular and wavelength values given. Choose 'bright spot', 'auto-exposure' and 'clear' filter for calibration stage. Choose an aperture - if your sample is large choose

a large aperture to maximise reflectance. Aperture Mask Calibration for the angle(s), wavelength(s) and aperture to be used in the experiment. BRDF Calibration for reflection measurements using the above angle and wavelength ranges. Press the 'reset queue' button and ensure wavelength information is the same.

Note - Software will (sometimes) forget angular and wavelength information between screens. Ensure these are set correctly before beginning a measurement.

B.1.3 Measurements using the Imaging Sphere

Fix the sample to the aperture. If the sample is small enough, cover with the light trap. For a highly specular sample choose 'bright spot' for auto-exposure time. For diffuse samples choose 'average' for auto-exposure time. For highly transparent samples you can fix the exposure time to prevent excessively long runs. Choose either B_DF or CCB_DF (cosine corrected) before the scan. Where the gap is R for reflection or T for transmission. If unsure, choose cosine corrected. Use the 'scan' option to run through the wavelength and angular ranges calibrated for. For each 'scan' create a new measurement database. Useful data can be found using the IS-SA report tool such as total reflectance.

B.1.4 Exporting Data from the Imaging Sphere

For each measurement database click 'tools' $\rightarrow$ 'BRDF export'. Ensure 'Assume Symmetry' is switched OFF. Added relevant information is added and ensure correct 'side' to chosen. Export away! The resulting BRDF file can be read using the code at Github Optical Measurements. The format information is availabe in full at Radiant Zemax BSDF File Format.

Appendix C

Theoretical Model and Validation

C.1 Cramer Rao Derivation

We begin by determining the expectation value of $\frac{\partial \lambda_n}{\partial \Theta}$

$$\frac{\partial \lambda_n}{\partial \Theta} = \frac{\partial}{\partial \Theta} \ln p_n(\vec{t}|\Theta) = \frac{1}{p_n} \frac{\partial p_n}{\partial \Theta} \tag{C.1}$$

$$\mathrm{E}[\Big(\frac{\partial \lambda_n}{\partial \Theta}\Big)] = \int \cdots \int \frac{1}{p_n} \frac{\partial p_n}{\partial \Theta} f_n dt_1 \cdots dt_n \tag{C.2}$$

$$\mathrm{E}[\Big(\frac{\partial \lambda_n}{\partial \Theta}\Big)] = \int \cdots \int \frac{\partial p_n}{\partial \Theta} dt_1 \cdots dt_n = 0 \tag{C.3}$$

This equals zero because one of the properties of the PDF is

$$\int_S p(t|\Theta) dt = 1 \tag{C.4}$$

where S is every possible value of t. We can use this result to redefine the Fisher information (equation 5.5) in terms of variance such that

$$\mathrm{Var}[X] := \mathrm{Cov}[X, X] = E[X^2] - E[X]^2 \tag{C.5}$$

Therefore

$$\mathrm{Var}[\Big(\frac{\partial\lambda}{\partial\Theta}\Big)] = E[\Big(\frac{\partial\lambda}{\partial\Theta}\Big)^2] - E[\Big(\frac{\partial\lambda}{\partial\Theta}\Big)]^2 \tag{C.6}$$

$$I(\Theta) = \mathrm{Var}[\Big(\frac{\partial\lambda}{\partial\Theta}\Big)] = E[\Big(\frac{\partial\lambda}{\partial\Theta}\Big)^2] \tag{C.7}$$

Using this result we can use the Cauchy-Schwarz inequality

$$\Big(\mathrm{Cov}[X,Y]\Big)^2 \leq \sigma_X^2\sigma_Y^2 \tag{C.8}$$

where $\mathrm{Cov}[X,Y]$ is the covariance defined as

$$\mathrm{Cov}[X,Y] = E[XY] - E[X]E[Y] \tag{C.9}$$

we should be able to reach an equation relating the variance in a parameter to the Fisher Information. Firstly We define a statistic $T = r(\vec{t})$ which is an estimator of the parameter Θ. Using equation C.8 we see that

$$\mathrm{Cov}[T, \frac{\partial\lambda_n}{\partial\Theta}] = E[T\frac{\partial\lambda_n}{\partial\Theta}] - E[T]E[\frac{\partial\lambda_n}{\partial\Theta}] \tag{C.10}$$

Which using equation C.3 reduces to

$$\mathrm{Cov}[T, \frac{\partial\lambda_n}{\partial\Theta}] = \int\cdots\int r(\vec{t})\frac{\partial\lambda_n}{\partial\Theta}dt_1\cdots dt_n = \frac{\partial m(\Theta)}{\partial\Theta} \tag{C.11}$$

Therefore using the Cauchy-Schwarz inequality with equations C.7 and 5.6 we now see

$$\Big(\mathrm{Cov}[T, \frac{\partial\lambda_n}{\partial\Theta}]\Big)^2 \leq \mathrm{Var}[T]\mathrm{Var}[\frac{\partial\lambda_n}{\partial\Theta}] \tag{C.12}$$

$$\Big(\frac{\partial m(\Theta)}{\partial\Theta}\Big)^2 \leq \mathrm{Var}[T]nI(\Theta) \tag{C.13}$$

$$\boxed{\mathrm{Var}[T] \geq \Big(\frac{\partial m(\Theta)}{\partial\Theta}\Big)^2\frac{1}{nI(\Theta)}} \tag{C.14}$$

And thus we get to the Cramer-Rao lower bound. For this to be valid, the statistic T must follow the form

$$r(\vec{t}) = u(\Theta)\frac{\partial \lambda_n}{\partial \Theta} + v(\Theta) \tag{C.15}$$

Appendix D

Photonics

D.1 Unpolarised Light

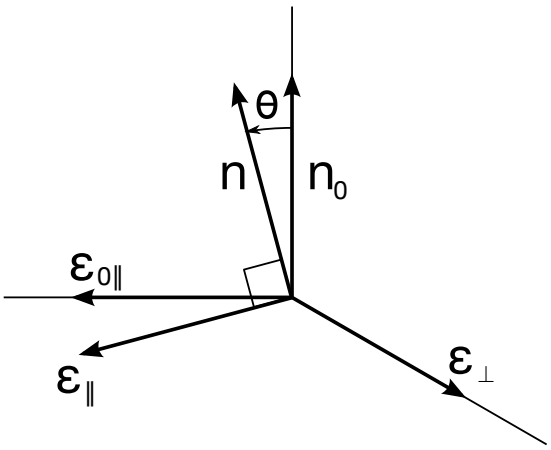

Figure D.1: Orthogonal Modes, $\epsilon_\perp$ and $\epsilon_\parallel$, defined relative to incident and outgoing directions.

In figure D.1 we define two orthogonal polarisations relative to the incident and outgoing directions These can be stated mathematically as

$$\vec{\epsilon}_\perp = \vec{n}_0 \times \vec{n} \tag{D.1}$$

$$\vec{\epsilon}_\parallel = \vec{\epsilon}_\perp \times \vec{n}_0 = (\vec{n}_0 \times \vec{n}) \times \vec{n}_0 \tag{D.2}$$

where $\vec{n}_0$ is the incident direction vector, $\vec{n}$ is the scattered direction vector and $\vec{k}$ is the wavevector of the incoming wave. The wavevector can be defined as

$$\vec{k} = k\vec{n}_0 \tag{D.3}$$

$$\therefore \vec{k} = k(\vec{\epsilon}_{\parallel} \times \vec{\epsilon}_{\perp}) \tag{D.4}$$

For these two polarisations we can define two individual differential cross sections for the two known polarisations as

$$\frac{d\sigma}{d\Omega} = \frac{k^4}{(4\pi\epsilon_0 E_0)^2}|\vec{\epsilon}.\vec{p}|^2 F \tag{D.5}$$

$$\therefore \frac{d\sigma_{\parallel}}{d\Omega} = \frac{k^4}{(4\pi\epsilon_0 E_0)^2}|-\vec{p}.\vec{n}_0 \times (\vec{n}_0 \times \vec{n})|^2 F \tag{D.6}$$

$$\therefore \frac{d\sigma_{\perp}}{d\Omega} = \frac{k^4}{(4\pi\epsilon_0 E_0)^2}|\vec{p}.(\vec{n}_0 \times \vec{n})|^2 F \tag{D.7}$$

For unpolarised light we must consider both polarisations equally, such that

$$\frac{d\sigma}{d\Omega} = \frac{k^4}{(4\pi\epsilon_0 E_0)^2}\left|(\vec{\epsilon}^*_{\perp}.\vec{p})\vec{\epsilon}_{\perp} + (\vec{\epsilon}^*_{\parallel}.\vec{p})\vec{\epsilon}_{\parallel}\right|^2 F(\vec{q}) \tag{D.8}$$

$$\frac{d\sigma}{d\Omega} = \frac{d\sigma_{\perp}}{d\Omega} + \frac{d\sigma_{\parallel}}{d\Omega} \tag{D.9}$$

This results in an addition of the two orthogonal modes for unpolarised light.

Bibliography

[1] L Eriksson. Experience with scintillators for PET: towards the fifth generation of PET scanners. *Nuclear Instruments and Methods in Physics Research Section A: Accelerators, Spectrometers, Detectors and Associated Equipment*, 525(1-2):242–248, jun 2004.

[2] Pieter Dorenbos. Fundamental Limitations in the Performance of Ce3+ , Pr3+ , and Eu2+ Activated Scintillators. *Nuclear Science, IEEE Transactions on*, 57(3):1162–1167, 2010.

[3] Stephen Derenzo. Scintillation properties. `http://scintillator.lbl.gov/`. [Online; Accessed 18 Dec, 2012].

[4] Paul Lecoq. *Radiation Detectors for Medical Applications (Chapter : New Trends in PET Detector Developments)*. Springer Netherlands, Dordrecht, 2006.

[5] P Geramifar, M R Ay, M Shamsaie Zafarghandi, S Sarkar, G Loudos, and A Rahmim. Investigation of time-of-flight benefits in an LYSO-based PET/CT scanner: A Monte Carlo study using GATE. *Nuclear Instruments and Methods in Physics Research Section A: Accelerators, Spectrometers, Detectors and Associated Equipment*, 641(1):121–127, jun 2011.

[6] WW Moses. Time of flight in PET revisited. *Nuclear Science, IEEE Transactions on*, 50(5):1325–1330, 2003.

[7] Borys Grinyov and Margaryta Globus. *"Radiation Detectors for Medical Applications (Chapter : Scintillation detectors for medical and biology applications)"*. Springer, 2006.

[8] Mark S Brown, Stefan Gundacker, Alaric Taylor, Clemens Tummeltshammer, Etiennette Auffray, Paul Lecoq, and Ioannis Papakonstantinou. Influence of depth of interaction upon the performance of scintillator detectors. *PloS one*, 9(5):e98177, 2014.

[9] Radiation Protection of Patients (RPOP) - PET/CT Scanning. `https://rpop.iaea.org/RPOP/RPoP/Content/InformationFor/HealthProfessionals/6_OtherClinicalSpecialities/PETCTscan.htm`, 2011. [Online; accessed 2011-12-14].

[10] Kengo Shibuya, Eiji Yoshida, Fumihiko Nishikido, Toshikazu Suzuki, Tomoaki Tsuda, Naoko Inadama, Taiga Yamaya, and Hideo Murayama. Annihilation photon acollinearity in PET: volunteer and phantom FDG studies. *Physics in medicine and biology*, 52(17):5249–61, sep 2007.

[11] CS Levin. Calculation of positron range and its effect on the fundamental limit of positron emission tomography system spatial resolution. *Physics in medicine and biology*, 781, 1999.

[12] Maurizio Conti. State of the art and challenges of time-of-flight PET. *Physica medica : PM : an international journal devoted to the applications of physics to medicine and biology : official journal of the Italian Association of Biomedical Physics (AIFB)*, 25(1):1–11, mar 2009.

[13] L Eriksson, M Conti, C L Melcher, Senior Member, D W Townsend, M Eriksson, H Rothfuss, M E Casey, and B Bendriem. Towards Sub-Minute PET Examination Times. 58(1):76–81, 2011.

[14] T Kimble, M Chou, and B H T Chai. Scintillation properties of LYSO crystals. *Nuclear Science Symposium ...*, 2002.

[15] Maurizio Conti, Lars Eriksson, Harold Rothfuss, and Charles L Melcher. Comparison of Fast Scintillators With TOF PET Potential. *IEEE Transactions on Nuclear Science*, 56(3):926–933, jun 2009.

[16] John B. Birks. *The theory and practice of scintillation counting.* Pergamon Press, 1964.

[17] Photonis. Xp2020 pmt information sheet. `http://www.datasheet.co.kr/datasheet-html/X/P/2/XP2020_Photonis.pdf.html`, 2013. [Online; Accessed 15 Jan, 2013].

[18] Hamamatsu. S10931-050p mppc information sheet. http://www.hamamatsu.com/jp/en/product/alpha/M/4113/S10931-050P/index.html, 2013. [Online; Accessed 17 Sept, 2013].

[19] Hamamatsu Photonics. *Photomultiplier Tubes: Basics and Applications*. Hamamatsu Photonics, third edition, 2006.

[20] Carel W E van Eijk. Inorganic scintillators in medical imaging. *Physics in medicine and biology*, 47(8):R85–106, apr 2002.

[21] National Institute of Science and Technology. Xcom: Photon cross sections database. http://physics.nist.gov/PhysRefData/Xcom/html/xcom1.html, 2010. [Online; Accessed 27 Nov, 2012].

[22] E Auffray, B Frisch, F Geraci, a. Ghezzi, S Gundacker, H Hillemanns, P Jarron, T Meyer, M Paganoni, K Pauwels, M Pizzichemi, and P Lecoq. A comprehensive & systematic study of coincidence time resolution and light yield using scintillators of different size, wrapping and doping. *2011 IEEE Nuclear Science Symposium Conference Record*, pages 64–71, oct 2011.

[23] W W Moses and M Ullisch. Factors influencing timing resolution in a commercial LSO PET camera. *Nuclear Science, IEEE Transactions on*, 53(1):78–85, 2006.

[24] Stefan Seifert, Herman T van Dam, and Dennis R Schaart. The lower bound on the timing resolution of scintillation detectors. *Physics in medicine and biology*, 57(7):1797–1814, mar 2012.

[25] K.K. S. *Introductory Nuclear Physics*. Wiley India, 2008.

[26] Ludivine Pidol, A Kahn-Harari, and Bruno Viana. High efficiency of lutetium silicate scintillators, Ce-doped LPS and LYSO crystals. *Record, 2003 IEEE*, 51(3):1084–1087, 2003.

[27] M Balcerzyk and M Moszynski. YSO, LSO, GSO and LGSO. A study of energy resolution and nonproportionality. *Nuclear Science, ...*, 2:3–7, 2000.

[28] S Gundacker, E Auffray, and B Frisch. A Systematic Study to Optimize SiPM Photo-Detectors for Highest Time Resolution in PET. *ieeexplore.ieee.org*, 59(5):1798–1804, 2013.

[29] C Carrier. Effect of geometrical modifications and crystal defects on light collection in ideal rectangular parallelepipedic BGO scintillators. *Nuclear Instruments and Methods in Physics*, 294:355–364, 1990.

[30] C Carrier. Theoretical modelling of light transport in rectangular parallelepipedic scintillators. *Nuclear Instruments and Methods in Physics*, 292:685–692, 1990.

[31] JS Huber, WW Moses, and MS Andreaco. Geometry and surface treatment dependence of the light collection from LSO crystals. *Nuclear Instruments and*, 437:374–380, 1999.

[32] M Cocchi and A Rota. Light collection on a photocathode from a cylindrical scintillator. *Nuclear Instruments and Methods*, 46(3):136–140, 1967.

[33] Florian Bauer, James Corbeil, and Matthias Schmand. Measurements and Ray-Tracing Simulations of Light Spread in LSO Crystals. *Nuclear Science, IEEE*, 56(5):2566–2573, 2009.

[34] WW W.W. Moses and S.E. Derenzo. Prospects for time-of-flight PET using LSO scintillator. *Nuclear Science, IEEE*, 46(3):474–478, jun 1999.

[35] William W Moses. Trends in PET imaging. *Nuclear Instruments and Methods in Physics Research Section A: Accelerators, Spectrometers, Detectors and Associated Equipment*, 471(1-2):209–214, Sep 2001.

[36] John L. Humm, Anatoly Rosenfeld, and Alberto Del Guerra. From PET detectors to PET scanners. *European Journal of Nuclear Medicine and Molecular Imaging*, 30(11):1574–1597, Nov 2003.

[37] Herman T van Dam, Giacomo Borghi, Stefan Seifert, and Dennis R Schaart. Sub-200ps CRT in monolithic scintillator PET detectors using digital SiPM arrays and maximum likelihood interaction time estimation. *Physics in medicine and biology*, 58(10):3243–57, may 2013.

[38] D J Jan van der Laan, Marnix C Maas, Peter Bruyndonckx, and Dennis R Schaart. Limits on the spatial resolution of monolithic scintillators read out by APD arrays. *Physics in medicine and biology*, 57(20):6479–6496, oct 2012.

[39] Dennis R Schaart, Herman T van Dam, Stefan Seifert, Ruud Vinke, Peter Dendooven, Herbert Löhner, and Freek J Beekman. A novel, SiPM-array-based, monolithic scintillator detector for PET. *Physics in Medicine and Biology*, 54(11):3501–3512, Jun 2009.

[40] Stefan Seifert, Gerben van der Lei, Herman T van Dam, and Dennis R Schaart. First characterization of a digital SiPM based time-of-flight PET detector with 1 mm spatial resolution. *Physics in Medicine and Biology*, 58(9):3061–3074, May 2013.

[41] Inc. Proteus. Lyso:ce lutetium-yttrium oxyorthosilicate, ce+3 doped lyso crystals & assemblies. `http://www.apace-science.com/proteus/lyso.htm`, 2013. [Online; accessed 20-September-2013].

[42] P. a. Cutler, C. L. Melcher, M. a. Spurrier, P. Szupryczynski, and L. a. Eriksson. Scintillation Non-Proportionality of Lutetium- and Yttrium-Based Silicates and Aluminates. *IEEE Transactions on Nuclear Science*, 56(3):915–919, jun 2009.

[43] MA Spurrier, CL Melcher, and P Szupryczynski. Effects of Ca2+ co-doping on the scintillation properties of LSO: Ce. *growth*, page 2007, 2008.

[44] Rhodorsil. Rhodorsil 47v optical grease datasheet. `http://www.rbhltd.com/rbh_news/wp-content/uploads/2012/01/TDS-47v50.pdf`, 2013. [Online; Accessed 19 Aug, 2013].

[45] Gábor Erdei, Noémi Berze, Ágnes Péter, Balázs Játékos, and Emke Lrincz. Refractive index measurement of cerium-doped LuxY2xSiO5 single crystal. *Optical Materials*, 34(5):781–785, mar 2012.

[46] S Gundacker, E Auffray, B Frisch, P Jarron, a Knapitsch, T Meyer, M Pizzichemi, and P Lecoq. Time of flight positron emission tomography towards 100ps resolution with L(Y)SO: an experimental and theoretical analysis. *Journal of Instrumentation*, 8:P07014–P07014, 2013.

[47] M.H. DeGroot and M.J. Schervish. *Probability and Statistics: International Edition*. Pearson Education, Limited, 2011.

[48] S. Gundacker, A. Knapitsch, E. Auffray, P. Jarron, T. Meyer, and P. Lecoq. Time resolution deterioration with increasing crystal length in a TOF-PET system. *Nuclear Instruments and*

Methods in Physics Research Section A: Accelerators, Spectrometers, Detectors and Associated Equipment, 737:92–100, Feb 2014.

[49] R I Wiener, M Kaul, S Surti, and J S Karp. Signal analysis for improved timing resolution with scintillation detectors for TOF PET imaging. *IEEE Nuclear Science Symposuim & Medical Imaging Conference*, pages 1991–1995, Oct 2010.

[50] Woon-Seng Choong. The timing resolution of scintillation-detector systems: Monte Carlo analysis. *Physics in Medicine and Biology*, 54(21):6495–6513, Nov 2009.

[51] Alberto Gola, Claudio Piemonte, and Alessandro Tarolli. Analog Circuit for Timing Measurements With Large Area SiPMs Coupled to LYSO Crystals. *IEEE Transactions on Nuclear Science*, 60(2):1296–1302, Apr 2013.

[52] Claudio Piemonte, Alberto Gola, Antonio Picciotto, Tiziana Pro, Nicola Serra, Alessandro Tarolli, and Nicola Zorzi. Timing performance of large area SiPMs coupled to LYSO using dark noise compensation methods. *2011 IEEE Nuclear Science Symposium Conference Record*, pages 59–63, Oct 2011.

[53] W.W. Moses and S.E. Derenzo. Prospects for time-of-flight PET using LSO scintillator. *IEEE Transactions on Nuclear Science*, 46(3):474–478, Jun 1999.

[54] Martin Janecek and William W Moses. Simulating Scintillator Light Collection Using Measured Optical Reflectance. *IEEE Transactions on Nuclear Science*, 57(3):964–970, jun 2010.

[55] Chad Bircher and Yiping Shao. Investigation of crystal surface finish and geometry on single LYSO scintillator detector performance for depth-of-interaction measurement with silicon photomultipliers. *Nuclear Instruments and Methods in Physics Research Section A: Accelerators, Spectrometers, Detectors and Associated Equipment*, 693:236–243, Nov 2012.

[56] S. Felekyan, R. Kuhnemuth, V. Kudryavtsev, C. Sandhagen, W. Becker, and C. a. M. Seidel. Full correlation from picoseconds to seconds by time-resolved and time-correlated single photon detection. *Review of Scientific Instruments*, 76(8):083104, 2005.

[57] L. M. Bollinger and G. E. Thomas. Measurement of the Time Dependence of Scintillation Intensity by a Delayed-Coincidence Method. *Review of Scientific Instruments*, 32(9):1044, 1961.

[58] Edinburgh Instruments Ltd. Picosecond light sources. `http://www.edinburghphotonics.com/lasers-leds/picosecond%20pulsed%20lasers%20and%20LEDs/`, 2012. [Online; Accessed 1 Dec, 2012].

[59] W Becker. The bh TCSPC handbook. *Becker & Hickl GmbH,*, 2008.

[60] J. Veče, a. a. Kowalczyk, L. Davenport, and R. E. Dale. Reconvolution analysis in time-resolved fluorescence experiments - An alternative approach: Reference-to-excitation-to-fluorescence reconvolution. *Review of Scientific Instruments*, 64(May 2012):3413–3424, 1993.

[61] Edinburgh Instruments. Fluorescence analysis software technology. `http://www.edinburghphotonics.com/spectrometers/software/fast/`, 2015. [Online; accessed 24-June 2015].

[62] Johan T. M. de Haas and Pieter Dorenbos. Advances in Yield Calibration of Scintillators. *IEEE Transactions on Nuclear Science*, 55(3):1086–1092, jun 2008.

[63] S. Seifert. Accurate measurements of the rise and decay times of fast scintillators with solid state photon counters. *Record (NSS/MIC),*, pages 1736–1739, 2010.

[64] JW Cates, JP Hayward, and X Zhang. Increased Light Extraction From Inorganic Scintillators With Laser-Etched Microstructures. *IEEE Transactions on Nuclear Science*, 60(2):1027–1032, 2013.

[65] D.K. McAllister. A generalized surface appearance representation for computer graphics. *Computer*, 2002.

[66] Martin Janecek and William W. Moses. Optical Reflectance Measurements for Commonly Used Reflectors. *IEEE Transactions on Nuclear Science*, 55(4):2432–2437, aug 2008.

[67] S Agostinelli, J Allison, and K Amako. GEANT4a simulation toolkit. *Nuclear Instruments and Methods in Physics Research A*, 506(3):250–303, jul 2003.

[68] Robert Yeo, Ron Rykowski, Doug Kreysar, and Kevin Chittim. The Imaging Sphere - the First Appearance Meter? *Proc. of The 5th Oxford Conference on Spectroscopy*, (June):87–103, 2006.

[69] Scintillation Crystals, Their Recommended, and Shaping Times. Wrapping Scintillator Crystals to Optimize Light Collection. pages 1–4, 2011.

[70] A O Hero and I Introduction. A lower bound on PET timing estimation with pulse pileup. *IEEE Transactions on Nuclear Science*, 38(2):1–4, 1991.

[71] D J Van Der Laan and M C Maas. Using Cramér-Rao theory combined with Monte Carlo simulations for the optimization of monolithic scintillator PET detectors. *IEEE Transactions on Nuclear Science*, 53(3):1063–1070, 2006.

[72] Stefan Seifert, Gerben van der Lei, Herman T van Dam, and Dennis R Schaart. First characterization of a digital SiPM based time-of-flight PET detector with 1 mm spatial resolution. *Physics in medicine and biology*, 58(9):3061–3074, may 2013.

[73] Stefan Seifert and H T van Dam. A comprehensive model to predict the timing resolution of SiPM-based scintillation detectors: theory and experimental validation. *Nuclear Science, ...*, 59(1):190–204, 2012.

[74] L G Hyman. Time Resolution of Photomultiplier Systems. *Review of Scientific Instruments*, 36(2):193, 1965.

[75] T Ludziejewski. Advantages and limitations of LSO scintillator in nuclear physics experiments. *IEEE Transactions on Nuclear Science*, 42(4):328–336, 1995.

[76] Wikipedia. Skew normal distribution — wikipedia, the free encyclopedia. `http://en.wikipedia.org/w/index.php?title=Skew_normal_distribution&oldid=554173728`, 2013. [Online; accessed 13-June-2013].

[77] S Gundacker, E Auffray, N Di Vara, B Frisch, H Hillemanns, P Jarron, B Lang, T Meyer, S Mosquera-vazquez, E Vauthey, and P Lecoq. Nuclear Instruments and Methods in Physics Research A SiPM time resolution : From single photon to saturation. *Nuclear Inst. and Methods in Physics Research, A*, pages 1–4, 2013.

[78] Wikipedia. Half-normal distribution — wikipedia, the free encyclopedia. http://en.wikipedia.org/w/index.php?title=Half-normal_distribution&oldid=553854660, 2013. [Online; accessed 13-June-2013].

[79] J.D. Jackson. *Classical Electrodynamics*. Wiley, 1999.

[80] S Gundacker, E Auffray, B Frisch, P Jarron, a Knapitsch, T Meyer, M Pizzichemi, and P Lecoq. Time of flight positron emission tomography towards 100ps resolution with L(Y)SO: an experimental and theoretical analysis. *Journal of Instrumentation*, 8(07):P07014–P07014, jul 2013.

[81] R. McCluney. *Introduction to Radiometry and Photometry*. Artech House optoelectronics library. Artech House, 1994.

[82] E Auffray, F Cavallari, and M Lebeau. Crystal conditioning for high-energy physics detectors. *Nuclear Instruments and Methods in Physics Research A*, 486:22–34, 2002.

[83] Matthias Kronberger, Etiennette Auffray, and Paul Lecoq. Probing the Concepts of Photonic Crystals on Scintillating Materials. *IEEE Transactions on Nuclear Science*, 55(3):1102–1106, jun 2008.

[84] AR Knapitsch. *Photonic Crystals: Enhancing the Light Output of Scintillation Based Detectors*. PhD thesis, 2012.

[85] Jeong-Gil Kim, Chih-Hung Hsieh, Hyungryul J. Choi, Jules Gardener, Bipin Singh, Arno Knapitsch, Paul Lecoq, and George Barbastathis. Conical photonic crystals for enhancing light extraction efficiency from high refractive index materials. *Optics Express*, 23(17):22730, 2015.

[86] Eric W Weisstein. Sphere point picking. http://mathworld.wolfram.com/SpherePointPicking.html, 2002.

[87] Nanfang Yu, Patrice Genevet, Mikhail a Kats, Francesco Aieta, Jean-Philippe Tetienne, Federico Capasso, and Zeno Gaburro. Light Propagation with Phase Discontinuities Reflection and Refraction. *Science*, 334(October):333–337, 2011.

[88] C. L. Holloway, E. F. Kuester, J. a. Gordon, J. O'Hara, J. Booth, and D. R. Smith. An Overview of the Theory and Applications of Metasurfaces: The Two-Dimensional Equivalents of Metamaterials. *IEEE Antennas and Propagation Magazine*, 54(2):10–35, apr 2012.

[89] Matthias Kronberger and Etiennette Auffray. Improving light extraction from heavy inorganic scintillators by photonic crystals. *Nuclear Science, IEEE*, 57(5):2475–2482, 2010.

[90] P. Lecoq, E. Auffray, and a. Knapitsch. How Photonic Crystals Can Improve the Timing Resolution of Scintillators. *IEEE Transactions on Nuclear Science*, 60(3):1653–1657, 2013.

[91] Arno Knapitsch, Etiennette Auffray, Christian W. Fabjan, Jean-Louis Leclercq, Xavier Letartre, Radoslaw Mazurczyk, and Paul Lecoq. Results of Photonic Crystal Enhanced Light Extraction on Heavy Inorganic Scintillators. *IEEE Transactions on Nuclear Science*, pages 2–7, 2012.

[92] P. Pignalosa, Bo Liu, Hong Chen, H. Smith, and Yasha Yi. Giant light extraction enhancement of medical imaging scintillation materials using biologically inspired integrated nanostructures. *Optics Letters*, 37(14):2808, 2012.

[93] M. Kaul, S. Surti, and J. S. Karp. Combining Surface Treatments With Shallow Slots to Improve the Spatial Resolution Performance of Continuous, Thick LYSO Detectors for PET. *IEEE Transactions on Nuclear Science*, 60(1):44–52, feb 2013.

[94] Lumerical Solutions Inc. FDTD Solutions. `http://www.lumerical.com/tcad-products/fdtd/`. [Electromagnetic Simulation Software].

[95] Anders Pors, Ole Albrektsen, Ilya P Radko, and Sergey I Bozhevolnyi. Gap plasmon-based metasurfaces for total control of reflected light. *Scientific reports*, 3:2155, jan 2013.

[96] Anders Pors and Sergey I Bozhevolnyi. Plasmonic metasurfaces for efficient phase control in reflection. *Optics Express*, 21(22):27438, nov 2013.

[97] Xin Li, Shiyi Xiao, Bengeng Cai, Qiong He, Tie Jun Cui, and Lei Zhou. Flat metasurfaces to focus electromagnetic waves in reflection geometry. *Optics letters*, 37(23):4940–2, dec 2012.

[98] Peter Bienstman, L Vanholme, M Ibanescu, P Dumon, and R Baets. Camfr: Cavity modeling framework. *Software at http://camfr. sourceforge. net*, 2008.

[99] Owen D. Miller. Photonic Design: From Fundamental Solar Cell Physics to Computational Inverse Design. *Thesis, Berkeley*, page 137, 2012.

[100] Craig F Bohren and Donald R Huffman. *Absorption and scattering of light by small particles*. John Wiley & Sons, 2008.

[101] Viktar S. Asadchy, Igar a. Faniayeu, Younes Ra'Di, and Sergei a. Tretyakov. Determining polarizability tensors for an arbitrary small electromagnetic scatterer. *Photonics and Nanostructures - Fundamentals and Applications*, 12:298–304, 2014.

[102] Mark W. Knight, Lifei Liu, Yumin Wang, Lisa Brown, Shaunak Mukherjee, Nicholas S. King, Henry O. Everitt, Peter Nordlander, and Naomi J. Halas. Aluminum plasmonic nanoantennas. *Nano Letters*, 12(11):6000–6004, 2012. PMID: 23072330.

[103] D. Lin, P. Fan, E. Hasman, and M. L. Brongersma. Dielectric gradient metasurface optical elements. *Science*, 345(6194):298–302, 2014.

[104] Nikolay I. Zheludev and Yuri S. Kivshar. From metamaterials to metadevices. *Nature Materials*, 11(11):917–924, 2012.

[105] Eric Berg, Emilie Roncali, and Simon R. Cherry. Optimizing light transport in scintillation crystals for time-of-flight PET: an experimental and optical Monte Carlo simulation study. *Biomedical Optics Express*, 6(6):2220, 2015.

[106] F. Anghinolfi and P. Jarron. NINO, an ultra-fast, low-power, front-end amplifier discriminator for the Time-Of-Flight detector in ALICE experiment. *Record, 2003 IEEE*, 51(5):1974–1978, oct 2003.

[107] Geant4. Geant4 User's Guide for Application Developers. `http://geant4.web.cern.ch/geant4/UserDocumentation/UsersGuides/ForApplicationDeveloper/BackupVersions/V9.4/fo/BookForAppliDev.pdf`, 2011.

[108] D Strulab, G Santin, D Lazaro, V Breton, and C Morel. Gate (geant4 application for tomographic emission): a pet/spect general-purpose simulation platform. *Nuclear Physics B-Proceedings Supplements*, 125:75–79, 2003.

[109] Michal Gierlik, Marek Moszynski, Antoni Nassalski, Agnieszka Syntfeld-Kazuch, Tomasz Szczśniak, and Lukasz Swiderski. Investigation of absolute light output measurement techniques. *IEEE Transactions on Nuclear Science*, 54(4):1367–1371, 2007.